UNIVERSITÀ DEGLI STUDI DI PADOVA

Amministrativa :
Università degli Studi di Padova
Dipartimento di Scienze Chimiche

SCUOLA DI DOTTORATO DI RICERCA IN
SCIENZA ED INGEGNERIA DEI MATERIALI
CICLO XXVI

Tesi di Dottorato

Model electrocatalysts for fuel cells: a surface science based study

Direttore della Scuola: Ch.mo Prof. Gaetano Granozzi

Supervisore: Ch.mo Prof. Gaetano Granozzi

Dottorando: Zheng Jian

Abstract

The present thesis focuses on studying structure/morphology/activity relationships in bimetallic Pt-Sn nanostructured electrodes for proton exchange membrane (PEM) fuel cells by adopting a rigorous surface science approach where:

i) Model electrocatalysts are prepared in ultra-high-vacuum (UHV) conditions as ultrathin (UT) films ($PtSn_x$/Pt(110) and SnO_x/Pt(110)) to ensure a very reproducible control down to the atomic level;

ii) Composition, morphology and structure of the UT nanostructured films are studied *in situ* by adopting state-of-the-art characterization tools;

iii) Quantum mechanical calculations are carried out adopting the density functional theory (DFT) in order to determine the atomic structure of the UT films.

A systematic search for possible Sn alloy or oxides on Pt(110) surface phases was carried out. Three surface alloys (including one already reported surface alloy) and two surface oxides on Pt(110) surface were identified.

The two novel surface alloys: p(3×1)PtSn/Pt(110) and p(6×1) PtSn/Pt(110) can be prepared by means of UHV Sn deposition on Pt(110) at different thickness and by a subsequent annealing at proper temperature. Besides, two SnO_x oxides surfaces, namely the c(2×4)SnO_x/Pt(110) and the c(4×2) SnO_x/Pt(110), were prepared by oxidizing the surface alloys. With optimization of the preparation conditions, a phase diagram for the surface alloys and surface oxides on Pt(110) was outlined.

The two novel surface alloys were characterized by low energy electron diffraction (LEED), scanning tunnelling microscopy (STM) and synchrotron radiation photoemission spectroscopy (SRPES). STM images of the two surface alloys are characterized by a highly corrugated row structure whereas photoemission data indicate a complex intermixing between Pt and Sn which leads to the formation of extended near-surface alloys. Some models for the two surfaces were proposed on the basis of the experimental evidences. These models were then compared with DFT calculations and the simulated STM images of the models were used as final assessment of their validity.

The reactivity of the surface alloys with CO was investigated both experimentally by thermal programmed desorption (TPD) and theoretically by DFT calculations. The results reveal a scarce reactivity towards CO on the two surfaces due the lower adsorption energy with respect to pure Pt(110) surface, indicating their use as highly CO tolerant catalysts. Based on the DFT results, the surfaces can have also an improved performance in CO oxidation reaction (COOR) on the basis of the calculated d-band centroid value.

The two surface oxides (c(2×4)SnO_x/Pt(110) and c(2×4)SnO_x/Pt(110)) were investigated by LEED, STM and SRPES. Some models for the two surfaces were proposed based on the experimental results, and investigated by DFT calculations. The good agreement between the simulated STM images with the experimental data suggests a good reliability of the proposed structures.

The reactivity towards CO for the two oxidised phases was also investigated. The c(4×2) structure, constituted by a slightly oxidised Sn overlayer, demonstrated to be scarcely reactive, whereas the more oxidized c(2×4) phase proved to be able to efficiently oxidize CO. These results were also confirmed by DFT. The decomposition of methanol on c(2×4) surface was also investigated by TPD and SRPES, indicating that the methanol can be oxidised efficiently into CO_2 and H_2O. However the body of our experimental data points to a quite complex oxidation mechanism whose selectivity changes dynamically according to the experimental conditions. The fully oxidised c(2×4) can efficiently oxidise methanol to CO_2 at low temperature, but this reaction path is progressively suppressed as soon as the phase is reduced. In this regime the methanol is oxidized to CO_2 at higher temperature and less efficiently, the microscopic mechanism of the reaction implies the supply of oxygen by c(2×4) islands on reduced Pt or PtSn areas by spillover, where the actual reaction takes place. When the spillover is not anymore possible, because the methanol decomposition has removed most oxygen, methanol is simply oxidatively dehydrogenated to CO and H_2, similarly to what happens on the clean Pt(110) surface but at a slightly lower temperature.

Key words: Fuel cell, PtSn, surface alloys, surface oxides, CO reactivity, methanol decomposition

Riassunto

La presente tesi si concentra sullo studio della relazione struttura / morfologia / reattività in elettrodi bimetallici nanostrutturati Pt - Sn per celle a combustibile a membrana a scambio protonico (PEM), adottando un rigoroso approccio di scienza delle superfici sviluppato come segue:

i) sistemi modello di elettrocatalizzatori sono stati preparati in condizioni di ultra - alto vuoto (UHV) depositando via epitassia da fasci molecolari (MBE) strati ultrasottili (UT) di $PtSn_x$ e SnO_x su superfici di Pt monocristallino orientate (110), al fine di garantire un controllo fine e riproducibile su scala atomica;

ii) composizione, morfologia e struttura dei film nanostrutturati UT sono stati studiati *in situ* mediante l'adozione di strumenti di caratterizzazione in linea con le più avanzate tecniche offerte dallo stato dell'arte;

iii) calcoli quanto-meccanici basati sulla teoria del funzionale densità (DFT) sono quindi stati effettuati per determinare la struttura atomica dei film UT, in modo da razionalizzare e supportare i risultati sperimentali ottenuti al punto precedente.

Una ricerca sistematica è stata effettuata allo scopo di identificare nuove possibili fasi di superficie di Sn o ossidi di Sn supportate su Pt (110). In questo modo, tre leghe di superficie (di cui una risulta già nota in letteratura) e due ossidi di superficie su Pt (110) sono stati identificati. Le due innovative leghe da film UT, la p(3 × 1) PtSn / Pt (110) e la p(6 × 1) PtSn / Pt (110) possono essere sintetizzate mediante deposizione di Sn su Pt (110), preparando spessori diversi e sottoponendo le superfici così ottenute a trattamenti termici effettuati a diverse temperature. Conseguentemente, l'ossidazione ad alta temperatura delle leghe superficiali ha permesso l'ottenimento di due nuove fasi ossidate di superficie, la (c(2 × 4) SnO_x / Pt (110) e la c(4 × 2) SnO_x / Pt (110). Infine, data l'elevata flessibilità delle tecniche di preparazione e caratterizzazione offerte dalla scienza delle superfici, è stato possibile delineare con grande accuratezza un diagramma di fase sia per le leghe che per gli ossidi di superficie sopra descritti.

Le due nuove leghe superficiali sono state caratterizzate mediante diffrazione di elettroni a bassa energia cinetica (LEED), microscopia a scansione ad effetto tunnel (STM) e spettroscopia di fotoemissione da radiazione di sincrotrone (SRPES). Le immagini STM delle due leghe superficiali sono caratterizzate da una struttura a righe altamente corrugata; i dati di fotoemissione indicano inoltre un complesso intermixing tra Pt e Sn che porta alla formazione di leghe localizzate in prossimità della superficie. Alcuni modelli per le due superfici così ottenute sono state proposte sulla base delle evidenze sperimentali. Tali modelli sono stati poi confrontati con calcoli DFT; in particolare, sono state generate simulazioni di immagini STM che sono state quindi confrontate con i dati sperimentali ed usate come valutazione finale della validità dei modelli proposti. La reattività delle leghe di superficie rispetto al CO è stata studiata sia sperimentalmente, mediante desorbimento termico programmato (TPD), sia ricorrendo a calcoli DFT. I risultati rivelano una scarsa reattività delle due superfici nei confronti del CO a causa dell’energia di adsorbimento inferiore rispetto alla stessa superficie di Pt (110) presa come riferimento; tale fenomenologia indica pertanto il promettente impiego di tali sistemi come catalizzatori caratterizzati da elevata tolleranza al CO.

Come già descritto per le leghe di superficie, i due ossidi superficiali (c(2 × 4) SnO_x / Pt (110) e c(4 × 2) SnO_x / Pt (110)), sono stati studiati mediante LEED, STM e SRPES. Alcuni modelli per le due superfici sono stati proposti sulla base dei risultati sperimentali, la cui validità è stata supportata da calcoli DFT. Il buon accordo tra le immagini STM simulate e i dati sperimentali suggeriscono una buona affidabilità delle strutture proposte.
La reattività verso il CO per le due fasi ossidate è stata inoltre indagata mediante TPD supportata da calcoli quantomeccanici. La struttura c(4 × 2), costituita da uno strato UT di SnO_x sub-stechiometrico, ha dimostrato di essere poco reattiva, mentre la fase più ossidata c(2 × 4) ha dimostrato di essere in grado di ossidare efficacemente il CO.
Lo studio della decomposizione del metanolo sulla fase c(2 × 4), effettuato mediante TPD e SRPES, indica come il metanolo possa essere ossidato in modo efficiente a CO_2 e H_2O. Tuttavia, i dati sperimentali indicano un meccanismo di ossidazione piuttosto complesso, la cui selettività cambia dinamicamente in base alle condizioni sperimentali. Ad ogni modo, la fase completamente ossidata c(2 × 4) può facilmente ossidare il metanolo a CO_2 già a bassa temperatura, tuttavia tale reattività viene progressivamente soppressa non

appena inizia la riduzione della fase con la perdita di ossigeno reticolare. In questo regime l'ossidazione del metanolo a CO_2 richiede temperature più elevate; in particolare, il meccanismo microscopico della reazione implica la fornitura di ossigeno da parte della fase c(2 × 4) ad isole ridotte di Pt o PtSn, siti nei quali avviene effettivamente la reazione di ossidazione. Con il procedere della decomposizione del metanolo, il progressivo consumo di ossigeno porta ad una drastica soppressione della diffusione di superficie di quest'ultimo. In questo modo, il metanolo viene semplicemente deidrogenato a CO e H_2 analogamente a quanto accade sulla superficie pulita di Pt (110), sebbene a temperature inferiori.

Parole chiave : celle a combustibile, leghe di superficie , ossidi di superficie , reattività verso il CO, decomposizione del metanolo.

Contents

1 Introduction

1.1 Energy crisis and solutions

Nowadays, the global economy relies on the traditional fossil fuel; however, excessive consumption of fossil fuel will lead to some terrible results. One of the disaster is the fast increasing temperature of the earth from recent 30~50 years, due to the emission of CO_2 from the consumption of fossil fuel [1]. The plot of global temperature and atmospheric CO_2 concentrations since 1880 is presented in Figure 1-1, indicating that the CO_2 concentration is the main factor for the increasing global temperature. The increasing temperature will cause some phenomena such as the melting of Antarctic ice and consequent rising sea level. Then the main cities near the coast will be flooded, as their positions are very low.

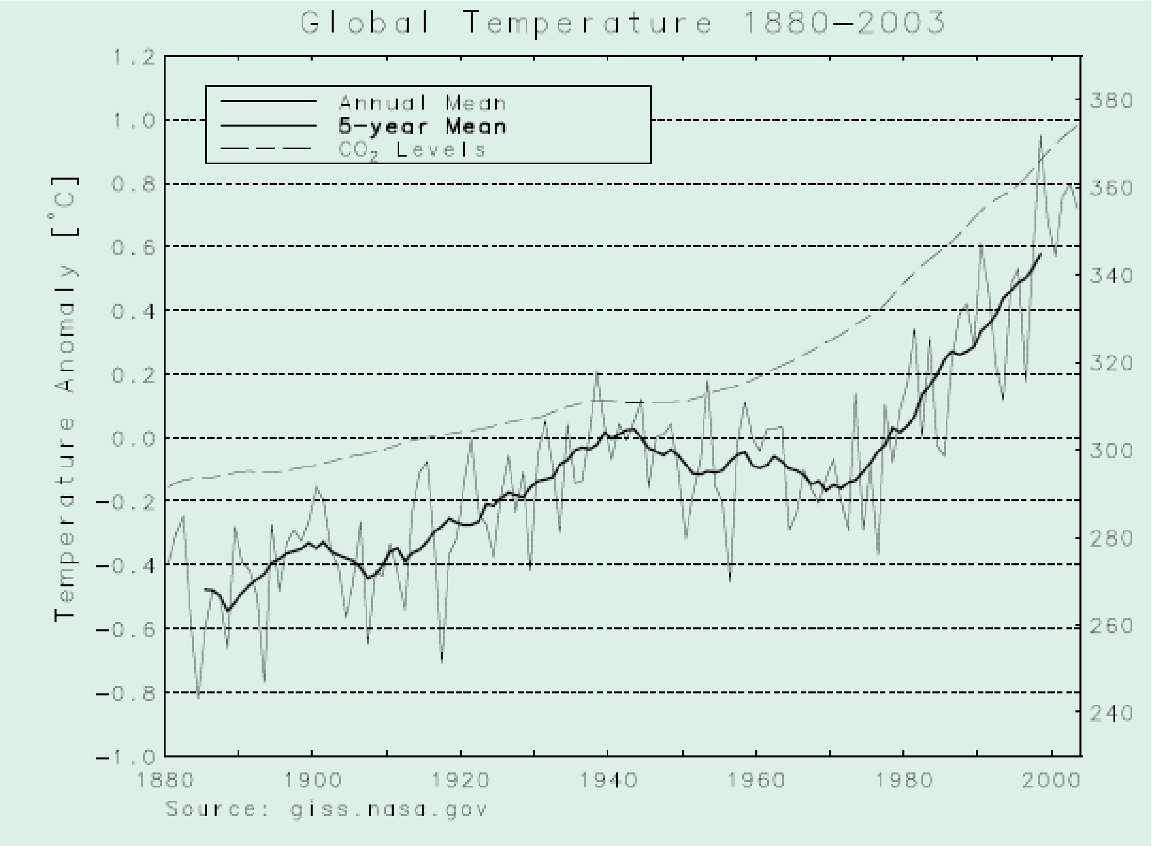

Figure 1-1 Michael Crichton's plot of global temperatures and atmospheric CO_2 concentrations since 1880.[1]

Besides, the air quality is deteriorating because of rising amount of cars which mainly use fossil fuel as their major power. Hence, finding energy sources alternative to fossil fuels is one of the biggest challenges for mankind in this century [2, 3]. Among several routes to satisfy the energy demand, fuel cells (FCs) have drawn much attention due to their high conversion efficiency[4], limited environmental impact[4] and solution to distributed energy requirements.

In this context, proton exchange membrane fuel cells (PEMFCs) are expected to be progressively used in daily applications.

1.2 Electrocatalysts and fuel cells

An electrocatalyst[5] is a catalyst that promotes electrochemical reactions [6]. Catalysts modify the rate of chemical reactions without being consumed in the process. Electrocatalysts are a specific form of catalysts deposited at electrode surface or may be the electrode surface itself. An electrocatalyst can be heterogeneous, such as a platinum surface or nanoparticles,[7-11] or homogeneous, like a coordination complex or enzyme[12-15]. The electrocatalyst assists in transferring electrons between the electrode and reactants, and/or facilitates an intermediate chemical transformation described by an overall half-reaction.

Figure 1-2 presents a typical structure of PEMFC~~[16]~~. According to the demonstrative figure, fuel such as H_2[17] or methanol[18] can be injected into anode, and the electrons from fuel can be consequently transferred to the electrode. Then the electrons go through the outside circle to the cathode to generate current, and H^+ transformed from H_2 transfers to cathode through the electrolyte present in the proton exchange membrane. In the cathode, O_2 and water can accept the electron from fuel and transform into OH^-, and finally react with transferred H^+ to form water exhaust.

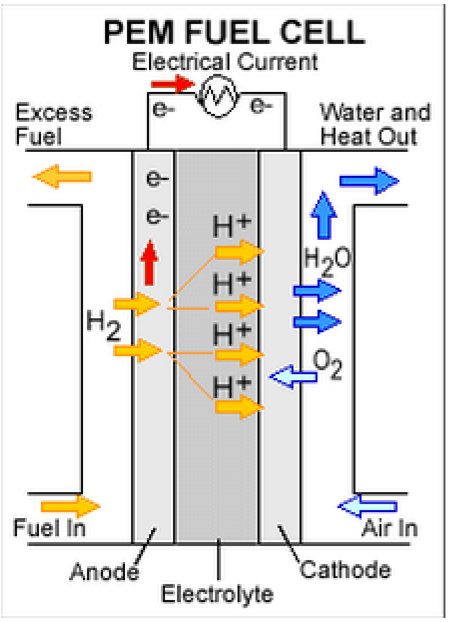

Figure 1-2 A demonstrative structure for typical PEMFCs.

1.2.1 Oxygen Reduction Reactions (ORR)

In cathode of PEMFC, air is pumped into the cell and oxygen is reduced on the cathode [19-23]. The ORR reaction consists in transferring four electrons from cathode to O_2 which is then transformed into OH^-, and then the OH^- can react with H^+ to form water during the reaction. The ORR reactions can be displayed as Equation 1-1.

$$O_2 + 4H^+ + 4e^- \rightarrow 2H_2O \qquad E^\theta = 1.23\text{V} \qquad \text{Equation 1-1}$$

1.2.2 Oxidation Reactions

For PEMFC, hydrogen [17, 24] and methanol [25-29] are the most used fuel due to their environmental friendly performance and to their abundance. However, H_2 always contains some trace of CO because of its preparation coming from reaction of water with coal or decomposition of methane. Hence, the CO oxidation reaction is also considered [30-34] and its presence can poison the electrode which is always made of Pt.

1.2.2.1 Hydrogen Oxidation Reactions (HOR)

In the electrochemical cell, hydrogen can be oxidized on the anode and then form proton. [34-37] The oxidation reactions can be described as Equation 1-2.

$$H_2 \rightarrow 2H^+ + 2e^- \qquad E^\theta = 0.00\text{V} \qquad \text{Equation 1-2}$$

Then, the proton can be transferred to cathode and react with OH^- which is the products from O_2 reduction reaction. So the total reaction of the fuel cells is showed as in Equation1-3.

$$2\boldsymbol{H_2} + \boldsymbol{O_2} \rightarrow 2\boldsymbol{H_2O} \qquad \boldsymbol{E^{\theta} = 1.23}\mathbf{V} \qquad \text{Equation 1-3}$$

1.2.2.2 Methanol Oxidation Reactions (MOR)

Methanol is another major fuel for PEMFC due to is convenient transportation and large supply from factory [38-42]. The MOR reaction [43, 44] implyes transferring of 6 electrons from methanol to anode and the transformation of methanol into CO_2 and H^+, which can be expressed as in Equation 1-4.

$$\boldsymbol{CH_3OH + H_2O \rightarrow 6H^+ + CO_2 + 6e^-} \qquad \boldsymbol{E^{\theta} = 0.02}\mathbf{V} \qquad \text{Equation 1-4}$$

So, the total reaction of the fuel cells can be showed as Equation 1-5.

$$\boldsymbol{CH_3OH + \frac{3}{2}O_2} \rightarrow 2\boldsymbol{H_2O + CO_2} \qquad \boldsymbol{E^{\theta} = 1.21}\mathbf{V} \qquad \text{Equation 1-5}$$

1.2.2.3 CO Oxidation Reactions (COOR) and CO stripping

As already mentioned, CO always exists in H_2 and it can be also one of the by-products during the MOR reaction[18]. But even trace amount of the gas can poison the electrode made of Pt and deteriorate the electrode performance dramatically. Hence, bimetallic electrocatalysts [32, 45-47] like Pt-Ru or Pt-Sn have attracted more attention due to their inhibition of CO poisoning. The promoting effect of alloyed M may be explained by two factors: functional and ligand (electronic) factors:

a) Bifunctional factor

The Pt atoms of alloy surfaces can adsorb CO very strongly. Hence, when some new metal is alloyed with Pt to form a bimetallic electrode, the second metal atom can promote the formation of–OH_{ad} on the surface, which, reacting with CO_{ad} on Pt atoms, can produce water and CO_2 [32, 48, 49]. The reaction can be described as Equation 1-6.

$$\boldsymbol{Pt - CO + M - OH \rightarrow H_2O + CO_2} \qquad \text{Equation 1-6}$$

The mechanism has been supported by many experimental results [25, 50, 51], and also explained by theoretical calculations [52, 53].

b) Ligand (electronic) factor.

The MOR performance of the bimetallic electrodes can be also explained considering a change in the electronic properties of Pt atoms which induce a CO absorption inhibition [26, 52, 54-56]. According to the mechanism, the alloyed metal atoms can decrease the adsorption energy of CO on Pt. Consequently, the CO can be easily desorbed from the surface, or it can be more easily removed by $–OH_{ad}$ present on the metal atoms close to Pt.

1.3 Bimetallic alloy electrocatalysts

Pt is the most popular material for electrode of FCs. However, durability and cost of the electrocatalysts for PEFMCs are still two open issues that restrict a pervasive diffusion of this technology [30, 57, 58]. As an example of the former, standard Pt-based electrocatalysts are quickly poisoned by CO [59, 60], one of the main impurities of the H_2 fuel. The replacement of Pt with cheaper catalysts, or at least its decrease, while maintaining the efficiency of current catalysts, is an open issue for the application of PEMFCs. The use of bimetallic catalysts [61] (either MM' or MM, where M'=noble metal and M=non-noble metal) is regarded as a promising route both to reduce the price [57, 62-65] and increase the durability of electrocatalysts [62, 66]. Ni[19] and Co[9] are two of the most popular alloyed metals for cathodes in PEMFC due to their excellent ORR performance after alloying with Pt. In particular, PtSn alloys [32, 48, 49, 67] have been considered as the most promising candidates to avoid CO poisoning [68-71] and with the best performance in alcohol oxidation [28, 72].

In order to optimize the activity/durability of bimetallic *real* electrocatalysts (i.e. PtSn alloy nanoparticles on a support [73-75]) a reductionist surface science based approach applied to appropriate model electrocatalysts offers a rationally-oriented route: surfaces of single crystal alloys [76-78] and their oxides [79, 80] or, alternatively, surface alloys and oxides can be fabricated with atomic scale precision by evaporating one of the two metals on a single crystal of the other, followed by thermal annealing. The processes occurring on such model electrocatalysts (such as alloying, corrosion or redox processes) can be efficiently monitored by the tools offered by modern surface science and the results transferred to *real* cases.

1.3.1 Deposition of metals on low index Pt surface

Alloying Pt with transition elements can provide better electrocatalysts and also reduce the load of Pt[7, 9, 81-84]. So, research on alloyed electrodes are increasing fast[85, 86], while more basic studies about the effect of alloyed elements were completed on PtM model catalysts prepared on various low index Pt surface (M= non-noble elements) [28, 80, 85, 87-89]. Ni is one of the most studied metals deposited on low index Pt surface, especially on Pt(111) surface[90-93]. According to these studies, the low index surface alloys exhibit excellent ORR performance. Markovic et. al has done systematic investigations in PtNi alloys, indicating that ORR current can be strongly enhanced,even more than a factor of 10. Alloying Co with low index Pt surface is another hot topic due to the enhancement of ORR performance [94-97]. Also, Pt electrodes alloyed with Ni or Co performs better than Pt for MOR [98], due to the introduction of the already mentioned factors and also to the facilitated decomposition of methanol (according to Thermal Programmed Desorption, TPD, investigations). Besides, adopting Sn as one of alloyed elements[32, 49, 69] with Pt is becoming an attractive topic to be investigated, as Sn can split water [52, 99] and reduce adsorption energy of CO on the Pt-M alloy electrode[55, 56]. Some basic investigations have been published on various low index Pt surface [2, 72, 77, 89, 100-104].

1.3.2 PtSn/Pt(111) surface alloys and their oxidized surface

Pt(111) is one of the most studied model catalyst surface because it represent the most abundant exposed surface in Pt nanoparticles and many papers have appeared in literature [105-110] So, PtSn/Pt(111) phase diagram [111-113] were accurately investigated.

1.3.2.1 Phase diagram

When various amount Sn is deposited on the Pt(111) surface, the p(2×2) and $(\sqrt{3} \times \sqrt{3})$R30° reconstructions can be observed by LEED, reported by Paffett et.al [114] about 25 years ago. After this paper, a lot of further studies were accomplished on the two surface alloys [111, 113, 115, 116]. Some theoretical studies were also reported based on the Tight-Binding Ising Model (TBIM) and a mean-field approximation [113]. According to the literature, the p(2×2) pattern can be prepared at lower Sn coverage compared to the $(\sqrt{3} \times \sqrt{3})$R30° one. Similar results are also reported in other studies [113, 117, 118]. Besides, some papers reported on the oxidation of the reconstructed PtSn(111) surfaces[119-126]. Batzill et al. [118, 120-122, 125] reported that oxidation of the $(\sqrt{3} \times \sqrt{3})$R30 surface forms a (5×5) pattern, while a more severe oxidation takes to a (4×4) reconstruction. After further oxidation at 900K, a monolayer wetting layer of tin oxide completely covers the substrate, and a 3D ordered structure on the surface can be obtained after oxidation with more oxygen exposure. Annealing of these oxidized surfaces at high temperature results in complete decomposition of SnO_x species and the p(2×2) pattern can be again observed by LEED and STM[122]. Hence, according to the above results, the phase diagram of PtSn(O) on Pt(111) surface can be also summarized as in Figure 1-3.

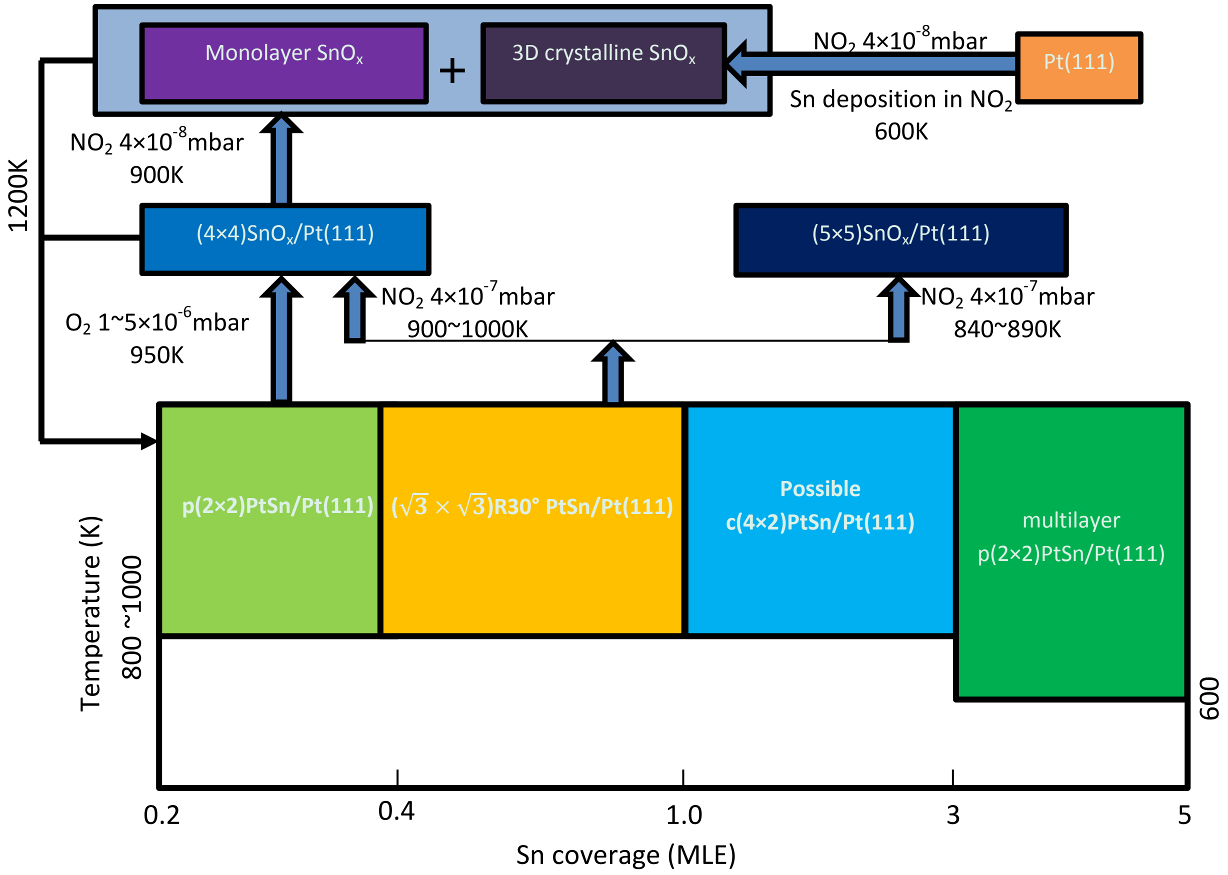

Figure 1-3 Phase diagram for PtSn/Pt(111) surface alloys and their SnO_x/Pt(111) oxides.

a. p(2×2)PtSn/Pt(111) surface

According to the phase diagram in Figure 1-3, after depositing 0.2~0.4ML Sn on Pt(111) surface at certain temperature and consequent annealing at about 800~1000K, a p(2×2) reconstructed pattern (see Figure 1-4(c)) can be observed[114, 120]. After the first report of the structure by Paffett et al. [114] in 1986, some similar works about reconstructed surface were also published [111, 113-117, 127-129]. The characterizations by XPD [116], LEED-IV [113], STM [118] and low-Energy Ion-Scattering [128] provide an evidence for the incorporation of Sn into the outermost Pt layer forming a two-dimensional ordered alloy surface. A typical image of the structure were presented as Figure 1-5(a) by Overbury et al. [128], and it was commonly also supported by other investigations[113, 128].

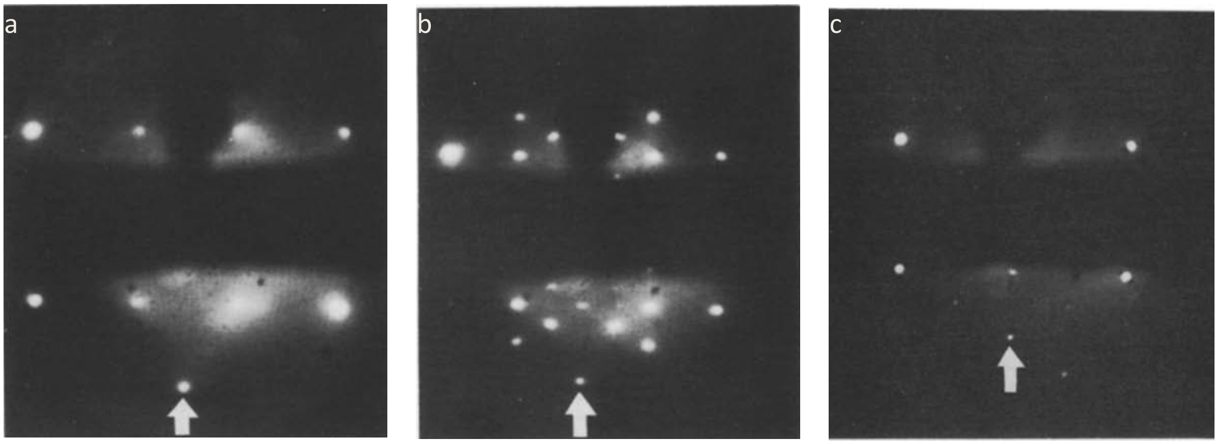

Figure 1-4 Typical LEED patterns : (a) the $(\sqrt{3}\times\sqrt{3})R30°$, (b) the c(4×2) patterns and (c) p(2×2) [114]

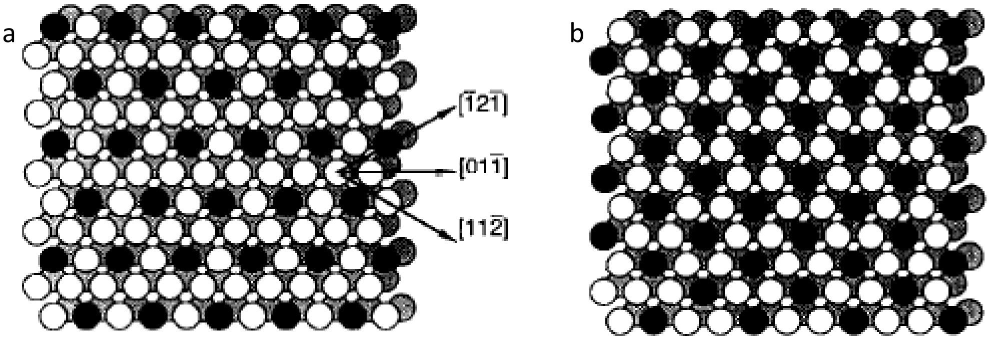

Figure 1-5 Structures for various reconstructed PtSn/Pt(111) surfaces are shown: p(2×2) (a) and $(\sqrt{3}\times\sqrt{3})R30°$ (b). Dark circles represent Sn atoms; open and shaded circles represent first and second layer Pt atoms, respectively [116].

b. Multilayer p(2×2) reconstructed surface

Multilayer p(2×2) reconstructed surface can be obtained when 3~5ML Sn are deposited on Pt(111) surface with subsequent annealing at about 600K, which was reported by Galeotti, et al. [116]. The reconstructed surface can be transformed into $(\sqrt{3} \times \sqrt{3})R30°$ pattern after higher temperature annealing to 800K. A similar work was published by Gallis et al. [111] where they annealed the sample covered with 3ML Sn at about 1000K for few seconds, and a $(\sqrt{3} \times \sqrt{3})R30°$ pattern was observed after annealing at 1000K for longer time, probably due to decrease of Sn amount on the surface by Sn diffusion into the bulk.

c. $(\sqrt{3} \times \sqrt{3})R30°$ PtSn/Pt(111) surface

$(\sqrt{3} \times \sqrt{3})R30°$ PtSn/Pt(111) reconstruction, whose LEED pattern is shown in Figure 1-5(a), was first reported in 1986 by Paffett et al. [114]. It can be obtained with a coverage of about 0.4ML Sn deposited on Pt(111) surface at a substrate temperature of 320K[128]. The surface structure was also characterized with various tools and thoroughly discussed [113-116, 128, 130]. According to the investigations, Sn is incorporated into the first Pt layer forming a two-dimensional ordered alloy surface and its structure is presented in Figure 1-5(b): it exhibits a slight buckling where Sn protrudes about 0.022±0.005nm above the plane of the first-layer Pt atoms [116]. The same reconstruction was also reported by Philip et al. starting from a Pt_3Sn bulk alloy [29, 115, 131].

d. c(4×2) PtSn/Pt(111) surface

The reconstruction was also first reported in 1986 by Paffett et al. [114], and the typical pattern is shown in Figure 1-4(b). It can be prepared from Pt(111) surface with about 0.5ML Sn coverage at low tempareture and then annealed to 1000K. The same preparation procedure has been also suggested by Gallis et al.[111].

e. (5×5) SnO_x/Pt(111) surface

After oxidation of $(\sqrt{3}\times\sqrt{3})$R30° PtSn/Pt(111) reconstruction with NO_2 at 4×10^{-7}mbar for several adsorption cycles, the surface can be transformed into (5×5) SnO_x/Pt(111) one [118, 120-122, 132] which is first reported by Batzill et al.[120]. The STM image of the surface was reported (see Figure 1-6). According to the topography, the surface presents point defects on an ordered (5×5) renconstructed surface sitting on a p(2×2) reconstructed substrate.

f. (4×4) PtSn/Pt(111) surface

After oxidizing the p(2×2) and the $(\sqrt{3}\times\sqrt{3})$R30° reconstructed surfaces, a (4×4) reconstructed surface can be prepared [120-122, 124, 133]. STM images were obtained and some typical STM images are displayed in Figure 1-6 [120, 124, 133]. A structural model has been proposed by Hoheisel et al. in agreement with the XPD and STM data, and it is presented in Figure 1-6(d) [133].

g. Some other surfaces

Some other ordered structures including (4×6) and (4×8) were identified from STM images reported by Batzill et al.[120], but details are not presented herein.

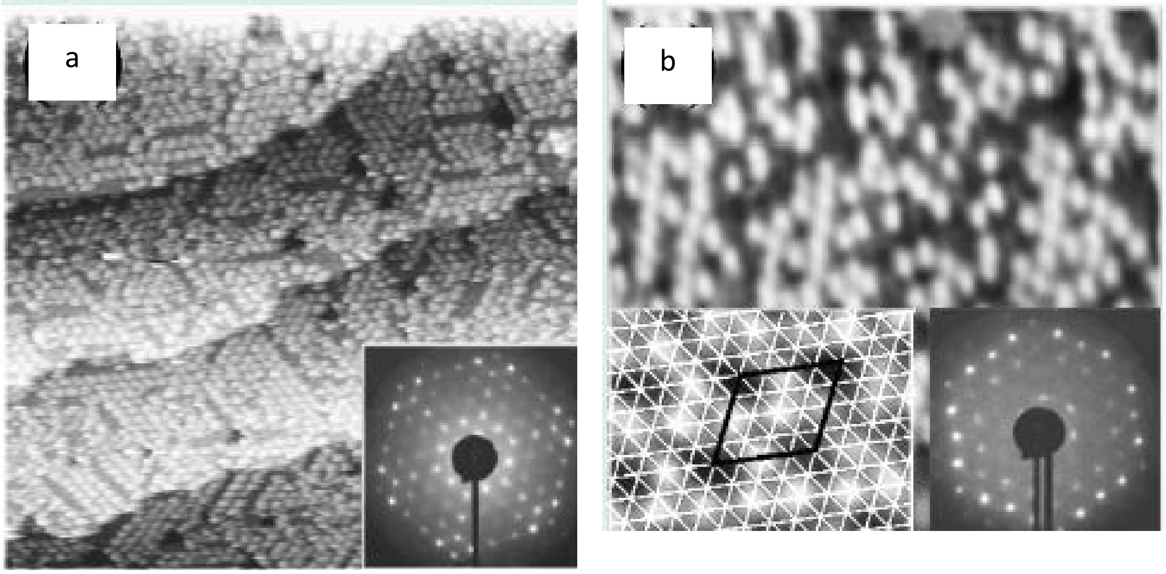

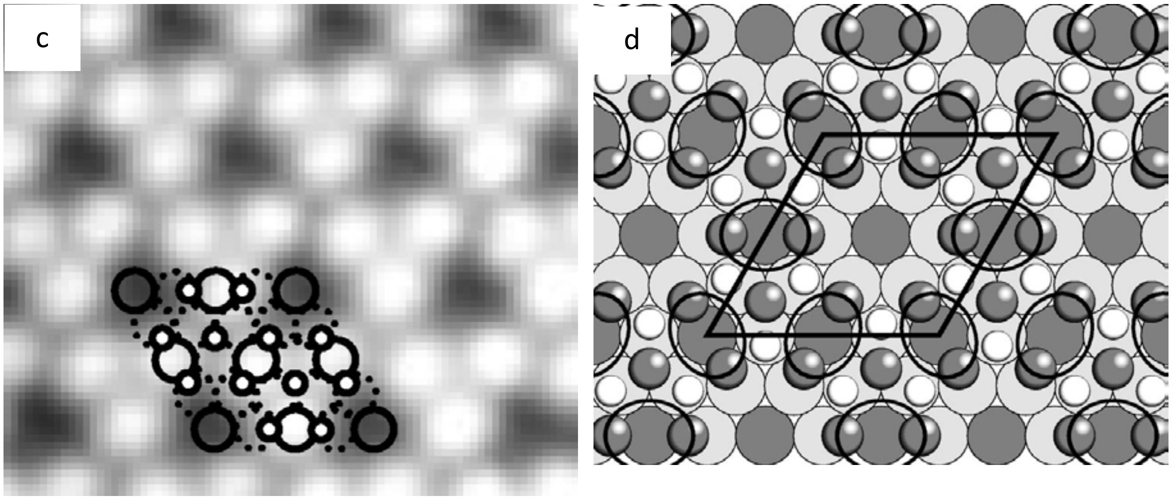

Figure 1-6 Typical STM and LEED images: (a) (5×5) reconstructed surface (62nm×62nm) and (b) (4×4) reconstructed surface (12nm×12nm)(b) [120]; (c) atomic (4×4) reconstructed surface with structural model and (d) schematic model of the (4×4) phase.[133].

1.3.2.2 Chemical and electrochemical reactivity

After discovery of the reconstructed patterns on Pt(111) surface, a lot of work [56, 114, 127, 129, 134, 135] was carried out to investigate their catalytic activities. However, most of the work is focused on the two most popular surface alloys: the p(2×2) and the $(\sqrt{3}\times\sqrt{3})$R30. Also some investigations about electrocatalysis of the two surface alloys were reported [29, 136-138], while a few papers about activities of SnO_x on Pt(111) were published in recent years [28, 72, 80, 139].

a. Catalytic activities of the surface alloys

After the first report of the surface alloys, their reactivity with various gases was tested [107, 108, 135, 140, 141] and the surfaces exhibit reduction of adsorption energies of the dosing species due to the electronic effect [56, 107, 108, 127, 142-145]. Alloying Sn with Pt(111) surface can lower the adsorption energies of CO[56, 131, 146], which can also explain the high performance for carbon oxidation reaction in the electrochemical cells and is also confirmed by some theoretical results [31, 147].

Besides, the surface exhibit very high selectivity for some reactions, such as hydrogenation [148] and dehydrogenation [149].

b. Electrochemical activities of the surface alloys

With the two surface alloys electrodes were also prepared and tested in electrochemical cells [29, 136, 143] with respect to COOR [31, 150, 151], MOR[29] and EOR[101, 137]. According to the works by Markovic et al. [29, 136], the addition of Sn in the Pt(111) surface can electro-oxidize carbon monoxide efficiently due to the bifunctional effect. The study of MOR [29] and EOR [137] on the two surfaces demonstrates an excellent activity.

c. Catalytic activities of the oxides

In recent years, reactivity studies were published on the ordered SnO_x/Pt(111) [28, 29, 72, 80, 139]. Axnanda et al. found that the Sn(II)O is playing a key role for the high COOR performance of the SnO_x/Pt(111) surface[80]. Also the electrocatalytical activity toward EOR is highly enhanced after adding SnO_x to the Pt surface[101].

1.3.3 PtSn/Pt(100) surface alloys and their oxidized surface

Some reconstructed PtSn surface alloy on Pt(100) have also been reported [102, 152-155] even if the number of publications is less than the one on the Pt(111) surface.

1.3.3.1 Phase diagram

According to the works of Koel et al.[102, 153, 156], addition of Sn at various coverage on Pt(100) can produce several reconstructed surfaces: an overlayer c(2×2), an incorporated c(2×2) and $(3\sqrt{3} \times 3\sqrt{3})R45°$. According to preparation parameters, the phase diagram of Pt(100) surface can be obtained (see Figure 1-7).

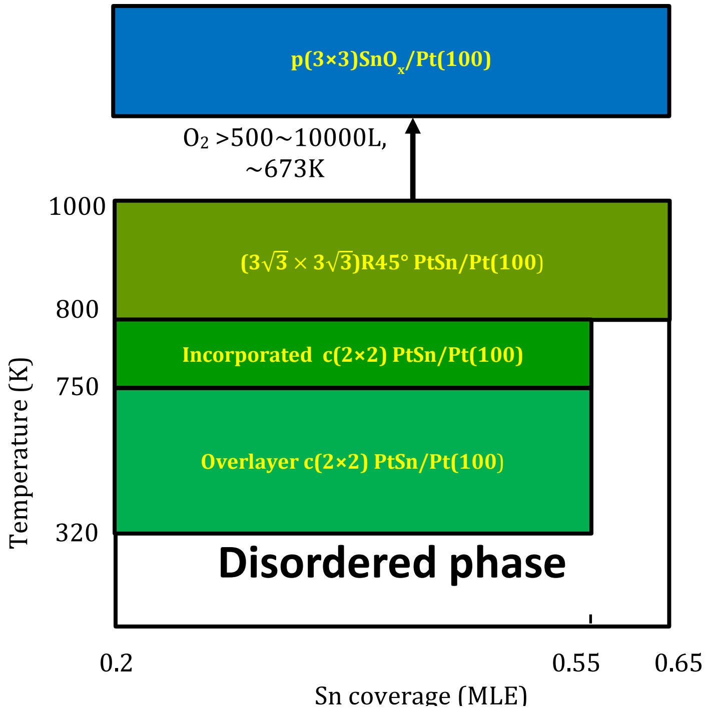

Figure 1-7 Phase diagram for PtSn/Pt(100) surface alloys and their SnO_x/Pt(100) oxides.

a. c(2×2)PtSn/Pt(100) overlayer surface alloy

The surface was reported for the first time by Haner et al. [157]: after depositing 0.2~0.55ML Sn on the Pt(100) surface and consequent annealing to 600~750K[153, 156], a c(2×2) pattern can be observed and its typical LEED, STM images, and atomic model [102] are shown in Figure 1-8. With increasing annealing temperature, the pattern becomes more clear which has been interpreted as an incorporated c(2×2) reconstruction of the outermost surface layers. If further annealing to 850K is applied, the surface can transform to the well-known $(3\sqrt{2}\times\sqrt{2})R45°$ pattern [102, 156, 157].

b. Incorporated c(2×2)PtSn/Pt(100) surface alloy

The incorporated c(2×2)PtSn/Pt(100) surface alloy was identified [156] after the first report of the c(2×2) pattern [157]. The surface can be prepared from annealing the overlayer c(2×2) surface to 800K [102, 156]. It has been also reported [155] that the surface with high Sn coverage had numerous pyramids on the surface and some atomic lines can form on the flat plane after heating to 1000K. Some typical STM images, LEED pattern and atomic models [102] are presented in Figure 1-9.

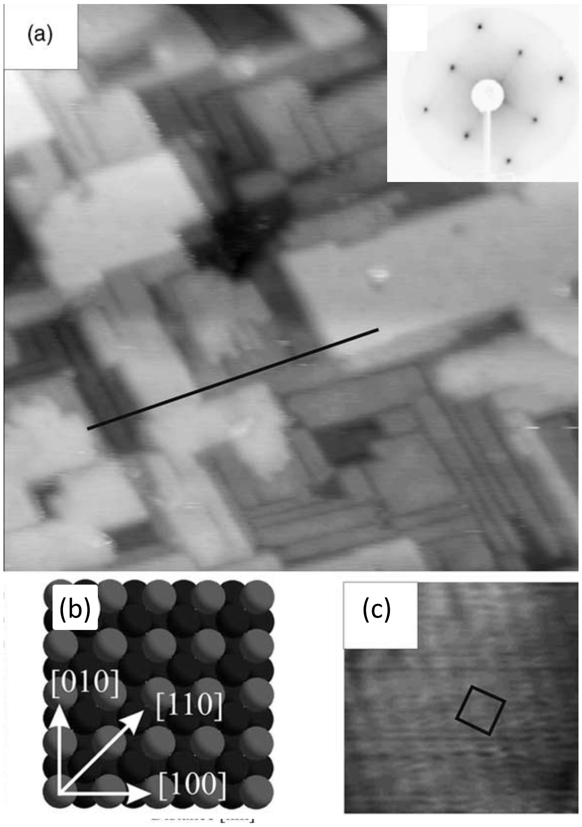

Figure 1-8 Typical STM image, LEED pattern and model of overlayer c(2×2) PtSn/Pt(100) surface.

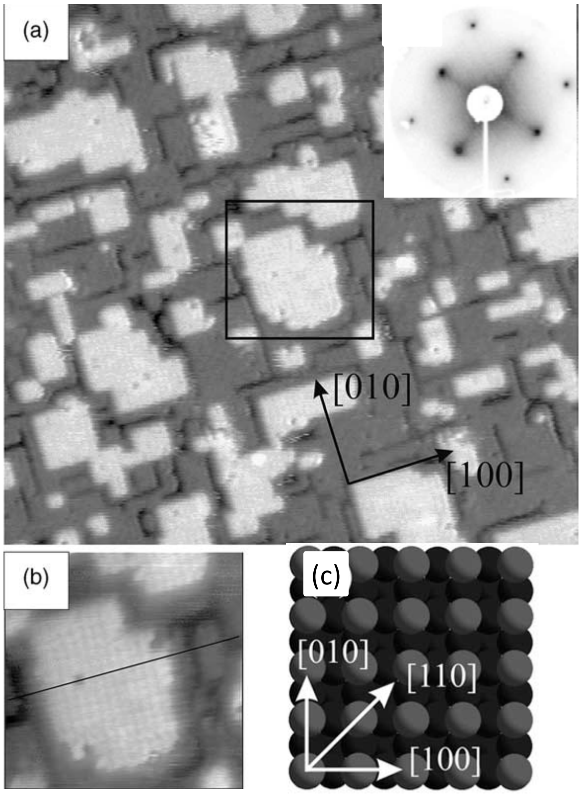

Figure 1-9 Typical STM image, LEED pattern and model of incorporated c(2×2) PtSn/Pt(100) surface.

c. $\left(3\sqrt{2}\times\sqrt{2}\right)R45°$PtSn/Pt(100) surface

The $\left(3\sqrt{2}\times\sqrt{2}\right)$R45° reconstruction was prepared from higher coverage Sn and annealing the sample above 800K [102, 153, 155-157]: its STM images, LEED pattern and atomic model are reported by Batzilland et al. [102] and shown in Figure 1-10. The STM images display some dark channels consisting of three missing Pt row on the reconstructed surface [102]. The surface is identified as one of the most stable surface [156]. The surface can be oxidized with large O_2 exposure and a p(3×3) pattern can be prepared [153].

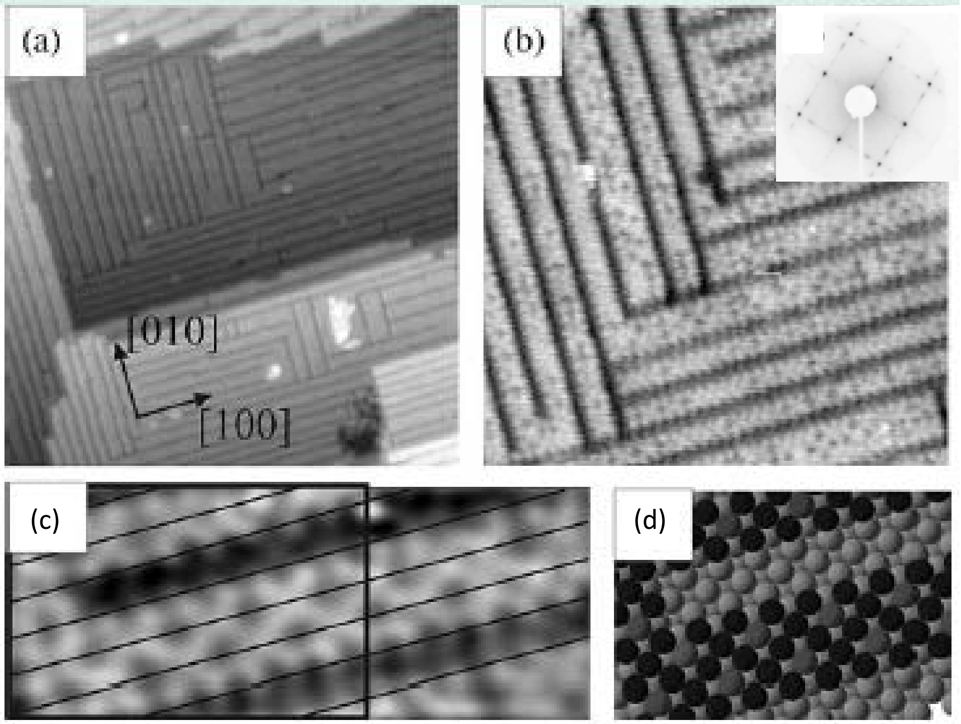

Figure 1-10 Typical STM image, LEED pattern and model o$(3\sqrt{2} \times \sqrt{2})R45°$ PtSn/Pt(100) surface.

d. p(3×3)SnO_x/Pt(100) surface oxides

Only one reconstructed pattern was reported [153] after oxidation of the surface alloys discussed above at about 673K. A further short report [104] has been reported on the surface oxides.

1.3.3.2 *Chemical and electrochemical reactivity*

Some gases were dosed on the surface of the reconstructed PtSn/Pt(100) surface, such as NO [158], CO [154] and acetylene [103, 159]. It has been shown that the addition of Sn can reduce the adsorption energy of the species on the Pt(100) surface. Also adding Sn into the Pt(100) surface can deactivate decomposition of acetylene [103, 159]: no decomposition of the gas on the overlayer c(2×2)PtSn/Pt(100) surface alloyhas been observed .

1.3.4 PtSn/Pt(110) surface alloys and their oxidized surface

The Pt(110) surface is by far the less studied one. The reconstructed surfaces of PtSn(110) were always prepared from Pt_3Sn bulk alloy [2, 78, 115, 136], and a reconstructed surface oxide was prepared on the $Pt_3Sn(110)$ from the bulk alloy [79]. They shows enhanced CO oxidation in solution. Also the effect of addition of Sn into the Pt(110) surface is to decrease the adsorption energy of CO on Pt [78, 136, 150].

1.3.4.1 Surface alloys and nano-oxides

a. p(4×1)PtSn/Pt(110)

Until now, only the p(4×1)PtSn/Pt(110) reconstructed surface alloy has been reported having a sharp LEED pattern with addition of Sn into Pt(110) [76, 77]. The surface is characterized by synchrotron radiation (SR) photoemission spectra (SRPES) and STM, and it was studied with DFT calculation. According the work of Agnoli and et al, [77], after deposition of 0.75ML Sn the p(4x1) LEED pattern and the STM images shown in Figure 1-11 are obtained. Also, the same authors propose a DFT derived model of the surface reconstruction.

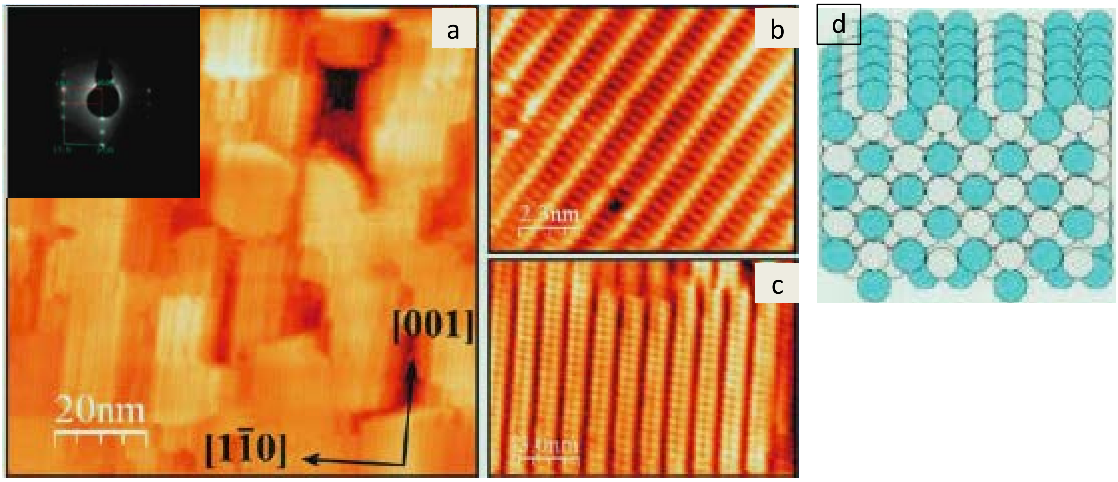

Figure 1-11 Typical STM images, LEED pattern and model of p(4×1)PtSn/Pt(110)[77]

b. p(2×2)PtSn/Pt(110)

Beside the p(4×1) reconstructed surface, von Schenck et al. reported an ordered surface with p(2×2) reconstruction characterized by STM, but no clear LEED pattern can be observed [100, 160]. The surface contains Pt-Sn-Pt along the [1$\bar{1}$0] direction and the Sn addition cause the roughing of Pt(110) surface.

c. c(4×2)SnO_x/Pt_3Sn(110)

A c(4×2) LEED pattern was observed from the Pt_3Sn(110) surface after annealing in O_2 with exposure of thousands Langmuir [79]. The surface has an additional c(2×2) superstructure with respect to the p(2×2) of Pt_3Sn(110) substrate. According to the STM images, the surface topography contains boundaries between the domains. Figure 1-12 presents typical LEED pattern and STM images of the nano-oxides [79].

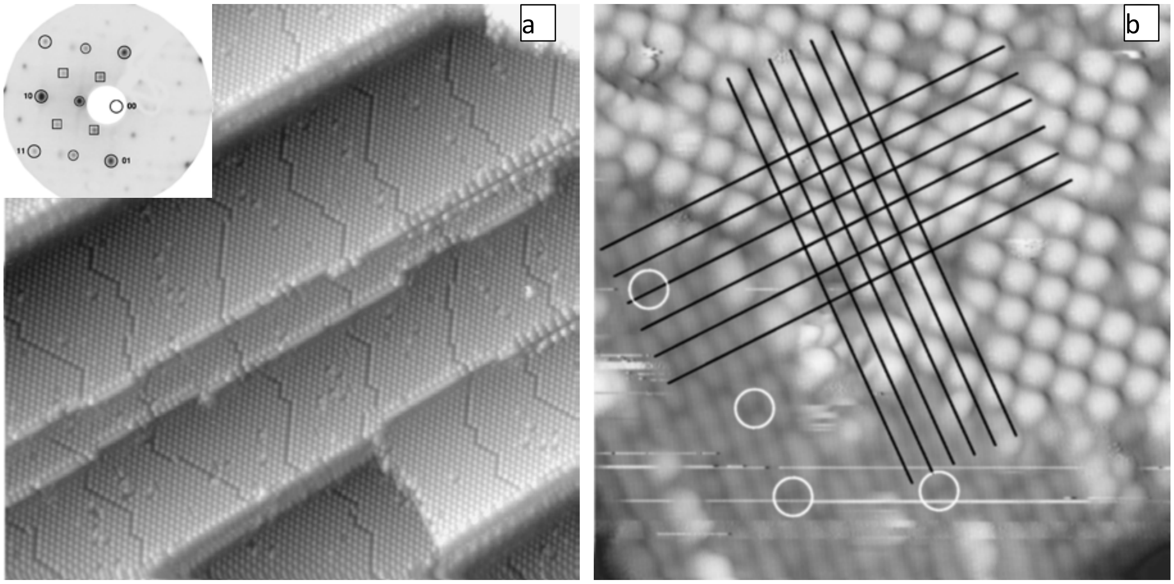

Figure 1-12 Typical STM images, LEED pattern of c(4×2) SnO_x/Pt_3Sn(110)[79]

d. some other patterns from Pt_3Sn bulk alloy

After sputtering and annealing Pt_3Sn(110) bulk alloys, p(3×1) and p(2×1) patterns were observed [150]. Besides, Hoheisel et al. [2] reported a surface with a mixed patterns containing p(2×1) and p(1×1) reconstructions and the surface was characterized with STM and LEED.

1.3.4.2 Chemical and electrochemical reactivity

Only few chemical characterizations have been reported. Surfaces were investigated with CO as a probe [100] or by theoretical calculation [78, 161]. Based on the results, the C1s of CO has similar binding energy after adsorbing on the p(2×2) reconstructed Sn terminated Pt(110) surface. Theoretical results indicate the adding of Sn can reduce the adsorption energy of CO on the Pt but no modification on adsorption sites. According to COOR tests of the reconstructed surfaces from $Pt_3Sn(110)$ surface alloys in the electrochemical cells [136, 150], the surfaces perform very high COOR reactivity.

1.4 Thesis Outline

According the above panorama, only a few papers were focusing on the PtSn(O) system on Pt(110), while the Pt(110) exhibits very high MOR reactivity. Hence, it is very worth to further investigate modification the Pt(110) surface with Sn to understand if the data obtained on the Pt(111) and Pt(100) surface alloys can be also transferred on the Pt(110) surface. The present thesis focuses on studying structure/morphology/activity relationships in bimetallic Pt-Sn nanostructured electrodes for proton exchange membrane (PEM) fuel cells by adopting a rigorous surface science approach where:

i) Model electrocatalysts are prepared in ultra-high-vacuum (UHV) conditions as ultrathin (UT) films ($PtSn_x$/Pt(110) and SnO_x/Pt(110)) to ensure a very reproducible control down to the atomic level;

ii) Composition, morphology and structure of the UT nanostructured films are studied *in situ* by adopting state-of-the-art characterization tools, i.e. photoemission spectroscopy, scanning probe microscopy and spectroscopy, once again down to the atomic level;

iii) Quantum mechanical calculations were done adopting the Density Functional theory (DFT) in order to derive model structures of the UT films;

References

[1] B.W. Rust, Computing Science and Statistics, , Volume 37.
[2] M. Hoheisel, S. Speller, J. Kuntze, A. Atrei, U. Bardi, W. Heiland, Phys Rev B, 63 (2001).
[3] G. Kolb, Introduction and Outline, in: Fuel Processing, Wiley-VCH Verlag GmbH & Co. KGaA, 2008, pp. 1-2.
[4] J. Kunze, U. Stimming, Angewandte Chemie International Edition, 48 (2009) 9230-9237.
[5] Wikipedia, http://en.wikipedia.org/wiki/Electrocatalyst.
[6] J.O.M. Bockris, Z.S. Minevski, Electrochim Acta, 39 (1994) 1471-1479.
[7] GreeleyJ, I.E.L. Stephens, A.S. Bondarenko, T.P. Johansson, H.A. Hansen, T.F. Jaramillo, RossmeislJ, ChorkendorffI, J.K. Nørskov, Nat Chem, 1 (2009) 552-556.
[8] J. Zhang, K. Sasaki, E. Sutter, R.R. Adzic, Science, 315 (2007) 220-222.
[9] V.R. Stamenkovic, B.S. Mun, M. Arenz, K.J. Mayrhofer, C.A. Lucas, G. Wang, P.N. Ross, N.M. Markovic, Nat Mater, 6 (2007) 241-247.
[10] J. Greeley, T.F. Jaramillo, J. Bonde, I.B. Chorkendorff, J.K. Norskov, Nat Mater, 5 (2006) 909-913.
[11] N.M. Markovic, P.N. Ross, Surf Sci Rep, 45 (2002) 121-229.
[12] H. Luo, S. Jin, P.H. Fallgren, H.J. Park, P.A. Johnson, Chem Eng J, 165 (2010) 524-528.
[13] E. Lojou, X. Luo, M. Brugna, N. Candoni, S. Dementin, M.T. Giudici-Orticoni, J Biol Inorg Chem, 13 (2008) 1157-1167.
[14] F. Colmati, S.A. Yoshioka, V.L.V.B. Silva, H. Varela, E.R. Gonzalez, Int J Electrochem Sc, 2 (2007) 195-202.
[15] K.A. Vincent, J.A. Cracknell, A. Parkin, F.A. Armstrong, Dalton T, (2005) 3397-3403.
[16] Wikipedia.
[17] M.K. Debe, Nature, 486 (2012) 43-51.
[18] Z.D. Wei, L.L. Li, Y.H. Luo, C. Yan, C.X. Sun, G.Z. Yin, P.K. Shen, The Journal of Physical Chemistry B, 110 (2006) 26055-26061.
[19] C. Wang, N.M. Markovic, V.R. Stamenkovic, ACS Catalysis, 2 (2012) 891-898.
[20] V. Viswanathan, H.A. Hansen, J. Rossmeisl, J.K. Nørskov, ACS Catalysis, (2012) 1654-1660.
[21] S. Kondo, M. Nakamura, N. Maki, N. Hoshi, J Phys Chem C, 113 (2009) 12625-12628.
[22] T.J. Schmidt, V. Stamenkovic, J.P.N. Ross, N.M. Markovic, Phys Chem Chem Phys, 5 (2003) 400-406.
[23] H.A. Gasteiger, P.N. Ross, The Journal of Physical Chemistry, 100 (1996) 6715-6721.
[24] K. Tedsree, T. Li, S. Jones, C.W.A. Chan, K.M.K. Yu, P.A.J. Bagot, E.A. Marquis, G.D.W. Smith, S.C.E. Tsang, Nat Nanotechnol, 6 (2011) 302-307.
[25] G.X. Wang, T. Takeguchi, Y. Zhang, E.N. Muhamad, M. Sadakane, S. Ye, W. Ueda, J Electrochem Soc, 156 (2009) B862-B869.
[26] E. Antolini, E.R. Gonzalez, Catal Today, 160 (2011) 28-38.
[27] D.K. Kang, C.S. Noh, N.H. Kim, S.H. Cho, J.M. Sohn, T.J. Kim, Y.K. Park, J Ind Eng Chem, 16 (2010) 385-389.
[28] W.-P. Zhou, W. An, D. Su, R. Palomino, P. Liu, M.G. White, R.R. Adzic, The Journal of Physical Chemistry Letters, (2012) 3286-3290.
[29] A.N. Haner, P.N. Ross, J Phys Chem-Us, 95 (1991) 3740-3746.
[30] Z.H. Teng, G. Wang, B. Wu, Y. Gao, J Power Sources, 164 (2007) 105-110.
[31] P. Liu, A. Logadottir, J.K. Nørskov, Electrochim Acta, 48 (2003) 3731-3742.
[32] V. Radmilovic, T.J. Richardson, S.J. Chen, P.N. Ross Jr, J Catal, 232 (2005) 199-209.
[33] N.M. Markovic, A. Widelov, P.N. Ross, O.R. Monteiro, I.G. Brown, Catal Lett, 43 (1997) 161-166.
[34] H.A. Gasteiger, N.M. Markovic, P.N. Ross, J Phys Chem-Us, 99 (1995) 8945-8949.

[35] Z. Radovic-Hrapovic, G. Jerkiewicz, J Electroanal Chem, 499 (2001) 61-66.
[36] N.M. Markovic, N.S. Marinkovic, R.R. Adzic, J Electroanal Chem, 241 (1988) 309-328.
[37] N.M. Markovic, N.S. Marinkovic, R.R. Adzic, J Electroanal Chem, 314 (1991) 289-306.
[38] Y. Chen, G.J. Zhang, J.A. Ma, Y.M. Zhou, Y.W. Tang, T.H. Lu, Int J Hydrogen Energ, 35 (2010) 10109-10117.
[39] Y.L. Du, K.L. Lv, B.Q. Su, N.O. Zhang, C.M. Wang, J Appl Electrochem, 39 (2009) 2409-2414.
[40] Q. Jiang, L.H. Jiang, J. Qi, S.L. Wang, G.Q. Sun, Electrochim Acta, 56 (2011) 6431-6440.
[41] K. Ke, K. Waki, J Electrochem Soc, 154 (2007) A207-A212.
[42] W. Gao, X. Li, Y. Li, X. Wang, S. Song, H. Zhang, CrystEngComm, (2012).
[43] K. Wang, H.A. Gasteiger, N.M. Markovic, P.N. Ross Jr, Electrochim Acta, 41 (1996) 2587-2593.
[44] A. Aramata, M. Masuda, T. Kodera, J Electrochem Soc, 136 (1989) 3288-3296.
[45] T. Sato, K. Kunimatsu, M. Watanabe, H. Uchida, J Nanosci Nanotechno, 11 (2011) 5123-5130.
[46] W. Yu, M.D. Porosoff, J.G. Chen, Chem Rev, 112 (2012) 5780-5817.
[47] E. Lee, A. Murthy, A. Manthiram, J Electroanal Chem, 659 (2011) 168-175.
[48] N.M. Markovic, A. Widelôv, P.N. Ross, O.R. Monteiro, I.G. Brown, Catal Lett, 43 (1997) 161-166.
[49] M. Arenz, V. Stamenkovic, B.B. Blizanac, K.J. Mayrhofer, N.M. Markovic, P.N. Ross, J Catal, 232 (2005) 402-410.
[50] G.X. Wang, T. Takeguchi, E.N. Muhamad, T. Yamanaka, W. Ueda, J Electrochem Soc, 158 (2011) B448-B453.
[51] G.X. Wang, T. Takeguchi, T. Yamanaka, E.N. Muhamad, M. Mastuda, W. Ueda, Appl Catal B-Environ, 98 (2010) 86-93.
[52] Y. Ishikawa, M.-S. Liao, C.R. Cabrera, Surf Sci, 463 (2000) 66-80.
[53] T.E. Shubina, M.T.M. Koper, Electrochim Acta, 47 (2002) 3621-3628.
[54] T. Frelink, W. Visscher, J.A.R. van Veen, Surf Sci, 335 (1995) 353-360.
[55] M.T. Paffett, S.C. Gebhard, R.G. Windham, B.E. Koel, The Journal of Physical Chemistry, 94 (1990) 6831-6839.
[56] C. Xu, B.E. Koel, Surf Sci, 304 (1994) L505-L511.
[57] C. Wang, N.M. Markovic, V.R. Stamenkovic, ACS Catalysis, (2012) 891-898.
[58] N. Tian, Z.-Y. Zhou, S.-G. Sun, Y. Ding, Z.L. Wang, Science, 316 (2007) 732-735.
[59] D.R. Butcher, M.E. Grass, Z. Zeng, F. Aksoy, H. Bluhm, W.-X. Li, B.S. Mun, G.A. Somorjai, Z. Liu, J Am Chem Soc, 133 (2011) 20319-20325.
[60] C. Spiel, D. Vogel, Y. Suchorski, W. Drachsel, R. Schloegl, G. Rupprechter, Catal Lett, 141 (2011) 625-632.
[61] B. Beden, F. Kadirgan, C. Lamy, J.M. Leger, Journal of Electroanalytical Chemistry and Interfacial Electrochemistry, 127 (1981) 75-85.
[62] W. Zhang, R. Wang, H. Wang, Z. Lei, Fuel Cells, 10 (2010) 734-739.
[63] X. Zhang, H. Wang, J. Key, V. Linkov, S. Ji, X. Wang, Z. Lei, R. Wang, J Electrochem Soc, 159 (2012) B270-B276.
[64] M. Ammam, L.E. Prest, A.D. Pauric, E.B. Easton, J Electrochem Soc, 159 (2012) B195-B200.
[65] S.K. Cheah, O. Sicardy, M. Marinova, L. Guetaz, O. Lemaire, P. Gelin, A.A. Franco, J Electrochem Soc, 158 (2011) B1358-B1367.
[66] B.E. Hayden, Abstr Pap Am Chem S, 221 (2001) U358-U358.
[67] T.J. Schmidt, H.A. Gasteiger, R.J. Behm, J New Mat Electr Sys, 2 (1999) 27-32.
[68] J.P. MacDonald, B. Gualtieri, N. Runga, E. Teliz, C.F. Zinola, Int J Hydrogen Energ, 33 (2008) 7048-7061.

[69] I. Avila-Garcia, M. Plata-Torres, M.A. Dominguez-Crespo, C. Ramirez-Rodriguez, E.M. Arce-Estrada, J Alloy Compd, 434 (2007) 764-767.
[70] G. Stalnionis, L. Tamasauskaite-Tamasiunaite, V. Pautieniene, A. Sudavicius, Z. Jusys, J Solid State Electr, 8 (2004) 892-899.
[71] G. Stalnionis, L. Tamasauskaite-Tamasiunaite, V. Pautieniene, Z. Jusys, J Solid State Electr, 8 (2004) 900-907.
[72] W.P. Zhou, S. Axnanda, M.G. White, R.R. Adzic, J. Hrbek, J Phys Chem C, 115 (2011) 16467-16473.
[73] K. Taniya, H. Jinno, M. Kishida, Y. Ichihashi, S. Nishiyama, J Catal, 288 (2012) 84-91.
[74] B. Habibi, N. Delnavaz, Rsc Adv, 2 (2012) 1609-1617.
[75] Y. Wang, S.Q. Song, G. Andreadis, H. Liu, P. Tsiakaras, J Power Sources, 196 (2011) 4980-4986.
[76] N. Tsud, T. Skala, K. Veltruska, M. Skoda, K.C. Prince, V. Matolin, J Phys-Condens Mat, 23 (2011).
[77] S. Agnoli, G. Barcaro, A. Barolo, A. Fortunelli, M. Sambi, F. Sedona, M. Di Marino, T. Skala, G. Granozzi, J Phys Chem C, 115 (2011) 14264-14269.
[78] M.A. Gulmen, A. Sumer, A.E. Aksoylu, Surf Sci, 600 (2006) 4909-4921.
[79] M. Hoheisel, S. Speller, A. Atrei, U. Bardi, G. Rovida, Phys Rev B, 71 (2005).
[80] S. Axnanda, W.-P. Zhou, M.G. White, Phys Chem Chem Phys, 14 (2012) 10207-10214.
[81] M. Oezaslan, F. Hasche, P. Strasser, J Electrochem Soc, 159 (2012) B394-B405.
[82] H. Xin, A. Holewinski, S. Linic, ACS Catalysis, 2 (2011) 12-16.
[83] T. Cochell, A. Manthiram, Langmuir, 28 (2011) 1579-1587.
[84] I.E.L. Stephens, A.S. Bondarenko, U. Gronbjerg, J. Rossmeisl, I. Chorkendorff, Energy & Environmental Science, (2012).
[85] T.P. Johansson, PhD Thesis DTU, (2012).
[86] W. Du, K.E. Mackenzie, D.F. Milano, N.A. Deskins, D. Su, X. Teng, ACS Catalysis, (2012) 287-297.
[87] N.M. Marković, C.A. Lucas, V. Climent, V. Stamenković, P.N. Ross, Surf Sci, 465 (2000) 103-114.
[88] B. Álvarez, V. Climent, A. Rodes, J.M. Feliu, J Electroanal Chem, 497 (2001) 125-138.
[89] F. McBride, G.R. Darling, K. Pussi, C.A. Lucas, Y. Gründer, M. Darlington, A. Brownrigg, A. Hodgson, The Journal of Physical Chemistry C, 117 (2013) 4032-4039.
[90] V.R. Stamenkovic, B. Fowler, B.S. Mun, G. Wang, P.N. Ross, C.A. Lucas, N.M. Markovic, Science, 315 (2007) 493-497.
[91] T. Wadayama, N. Todoroki, Y. Yamada, T. Sugawara, K. Miyamoto, Y. Iijama, Electrochem Commun, 12 (2010) 1112-1115.
[92] N. Todoroki, R. Takahashi, Y. Iijima, Y. Yamada, T. Hayashi, T. Wadayama, Mater Trans, 54 (2013) 1735-1740.
[93] N. Todoroki, Y. Iijima, R. Takahashi, Y. Asakimori, T. Wadayama, J Electrochem Soc, 160 (2013) F591-F596.
[94] M.P. Hyman, J.W. Medlin, J Phys Chem C, 111 (2007) 17052-17060.
[95] T. Wadayama, H. Yoshida, K. Ogawa, N. Todoroki, Y. Yamada, K. Miyamoto, Y. Iijima, T. Sugawara, K. Arihara, S. Sugawara, K. Shinohara, J Phys Chem C, 115 (2011) 18589-18596.
[96] Y. Yamada, K. Miyamoto, T. Hayashi, Y. Iijima, N. Todoroki, T. Wadayama, Surf Sci, 607 (2013) 54-60.
[97] N.M. Markovic, T.J. Schmidt, V. Stamenkovic, P.N. Ross, Fuel Cells, 1 (2001) 105-116.
[98] J.C. Davies, B.E. Hayden, D.J. Pegg, Surf Sci, 467 (2000) 118-130.
[99] M. Krausa, W. Vielstich, J Electroanal Chem, 379 (1994) 307-314.
[100] H. von Schenck, E. Janin, O. Tjernberg, M. Svensson, M. Gothelid, Surf Sci, 526 (2003) 184-192.

[101] M. Nakamura, R. Imai, N. Otsuka, N. Hoshi, O. Sakata, The Journal of Physical Chemistry C, (2013).
[102] M. Batzill, D. Beck, B.E. Koel, Surf Sci, 558 (2004) 35-48.
[103] C. Panja, N.A. Saliba, B.E. Koel, J Phys Chem B, 105 (2001) 3786-3796.
[104] N.A. Saliba, D.E. Beck, C. Baur, B.E. Koel, Abstr Pap Am Chem S, 217 (1999) U599-U599.
[105] J. Haubrich, D. Loffreda, F. Delbecq, P. Sautet, Y. Jugnet, C. Becker, K. Wandelt, J Phys Chem C, 114 (2010) 1073-1084.
[106] J. Haubrich, D. Loffreda, F. Delbecq, P. Sautet, A. Krupski, C. Becker, K. Wandelt, The Journal of Physical Chemistry C, 113 (2009) 13947-13967.
[107] H. Zhao, B.E. Koel, Surf Sci, 572 (2004) 261-268.
[108] H. Zhao, B.E. Koel, Surf Sci, 573 (2004) 413-425.
[109] W. Gao, J.E. Mueller, Q. Jiang, T. Jacob, Angewandte Chemie International Edition, 51 (2012) 9448-9452.
[110] N.M. Marković, B.N. Grgur, P.N. Ross, The Journal of Physical Chemistry B, 101 (1997) 5405-5413.
[111] C. Gallis, B. Legrand, G. Tréglia, Surf Sci, 377–379 (1997) 1033-1037.
[112] B. Predel, Pt-Sn (Platinum-Tin), in: O. Madelung (Ed.) Ni-Np – Pt-Zr, vol. 5I, Springer Berlin Heidelberg, 1998, pp. 1-3.
[113] A. Atrei, U. Bardi, J.X. Wu, E. Zanazzi, G. Rovida, Surf Sci, 290 (1993) 286-294.
[114] M.T. Paffett, R.G. Windham, Surf Sci, 208 (1989) 34-54.
[115] A.N. Haner, P.N. Ross, U. Bardi, Catal Lett, 8 (1991) 1-7.
[116] M. Galeotti, A. Atrei, U. Bardi, G. Rovida, M. Torrini, Surf Sci, 313 (1994) 349-354.
[117] C. Creemers, S. Helfensteyn, Appl Surf Sci, 167 (2000) 216-229.
[118] M. Batzill, D.E. Reck, B.E. Koel, Surf Sci, 466 (2000) L821-L826.
[119] N.A. Saliba, Y.-L. Tsai, B.E. Koel, The Journal of Physical Chemistry B, 103 (1999) 1532-1541.
[120] M. Batzill, D.E. Beck, D. Jerdev, B.E. Koel, J Vac Sci Technol A, 19 (2001) 1953-1958.
[121] M. Batzill, D.E. Beck, B.E. Koel, Appl Phys Lett, 78 (2001) 2766-2768.
[122] M. Batzill, D.E. Beck, B.E. Koel, Phys Rev B, 64 (2001) 245402.
[123] H. Busse, M.R. Voss, D. Jerdev, B.E. Koel, M.T. Paffett, Surf Sci, 490 (2001) 133-143.
[124] A. Atrei, U. Bardi, G. Rovida, M. Torrini, M. Hoheisel, S. Speller, Surf Sci, 526 (2003) 193-200.
[125] M. Batzill, J. Kim, D.E. Beck, B.E. Koel, Phys Rev B, 69 (2004).
[126] M.R. Voss, H. Zhao, B.E. Koel, Surf Sci, 560 (2004) 235-245.
[127] M.T. Paffett, S.C. Gebhard, R.G. Windham, B.E. Koel, Surf Sci, 223 (1989) 449-464.
[128] S.H. Overbury, D.R. Mullins, M.T. Paffett, B.E. Koel, Surf Sci, 254 (1991) 45-57.
[129] C. Xu, B. E. Koel, Surf Sci, 310 (1994) 198-208.
[130] Š. Pick, Surf Sci, 436 (1999) 220-226.
[131] P.N. Ross, Journal of Vacuum Science & Technology A: Vacuum, Surfaces, and Films, 10 (1992) 2546.
[132] D.I. Jerdev, B.E. Koel, Surf Sci, 492 (2001) 106-114.
[133] M. Hoheisel, S. Speller, W. Heiland, A. Atrei, U. Bardi, G. Rovida, Phys Rev B, 66 (2002) 165416.
[134] W. Unger, D. Marton, Surf Sci, 218 (1989) L467-L475.
[135] J. Szanyi, S. Anderson, M.T. Paffett, J Catal, 149 (1994) 438-448.
[136] H. Gasteiger, N. Marković, P. Ross, Jr., Catal Lett, 36 (1996) 1-8.
[137] A.A. El-Shafei, M. Eiswirth, Surf Sci, 604 (2010) 862-867.
[138] E. Mostafa, A.-E.-A.A. Abd-El-Latif, R. Ilsley, G. Attard, H. Baltruschat, Phys Chem Chem Phys, 14 (2012) 16115-16129.

[139] Y. Jugnet, D. Loffreda, C. Dupont, F. Delbecq, E. Ehret, F.J. Cadete Santos Aires, B.S. Mun, F. Aksoy Akgul, Z. Liu, The Journal of Physical Chemistry Letters, 3 (2012) 3707-3714.
[140] E. Janin, H. von Schenck, S. Ringler, J. Weissenrieder, T. Åkermark, M. Göthelid, J Catal, 215 (2003) 245-253.
[141] C. Panja, E.C. Samano, N.A. Saliba, B.E. Koel, Surf Sci, 553 (2004) 39-49.
[142] C. Xu, B.E. Koel, Surf Sci, 304 (1994) 249-266.
[143] E. Janin, M. Björkqvist, T.M. Grehk, M. Göthelid, C.M. Pradier, U.O. Karlsson, A. Rosengren, Appl Surf Sci, 99 (1996) 371-378.
[144] Y.-L. Tsai, C. Xu, B.E. Koel, Surf Sci, 385 (1997) 37-59.
[145] H. Zhao, J. Kim, B.E. Koel, Surf Sci, 538 (2003) 147-159.
[146] S. Tillmann, G. Samjeske, K.A. Friedrich, H. Baltruschat, Electrochim Acta, 49 (2003) 73-83.
[147] M.A. Gülmen, A. Sümer, A.E. Aksoylu, Surf Sci, 600 (2006) 4909-4921.
[148] H. Zhao, B.E. Koel, J Catal, 234 (2005) 24-32.
[149] J.W. Peck, B.E. Koel, J Am Chem Soc, 118 (1996) 2708-2717.
[150] V. Stamenkovic, M. Arenz, B.B. Blizanac, P.N. Ross, N.M. Markovic, J New Mat Electr Sys, 7 (2004) 125-132.
[151] B.E. Hayden, M.E. Rendall, O. South, Journal of Molecular Catalysis A: Chemical, 228 (2005) 55-65.
[152] A.N. Haner, P.N. Ross, U. Bardi, Surf Sci, 249 (1991) 15-20.
[153] M.T. Paffett, A.D. Logan, R.J. Simonson, B.E. Koel, Surf Sci, 250 (1991) 123-138.
[154] C. Panja, B.E. Koel, Israel Journal of Chemistry, 38 (1998) 365-374.
[155] M. Hoheisel, J. Kuntze, S. Speller, A. Postnikov, W. Heiland, I. Spolveri, U. Bardi, Phys Rev B, 60 (1999) 2033-2039.
[156] Y. Li, B.E. Koel, Surf Sci, 330 (1995) 193-206.
[157] A.N. Haner, P.N. Ross, U. Bardi, Surf Sci, 249 (1991) 15-20.
[158] C. Panja, B.E. Koel, J Phys Chem A, 104 (2000) 2486-2497.
[159] C. Panja, N.A. Saliba, B.E. Koel, Catal Lett, 68 (2000) 175-180.
[160] E. Janin, H. von Schenck, S. Hellden, O. Tjernberg, U.O. Karlsson, M. Gothelid, Surf Sci, 515 (2002) 462-470.
[161] A. Sumer, M.A. Gulmen, A.E. Aksoylu, Surf Sci, 600 (2006) 2026-2039.

2 Experimental Techniques and Model Calculations

In this chapter, some basic principles of the experimental techniques used for the sample characterization during this PhD thesis will be introduced briefly, i.e. TPD, XPS, STM, and LEED. Certain basis theory about quantum mechanism calculation will also be presented. For more detailed information about both the experimental set-up and the rigorous interpretative principles the reader is redirected to textbooks about Surface Science and quantum calculations. Besides, the used experimental setups (TPD-Mass and UHV-STM) during the experiments will be displayed.

2.1 Ultra High Vacuum Chamber

2.1.1 X-ray Photoelectron Spectroscopy

The X-Ray Photoelectron Spectroscopy (XPS)[1-4] employs the photoelectric effect. Some photoelectrons will emit when a solid surface is exposed to an X-ray radiation. A simple schematic configuration for an XPS setup is presented as Figure 2-1(a), and it consists of an X-ray primary source, a sample holder and an electron analyzer.

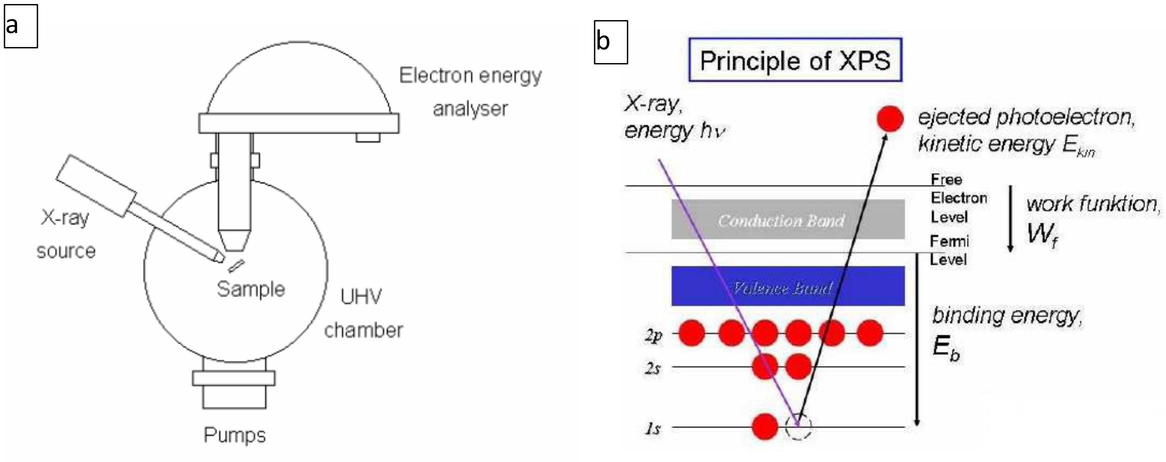

Figure 2-1(a) Schematic representation of an XPS instrument; (b) The photoemission process (a 1s photoelectron emission as the example).

When the X-rays photon flux, generated by the source (usually through electron bombardment of a metal anode, Mg or Al), is directed on the sample, a flux of photoelectrons will be generated both from the core and the valence shells (Figure 2-1 (b),). The photoelectrons emitted between the X-ray photons and the sample can have different interactions. Part of them can undergo an elastic diffusion, and their energy is released as heat or contributes the spectrum baseline during the diffusion. Some other part of photons can both be excited and emitted without any energy loss, giving the characteristic elastic peaks. The analyzer can record the kinetic energy associated to the photoelectrons, and give out an output spectrum where the signal intensity (counts per second) is reported as a function of the kinetic energy. The kinetic energy depends on the incident photons energy (primary radiation $E = h\nu$) and it can be transformed into a function with electron binding energy to the atom (BE) showing as the equation:

$$\boldsymbol{E_k = h\nu - BE - \phi} \qquad \text{Equation 2-1}$$

where ϕ is work-function of the analyzer. The BE is strongly dependent on the oxidation state of the analyzed element. So, an XPS spectrum can provide some important information about the electronic structure of a solid sample through the analysis of its output core and valence peaks (Figure 2-2), although it is more difficult to specify a photoelectron from an oxidized element with respect to its reduced counterpart.

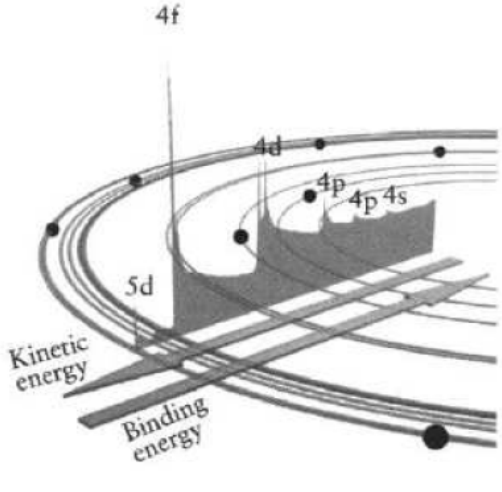

Figure 2-2 Example of an XPS spectrum.

Sampling depth as another important parameter in XPS depends on the emitted electrons kinetic energies. Moreover, the electrons kinetic energy affects an elastic attenuation length (Λ_e) which is directly related to the electron mean free path. The variation in the XPS signal intensity is expressed by the following:

$$I = I_0 \cdot exp\left(\frac{-z}{\Lambda_e sin\theta}\right) \qquad \text{Equation 2-2}$$

where $-z/sin\theta$ is the length covered by the electron. The relation between signal intensity and attenuation length can be demonstrated that the 65% signal intensity comes from a < Λ_e distance, the 85% comes from a < 2 Λ_e distance and the 95% comes from a < 3 Λ_e distance. So, this technique is considered "surface sensitive", only available to characterize a few nm sample thickness. Besides, if the angle between the sample surface and the analyzer (θ) is 90° (normal emission angle), the sampled thickness is 3 Λ_e. When the angle θ is reduced ($\theta < 90°$), the sampled thickness consequently becomes $3\Lambda_e sin\theta$, and the analysis turn more surface sensitive[5].

The conventional notation used in this thesis to indicate the XPS peaks refers to the quantum numbers related to the orbital where the photoelectron comes from. It is always express as nl_j, where n means the principal quantum number representing the orbital energy level and l indicates the azimuthal quantum number representing the orbital geometry. When $l>0$, the XPS peaks display generally doublets due to the interaction of the magnetic moment (m) associated to the angular one with the spin magnetic moment (m_s) associated to the electron. And the sum vector of these two creates a vector (j), expressed as a subscript in the notation, whose magnitude is given by $j = l + s$. Therefore a d peak can originate 3 values of j: 3/2 (which originates from $l - s$) and 5/2 (which originates from $l + s$). The peak distribution attributed from it will be a doublet, whose components will be separated by an energy difference corresponding to the spin-orbit coupling and an intensity ratio given by ($2j + 1$).

In period of my finishing PhD project, some work were finished at the Elettra synchrotron facility, in Basovizza, Trieste. A precise photon wavelength when using synchrotron radiation[1, 6, 7] set by mean of monochromators can be utilized during High Resolution (HR)-XPS experiments. Since the selected radiation derive from a storage ring where electrons are accelerated in a magnetic field up to very high energy (2.0 Gev), the photon fluxes are extremely high compared with the one produced by a common X-Ray source. Therefore, the intense and tunable photon energy can provide a maximization of the photoionization cross sections of the elements that are useful for the analysis. Meanwhile, it is also possible to minimize some contributions coming, for example, from the bulk substrates, basing on the photoionization cross sections Cooper's minimum energy position. The latter procedure is particularly helpful for the valence band studies as the presence of a bulk signal can affect the overall spectrum appearance.

2.1.2 Scanning Tunneling Microscope [8]

Scanning Tunneling Microscopy (STM) is a powerful technique for imaging surfaces at an atomic level. This technique is based on quantum tunneling effect: a conductive tip is brought close to the sample surface (ca. 1 nm) and a voltage difference (called Bias) is applied between the two, allowing electrons to go through the vacuum.

The measured electron current (tunneling current) is related with the bias, the tip position and the local density of states (LDOS) of the sample. The tunneling current as a quantum mechanical effect has two major properties for STM: it flows between two electrodes and even through a thin insulator or a vacuum gap, and it decays on the length scale of one atomic radius. So, it is possible to display a surface image plot according to the measured current as a function of the tip scan position. When the tip is close to the sample and its movements in the three dimensions are controlled by piezoelectric devices, the device can maintain a tip-sample separation that is typically in equilibrium between attractive and repulsive interactions. If the tip scans the sample (in the x-y planes), the changes in the surface morphology and LDOS cause changes in the current that can be mapped in images. There are two main way to operate with STM: constant height mode (mapping the above mentioned changes in the tunneling current) and constant current mode(mapping the tip height (z) with a constant current. Then the z position can be calibrated by applying a voltage to the piezoelectric height control mechanism. In the latter operating mode variations in the images contrast are due to variations in the sample charge density.

As the above description, the basic physical principle of STM is the interaction between the scanning tip and the sample. If this interaction has a near field character, it is possible to overcome the resolution limits of far-fields techniques like microscopies (optical and SEM), which has disadvantage of limitation in the order of half a wavelength of the photons or the electrons. However, the resolution in STM is just controlled by the geometrical shape of the tip. The lateral resolution is decided by the vertical amplitude of the structures on the surface. The probing tip is always a cone with an opening angle and a finite radius at the apex. Hence, images of the surface steps with walls steeper than the tip opening angle will be distorted due to the convolution of the tip shape with the surface structure. All the holes with smaller dimension than the tip radius will not be imaged at all or with a reduced corrugation, as it is possible to observe in Figure 2-6. On atomically flat surfaces or molecular layers the resolution is determined by the atomic structure of the tip apex.

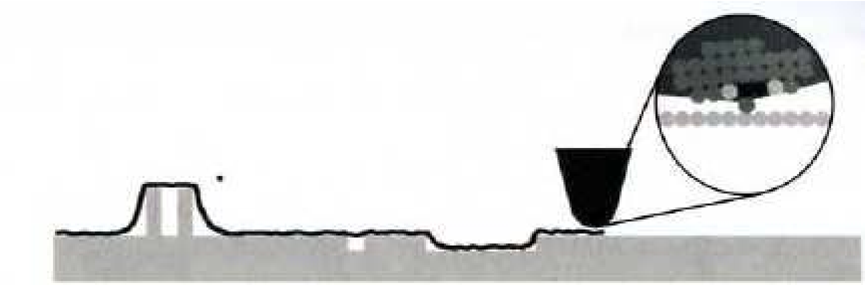

Figure 2-3 Resulution limits in a conventional STM instrument. Images of step walls and holes are distorted when their size is comparable to that of the tip apex

The most powerful near-field interaction is the tunneling current across a vacuum gap for two main reasons:

- the decay length is less than an atomic diameter
- there are no other electrical currents flowing through the vacuum.

2.1.3 Low Energy Electron Diffraction

The Low Energy Electron Diffraction (LEED) is based on the oscillation behavior of a primary electron beam at low energy (20-500 eV), which corresponds wavelengths variation from 0.5 to 2.0 Å. The electrons are diffracted and an image of diffraction spots matching the reciprocal lattice ones can be obtained if the beam interacts with a crystal lattice with comparable inter-atomic distances. Then, we can deduce the real lattice and surface structure according to the obtained bright spots. The electrons mean escape depth values are low, usually less than 10 Å, so that electrons are very surface sensitive and can be used for surface analysis of the surface atoms layers. A usual schematic experimental setup is displayed in Figure 2-4 (a)). In the device, the sample is illuminated with an electron beam, produced from electron gun at the back screen side. The electrons are then accelerated up to the set energies through a potential gap and collide on the sample.

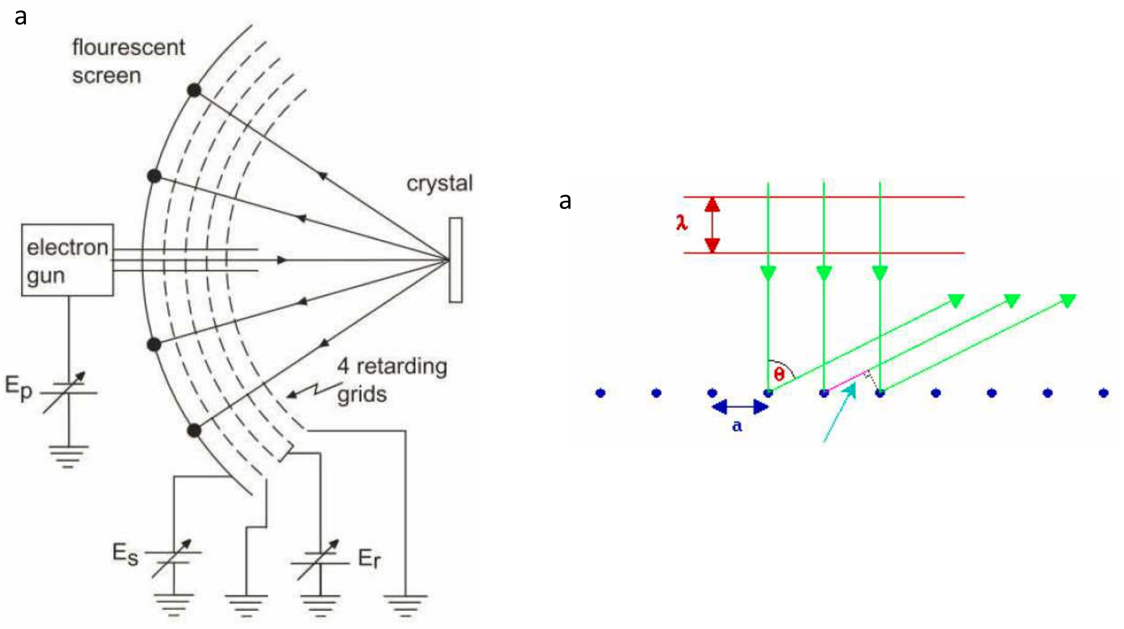

Figure 2-4 Example of a rear-view LEED configuration; (b) Schematic representation of the diffraction process from atoms separated by a periodic distance

The diffracted electrons emitted back in precise directions (with respect to the primary beam), collide with a suppressor made by a series of grids kept at a variable potential, in order to select their energy. The selected electrons emerge from the last grid, and then the diffraction spots are revealed from hemispheric fluorescent screen where the electrons hit finally.

The diffraction spots are typical as a function of the sample crystal lattice, are also used to judge surface reconstruction. The surface indicates homogeneous ordered and large if the obtained spots are sharp, intense and well defined (with respect to the screen background). When a disordered lattice is observed, the diffraction electrons from many directions can be generated and then a high background is observed. The diffraction spots correspond to the positive interference of the waves. In Figure 2-4 (b), a sample is proposed, where an electron beam with λ wavelength colliding with a mono-dimensional chain of atoms separated by a distance (a) is reported. The positive interference condition is given by the Bragg's law: where $n\lambda$ is an entire number of waves (n is the diffraction order) and $a\sin\theta$ is the inter-atomic distance projection along the propagation direction. The first diffraction order is then obtained when $\sin\theta = \lambda/a$. Hence, if the value of θ is known, the inter-atomic distance a can be obtained easily. When the sample is put at the center of the LEED screen, θ can be measured in this simplest way. And then the distance between the zero order spot (covered by the electron gun) and the first diffraction order a can be easily measured. Therefore, supposing the distance between the screen and the sample (R) and the one between the zero and first order diffraction spots (a^*) are known, the following relation can be obtained: $\sin\theta = a^*/R$, thus allowing us the calculation the a value:

$$a = \frac{R\lambda}{a^*} \qquad \text{Equation 2-3}$$

2.1.4 Temperature Programmed Desorption

The Temperature Programmed Desorption (TPD) [9] plays an important method for the study and determination of thermodynamic and kinetic parameters about the desorption processes. Commonly, the sample is heated following a programed temperature ramp ($\beta(\mathrm{t}) = dT/dt$) where the temperature (T) varies linearly with the time. The partial pressures corresponding to the atoms or molecules desorbed from the sample surface are detected by a Quadrupole Mass Spectrometer (QMS)[10]. So the final report of the experiment provides spectra including the partial pressures intensities as a function of the temperature. The experimental method used in this thesis for all the TPD experiments is always as the following:

a. Sample exposing to a precise amount (expressed in Langmuirs [L]) of a probe molecule/s (usually CO or methanol) at room temperature (RT) or low temperature (LT)

b. Sample heating (a linear temperature ramp by 1 or 2 K/s) up to a set temperature while the QMS monitor the *probe* molecule/s partial pressure intensities

c. Sample cooling-down after the set temperature is reached.

The adsorption process takes place when the surface temperature is enough to disorder the interaction energy between an adsorbate (probe molecule) in the gas phase and the surface. According to the strength of such interaction, both physisorption (typically Van der Waals interactions, with a $\Delta H_{ads} < 50$kJ/mol) or chemisorption (when the interaction strength is comparable to a chemical bond and $\Delta H_{ads} > 50$ kJ/mol) can be observed. The former, being a low energy interaction, is favored by low temperatures and is non-specific (each kind of molecule can be adsorbed under appropriate experimental conditions). The latter leading to the formation of a chemical bond is suitable for a specific orientation of the molecules. Moreover, some molecular can be dissociated due to the chemisorption interaction which can weaken the intra-molecular bonds[10]. The kinetic aspects regarding the adsorption/desorption processes are well described by the Langmuir isotherm, that is a function with the surface coverage to the gas pressure on the surface. The main assumptions to obtain this equation are the following:

a. The adsorption process is localized;
b. The sample surface is saturated so that the degree of coverage is θ= 1 ML when all the active sites are occupied;
c. The interactions between the adsorbed molecules are negligible.

It is then able to obtain the rate (*r*) both for the adsorption and the desorption processes:

$$r_{ad} = A_n \cdot p(1 - \theta)^n \qquad \text{Equation 2-4}$$

$$r_{des} = B_n \cdot \theta^n \qquad (A_n, B_n = \text{cost., n=1,2 }) \qquad \text{Equation 2-5}$$

When the equilibrium is reached: $r_{ad} = r_{des}$, and then:

$$A_n \cdot p(1 - \theta)^n = B_n \cdot \theta^n \qquad \text{Equation 2-6}$$

$$\theta = \frac{(b_n P)^{1/n}}{1+(b_n P)^{1/n}} \qquad (b_n = A_n/B_n = \text{cost., n=1,2 }) \qquad \text{Equation 2-7}$$

For *n* = 1, the adsorption/desorption kinetic is first order. For *n* = 2, the kinetic is second order and so on.

The adsorption/desorption processes according to the microscopic reversibility principle states that both the processes can be described by the same kinetic equations. Hence, the reaction rate for a *n* order process can be written as:

$$r_{des} = -\frac{d\theta}{dt} = k_n \cdot \theta^n \qquad \text{Equation 2-8}$$

where *k* is the rate constant that can be described with an Arrhenius equation:

$$k_n = \mathrm{v_n}(\theta) \cdot \exp\left(-\frac{\Delta E_{des}(\theta)}{RT}\right) \qquad \text{Equation 2-9}$$

Combining the two equations, it is possible to obtain the Polanyi-Wigner equation:

$$r_{des} = -\frac{d\theta}{dt} = \mathrm{v_n}(\theta) \cdot \exp\left(-\frac{\Delta E_{des}(\theta)}{RT}\right) \cdot \theta^n \qquad \text{Equation 2-10}$$

where $\mathrm{v_n}(\theta)$ is a pre-exponential frequency factor, θ is the degree of coverage, *n* is the kinetic order of the process (in this case the desorption) and $\Delta E_{des}(\theta)$ is the activation energy for the same process. Application of the Polanyi-Wigner equation to our experimental technique (TPD with *dt* =(1/β) ·*dt* causes the followed equation:

$$-\frac{d\theta}{dt} = \frac{1}{\beta}\nu_{\mathrm{n}}(\theta) \cdot \exp\left(-\frac{\Delta E_{des}(\theta)}{RT}\right) \cdot \theta^{n} \qquad \text{Equation 2-11}$$

This last equation indicates that:

_ the desorption temperature (T) depends on E_{des}, β, θ_n;

_ the desorption peaks shape depends on v_n, β, n;

_ the peaks area depends on θ_n.

If a sequence of desorption spectra is recorded at a constant coverage (θ_n) (both v_n and ΔE_{des} become independent from it) and at different heating rate (β), it is possible to obtain the desorption temperature corresponding to the peak maximum for each β. Then, we can get a plot reporting the $ln\left(\frac{T_{max}^2}{\beta}\right) vs \frac{1}{T_{max}}$ allowing us to calculate the ΔE_{des} value. The E_{dep} can also be calculated from the desorption temperature, which was proposed by Redhead.P.A[9]. The equation can be showed as followed equation if n=1.

$$\frac{E_{dep}}{RT_p} = ln\frac{\nu_1 T_p}{\beta} - 3.64 \qquad \text{Equation 2-12}$$

2.1.5 Evaporation of metals[11]

Physical Vapor Deposition (PVD) processes (often just called thin film processes) are atomistic deposition processes in which material is vaporized from a solid or liquid source in the form of atoms or molecules, transported in the form of a vapor through a vacuum or low pressure gaseous (or plasma) environment to the substrate where it condenses. Typically, PVD processes are used to deposit films with thicknesses in the range of a few nanometers to thousands of nanometers; however, they can also be used to form multilayer coatings, graded composition deposits, very thick deposits and freestanding structures. The substrates can range in size from very small to very large such as the glass panels used for architectural glass. The substrates can range in shape from flat to complex geometries such as watchbands and tool bits.

Typical PVD deposition rates are 10–100Å (1–10 nanometers) per second. PVD processes can be used to deposit films of elements and alloys as well as compounds using reactive deposition processes. In reactive deposition processes, compounds are formed by the reaction of depositing material with the ambient gas environment such as O_2 (e.g. SnO_2) or with a co-depositing material (e.g. titanium carbide, TiC). Quasi-reactive deposition is the deposition of films of a compound material from a compound source where loss of the more volatile species or less reactive species during the transport and condensation process, is compensated for by having a partial pressure of reactive gas in the deposition environment. For example, the quasi-reactive sputter deposition of ITO (indium-tin-oxide) from an ITO sputtering target using a partial pressure of oxygen in the plasma. The main categories of PVD processing are vacuum evaporation, sputter deposition, and ion plating as depicted in Figure 2-5. During my PhD research, vacuum evaporation is the only way to deposit the metal on the sample substrate.

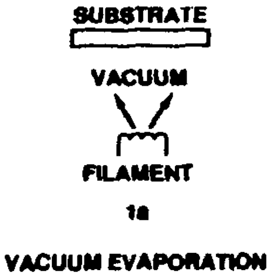

Figure 2-5 PVD processing techniques: vacuum evaporation

In this thesis, the all the surface were prepared with the procedure showing in Figure 2-6.

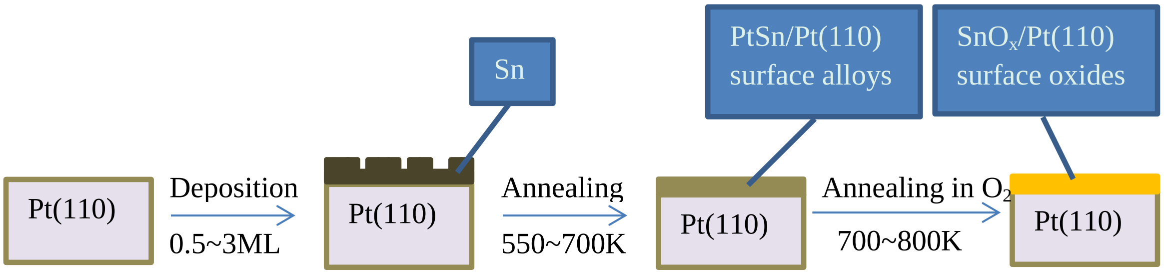

Figure 2-6 The procedure to prepare surface alloys and surface oxides

2.2 Density Function Calculations

2.2.1 DFT theories[12]

Density functional theory (DFT) is a quantum mechanical modeling method used in physics and chemistry to investigate the electronic structure of atoms, molecules, and the condensed phases. DFT has been attracted by the scientist since the 1970s, especially in the field of solid state physics [13, 14].

The aim of all quantum chemical approaches is the solution of the time-independent, non-relativistic Schrödinger equation[13]

$$\hat{\mathrm{H}}\Psi_i(\vec{x}_1, \vec{x}_2, \cdots \vec{x}_N, \vec{R}_1, \vec{R}_2, \cdots \vec{R}_M) = \mathrm{E}_i\Psi_i(\vec{x}_1, \vec{x}_2, \cdots \vec{x}_N, \vec{R}_1, \vec{R}_2, \cdots \vec{R}_M) \qquad \text{Equation 2-13}$$

where $\hat{\mathrm{H}}$ is the Hamilton operator for a molecular system consisting of M nuclei and N electrons in the absence of magnetic or electric fields. E_i corresponds to the energy eigenvalue of the Schrödinger equation and Ψ_i is the wave function. $\hat{\mathrm{H}}$ is a differential operator representing the total energy:

$$\hat{\mathrm{H}} = \mathrm{T_{el}} + \mathrm{T_{nu}} + \mathrm{V_{nu-nu}} + \mathrm{V_{el-el}} + \mathrm{V_{nu-el}} \qquad \text{Equation 2-14}$$

Where T_{el} is the kinetic energy of electrons; T_{nu} the kinetic energy of nuclei; V_{nu-nu} is interactions between nuclei, V_{el-el} is the interactions between electrons, and V_{nu-el} is the interactions between electrons and nuclei.

In reality, only a few systems such as the hydrogen atom or H_2^+ can be solved analytically, as these system have only one electron which excludes the interaction between electron and electron. All other systems require at least two approximations. One is the Born-Oppenheimer approximation. As the difference between electron and nucleus is very large, even a proton is about 1800 times heavier than electron, hence the nuclei move much slower than the electrons. So, it is a good approximation to consider the electrons as moving in the field of fixed nuclei[13]. This approximation allows to separate the electronic and nucleus parts of the Schrödinger equation.

$$\Psi_{tot} = \Psi_{el}\Psi_{nu} \qquad \text{Equation 2-15}$$

Where Ψ_{tot} is the total wave functional, Ψ_{el} is the wave functional of electrons and Ψ_{nu} is the wave functional of nuclei. So, the contributions to the total potential energy surface can be splitted up as follows:.

$$\mathrm{E}_{tot} = \mathrm{E}_{el} + \mathrm{E}_{nu} \qquad \text{Equation 2-16}$$

Where E_{tot} is the total energy, E_{el} is the energy of electrons and E_{nu} is the energy of nuclei. So, potential energy surface is obtained.

One of the first practical implementations to solve the electronic Schrödinger equation for multi-electron systems within the independent particle and Born-Oppenheimer approximations are the Hartree-Fock equations[15]. The independent particle approximation[13] assumes, that the single electrons moves in the field of all other electrons. So instead of considering all surrounding electrons independently only their mean field is used. Then the system state can be considered as the product of all the single particle state in the system.

$$\left\{-\frac{\hbar^2}{2m}\nabla^2+\left(-\sum_i\frac{\mathrm{Z}_i e^2}{|\boldsymbol{r}-\boldsymbol{R}_i|}\right)+\sum_j\int d^3\boldsymbol{r}'\frac{e^2}{|\boldsymbol{r}-\boldsymbol{r}'|}\left|\Psi_j(\boldsymbol{r}')\right|^2\right\}\Psi_i(\boldsymbol{r})$$
$$-\sum_j\int d^3\boldsymbol{r}'\frac{e^2}{|\boldsymbol{r}-\boldsymbol{r}'|}\Psi_j^*(r')\Psi_i(\boldsymbol{r}')\Psi_j(r)\delta_{\sigma_i\sigma_j}=\mathrm{E_i}\Psi_i(\boldsymbol{r})$$

Equation 2-17

Where

$-\frac{\hbar^2}{2m}\nabla^2$ is $\mathrm{T_{el}}$;

$\left(-\sum_i\frac{\mathrm{Z}_i e^2}{|r-R_i|}\right)$ is $\nu_{\mathrm{ext}}(\mathrm{r})$ which equals to $\nu_{\mathrm{nu-el}}(\mathrm{r})$;

$\sum_j\int d^3r'\frac{e^2}{|\boldsymbol{r}-\boldsymbol{r}'|}\left|\Psi_j(r')\right|^2$ is $\nu_{\mathrm{Hartree}}(\mathrm{r})$ which equals to $\nu_{\mathrm{el-el}}(\mathrm{r})$;

$\sum_j\int d^3r'\frac{e^2}{|\boldsymbol{r}-\boldsymbol{r}'|}\Psi_j^*(r')\Psi_i(\boldsymbol{r}')\Psi_j(r)\delta_{\sigma_i\sigma_j}$ is $\mathrm{E_x}$ which is the .

Having solved all 1-electron Hartree-Fock equations the total energy of the system can finally be obtained from summing up all the single electron energies and adding the constant interaction between nuclei.[16, 17] A complementary way to solve the electronic Schrödinger equation is Density Functional Theory (DFT). In pure DFT, which is based on the Hohenberg-Kohn theorem [18]. The HK theorem says for a given electron density the external potential is unique. As a result the electron density may be used.

$$\mathrm{N}(\mathbf{r})\longrightarrow\nu_{\mathrm{ext}}(\mathbf{r})+\mathrm{const} \qquad \text{Equation 2-18}$$

$$\mathrm{N}=\int n(\boldsymbol{r})d^3\boldsymbol{r} \qquad \text{Equation 2-19}$$

Where, N is the times of the probability for one particular electron[13].

Hence, Kohn-Sham (KS)[18] , a more practical formulation, was developed to solve the trouble in computational chemistry due to the limitation of DFT. The new DFT formulation, inspired by Hartree-Fock theory, replaces the electron density n(**r**) in pure DFT by a wave function.

$$n(\boldsymbol{r})=\sum_{i=1}^{N}|\Psi_i(\boldsymbol{r})|^2 \qquad \text{Equation 2-20}$$

$$\left\{-\frac{\hbar}{2m}\nabla^2+\nu_{\mathrm{ext}}(\mathbf{r})+\nu_{Hartree}(\boldsymbol{r})+\nu_{\mathrm{xc}}(\mathbf{r})\right\}\Psi_i(\boldsymbol{r})=E_i\Psi_i(\boldsymbol{r}) \qquad \text{Equation 2-21}$$

Where $-\frac{\hbar}{2m}\nabla^2$ is $\mathrm{T_{elec}}$, and $\nu_{\mathrm{ext}}(\mathbf{r})+\nu_{Hartree}(\boldsymbol{r})+\nu_{\mathrm{xc}}(\mathrm{r})$ is $\nu_{\mathrm{eff}}(\mathbf{r})$.

The exchange can be known exactly from Hartree-Fock theory, but the exact value from correlation part is unknown. Over the years different levels of approximations were developed most notably GGAs[13, 18, 19]. GGAs rely on approximated exchange and correlation parts for cancellation of errors. Even introduction of GGA functions, there are also some problems with DFT exist, i.e. van-der-Waals[14], near-degenerate electronic structures which can be found in TM oxides[20, 21], artificial delocalization of charges due to interaction of electron with itself[18].

2.2.1 Computational method

All closed-shell density functional theory (DFT) calculations were performed using GPAW[22, 23] (version: 0.9.0.8965) code within the ASE (version: 3.7.1.3184) [24] environment at the generalized gradient approximation (GGA) level of theory employing the RPBE[19] functional. The core electrons were approximated by projector augmented wave functions (PAW) [25] as implemented into GPAW (version: 0.8.7929). A finite difference grid basis set with a grid spacing of 0.15 Å was used for the valence electrons. Depending on the surface reconstruction k-point sets containing 5×5×1 for p(3×1), 9×3×1 for p(6×1), 5×5×1 for Pt(110), 5×5×5 for the required bulk structures Sn_8, 9×9×9 for Pt_3Sn and 5×5×9 for $Pt_{15}Sn$ k-point sets were employed. The geometries were relaxed using a BFGS algorithm as implemented into ASE (version: 3.7.1.3184). Convergence of the electronic structure was assumed for energy differences below 0.0005 eV and convergence of the geometry for forces below 0.05 eV/Å. STM images of the fully converged surfaces for different potentials were simulated using ASE [26-29].

Employing these setups a lattice constants of 4.01 Å for Pt_4, 4.10 Å for Pt_3Sn and 6.74 Å for Sn_8 (α-Sn_8) were obtained. These results are in agreement with experiment [30]. All surfaces were modeled employing a 5 monolayer (ML) slab using the relaxed Pt_4 system as a precursor in order to account for the pure Pt bulk which enforces a Pt_4 lattice constant on the surface monolayers. The lowest ML was kept constant and the slabs were divided by a vacuum of at least 8 Å in order to avoid interactions between the slabs. In order to identify the most stable configuration a number of different models for the p(3×1) and p(6×1) reconstructions, differing in the amount and the position of Pt atoms substituted by Sn, were considered.

In the above equations, m can be 3 or 6 to calculate the formation energies of p(3×1) and p(6×1) respectively, and y is the number of replaced atoms to form the reconstructed surface alloys. $Pt(110)_{rec}$ is the reconstructed surface with pure Pt slab and its energy is $E_{Pt(110)_{rec}}$. $p(m\times 1)PtSn/Pt_xSn(110)$ is reconstructed surface which can be p(3×1) or p(6×1) surface, and their energies are described as $E_{p(m\times 1)PtSn/Pt_xSn(110)}$. $Pt_{4\,bulk}$ is bulk Pt unit with energy $E_{Pt_{4\,bulk}}$ and $Sn_{8\,bulk}$ is bulk α-Sn_8 unite with energy $E_{Sn_{8\,bulk}}$. The relative energies can be calculated by assuming a reaction where a surface slab Pt atom is replace by a Sn atom from a Sn source such as Pt_3Sn

$$Pt(110)_{rec} + y \times {}^{1}\!/_{8}\ Sn_{8\,bulk} \ \rightarrow\ p(m\times 1)PtSn/Pt_xSn(110) +\ y \times {}^{1}\!/_{4}\ Pt_{4\,bulk}$$

Equation 2-22

The energy of formation for the different model slabs become then

$$E_F = E_{p(m\times 1)PtSn/Pt_xSn(110)}\ +\ y\cdot(\tfrac{1}{4}E_{Pt_{4\,bulk}} - \tfrac{1}{8}\ E_{Sn_{8\,bulk}}) - E_{Pt(110)_{rec}}$$

Equation 2-23

Where m can be 3 or 6 to calculate the formation energies of p(3×1) and p(6×1) respectively, and y is the number of replaced atoms to form the reconstructed surface alloys. $Pt(110)_{rec}$ is the reconstructed surface with pure Pt slab and its energy is $E_{Pt(110)_{rec}}$. $p(m\times 1)PtSn/Pt_xSn(110)$ is reconstructed surface which can be p(3×1) or p(6×1) surface, and their energies are described as $E_{p(m\times 1)PtSn/Pt_xSn(110)}$. $Pt_{4\,bulk}$ is bulk Pt unit with energy $E_{Pt_{4\,bulk}}$ and $Sn_{8\,bulk}$ is bulk α-Sn_8 unite with energy $E_{Sn_{8\,bulk}}$. Employing pure Pt_4 and α-Sn_8 (modification) as references would results would prefer unphysical high Sn concentrations [31]. In order to correct for this error a more physical reference system is required. In the present study Pt_3Sn and a more diluted $Pt_{15}Sn$ were considered as Sn sources. The reference energy can in this case be obtained by assuming the following chemical reaction

$$Pt_{4bulk} + {}^{1}\!/_{8}\ Sn_{8bulk}\ \rightarrow\ Pt_3Sn_{\ bulk} +\ {}^{1}\!/_{4}\ Pt_{4bulk}$$

$$Pt_{16bulk} + {}^{1}\!/_{8}\ Sn_{8bulk}\ \rightarrow\ Pt_{15}Sn_{\ bulk} +\ {}^{1}\!/_{4}\ Pt_{4bulk}$$

$$\boldsymbol{\Delta E_{Pt_xSn}\ =\ E_{\ Pt_xSn_{\ bulk}} +\ {}^{1}\!/_{4}\ E_{\ Pt_{4\,bulk}} -\ E_{\ Pt_{4\,bulk}} -\ {}^{1}\!/_{8}\,E_{\ Sn_{8\,bulk}}}$$

Equation 2-24

The reference energy becomes then

$${}^{1}\!/_{8}\,E_{\ Sn_{8\,bulk}} =\ E_{\ Pt_xSn_{\ bulk}} +\ {}^{1}\!/_{4}\ E_{\ Pt_{4\,bulk}} -\ E_{\ Pt_{4\,bulk}} - \Delta E$$

$$= \boldsymbol{E_{\ Pt_xSn_{\ bulk}} - {}^{3}\!/_{4}\,E_{\ Pt_{4\,bulk}}\ - \Delta E_{Pt_xSn}}$$

Equation 2-25

Where x can be 3 and 15 responding to Pt_3Sn and $Pt_{15}Sn$ respectively.

Then, $\Delta E_{Pt_3Sn} = -1.43eV$ and $\Delta E_{Pt_{15}Sn} = -1.18eV$ were obtained. In this paper, we defined the negative value as energy emitted from the system.

By replacing $E_{reference}$ in Equation 2-25 by Equation 2-27 the formation energy becomes

$$E_F = E_{p(m\times1)PtSn/Pt_xSn(110)} + y \times {}^{1}\!/_{4}\, E_{Pt_4\,bulk} - y\cdot\left(E_{Pt_3Sn\,bulk} - {}^{3}\!/_{4}\, E_{Pt_4\,bulk} - \Delta E_{Pt_xSn}\right) - E_{Pt(110)_{rec}}$$

$$= E_{p(m\times1)PtSn/Pt_xSn(110)} - E_{Pt(110)_{rec}} + y\cdot\left(E_{Pt_4\,bulk} - E_{Pt_3Sn\,bulk} + \Delta E_{Pt_xSn}\right)$$

Equation 2-26

Formation energies for both a Pt_3Sn and a $Pt_{15}Sn$ reference system were calculated. While indeed quantitative differences are found between both references, the predictions arrived at are not affected. In what follows results only using the $Pt_{15}Sn$ reference system are reported.

A second potential source of errors is differences in the amount of tin atoms at the backside surface of the slab. In order to correct for this model inherent source of errors, the correction factor for placing a bulk tin atom at the backside surface is calculated. This correction is arrived at by calculating the energy difference for a Sn atom in a 5 ML Pt(110) slab in the center of the slab and at the surface. This results in a correction of 0.97eV per surface Sn atom at the backside surface of the slab that was added. So the Equation 2-28 can be corrected into Equation 2-29 in which z is the atoms at back side.

$$E_F = E_{p(m\times1)PtSn/Pt_xSn(110)} - E_{Pt(110)_{rec}} + y\cdot\left(E_{Pt_4\,bulk} - E_{Pt_3Sn\,bulk} + \Delta E_{Pt_xSn}\right) + 0.97\cdot z$$

Equation 2-27

Adsorption energy is calculated with the deviation between the energetic sum of CO (E_{CO}) & surface (E_M) and the systematic energy of the surface adsorbed with CO ($E_{CO\text{-}M}$)[20].

$$E_{ad} = E_{CO-M} - (E_{CO} - E_M)$$

Equation 2-28

2.3 STM simulations

STM can observe details of the electronic properties of sample surface as it has a sharp tip which can approach to surface very close in real space. Then the electron of the tip can interact with the electron of atoms or molecules of the surface. During the STM measurements, the signals by atomic structure and electronic structure can be recorded together through the tip. So, it is very important to understand the corresponding effects from electronic interaction or morphology, especially for the atomic resolved STM images. Due to the difficulty of separating the current from the electronic interactions and surface structures, the collaboration between experiment and theory is indispensable for the interpretation of experimental results. Then, an accurate STM simulation can show the insight on the origins of observed image contrast, and avoid some effect by the STM devices, STM tip and so on. [27].

In the simplest case, the tunneling current can be considered as the electrons over the vacuum between STM tip and sample, so the value is proportional to the probability of finding the surface electron in the tip apex region [27, 29]. If the electron–electron interaction can be disregarded, and a constant value U between tip and sample is applied, the electron can be described by a single particle Schrödinger equation:

$$-\frac{\hbar^2}{2m}\frac{d^2}{dz^2}\psi(z) + U\psi(z) = E\psi(z) \tag*{Equation 2-29}$$

In which, z corresponds to the distance between the electrons of sample surface and tip. Then, the decayed surface state can be described as the Equation 2-41 when the potential is in the classically forbidden region ($E < U$).

$$\phi(z) = \phi(z)e^{-\kappa z} \tag*{Equation 2-30}$$

$\kappa = \sqrt{2m(U-E)}/\hbar$ is the decay constant of the electron state. In the Tersoff– Hamann model, an atomic s orbital assuming is employed as the electronic structure of the tip. When the applied bias is very small, the electronic properties of tip and sample are not affected. Then, the tunneling current can be evaluated from the Tersoff–Hamann formula[28, 29]:

$$I(z) \propto \sum_{E_{s_n} > E_F - eV_{bias}}^{E_{s_n} < E_F} \left|\psi\left(z, E_{s_n}\right)\right|^2 \tag*{Equation 2-31}$$

where E_F is the Fermi level of the sample surface states. In practice, the obtained tunneling current map according to the TH model is simply the Local Density of States (LDOS) of the sample at Fermi level [27]. Hence, Tersoff-Hamann method can be very simple, and is adopted by most existing DFT codes.

2.4 Instruments

The instruments used during my PhD thesis are showed in Figure 2-7. All the TPD tests were finished in TPD setup showing as Figure 2-7(a). Some of STM images were completed in UHV-TPD displayed as Figure 2-7(b).

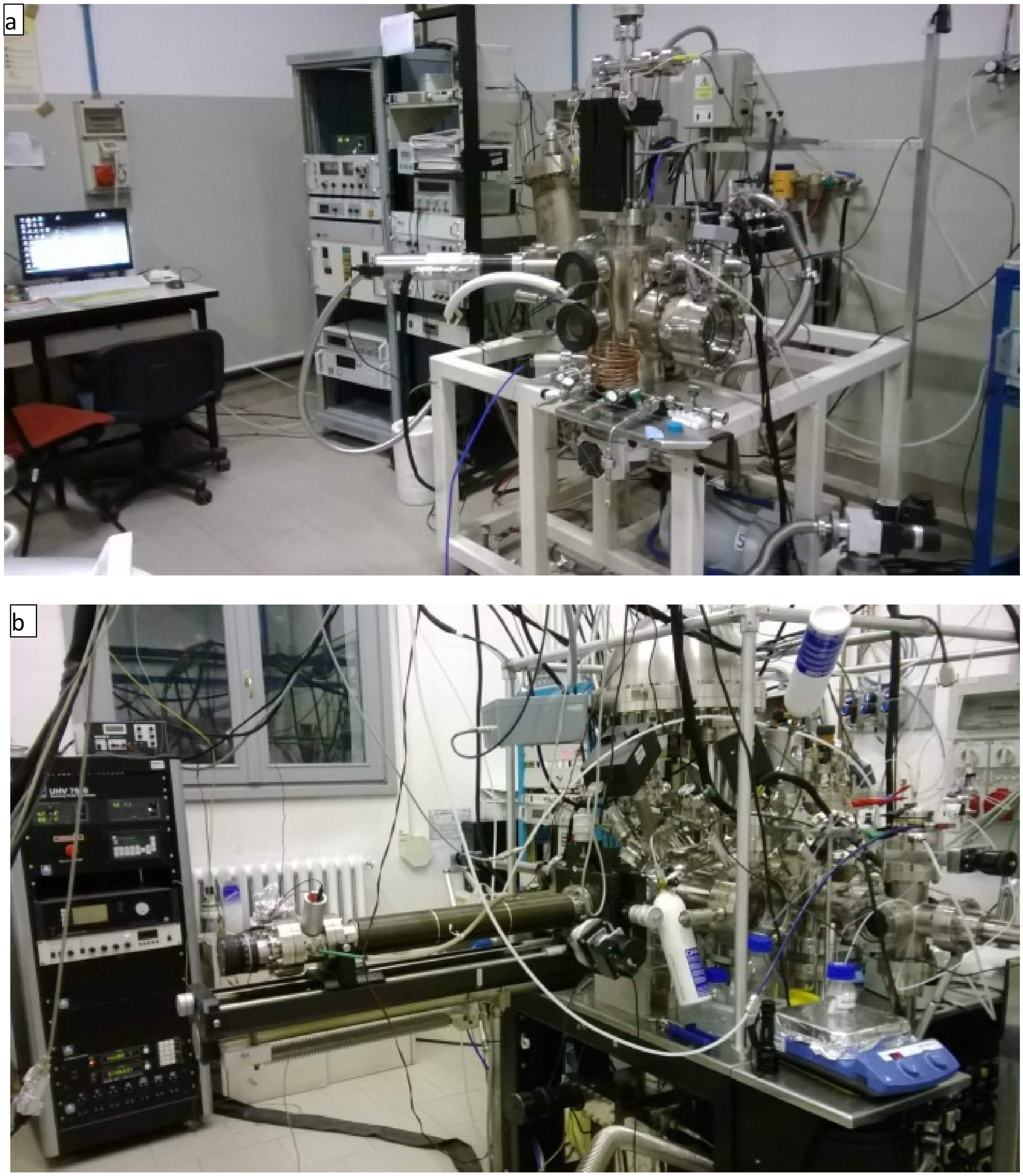

Figure 2-7 *(a) The TPD UHV chamber setup; (b) The UHV-STM chamber setup.*

References

[1] S. Doniach, M. Sunjic, Journal of Physics C: Solid State Physics, 3 (1970) 285.
[2] J.F. Watts, J. Wolstenholme, Electron Spectroscopy: Some Basic Concepts, in: An Introduction to Surface Analysis by XPS and AES, John Wiley & Sons, Ltd, 2005, pp. 1-15.
[3] J.F. Watts, J. Wolstenholme, The Electron Spectrum: Qualitative and Quantitative Interpretation, in: An Introduction to Surface Analysis by XPS and AES, John Wiley & Sons, Ltd, 2005, pp. 59-77.
[4] J.F. Watts, J. Wolstenholme, Applications of Electron Spectroscopy in Materials Science, in: An Introduction to Surface Analysis by XPS and AES, John Wiley & Sons, Ltd, 2005, pp. 113-164.
[5] F. Charles S, Prog Surf Sci, 16 (1984) 275-388.
[6] S.M. Goldberg, C.S. Fadley, S. Kono, J Electron Spectrosc, 21 (1981) 285-363.
[7] J.J. Yeh, I. Lindau, Atomic Data and Nuclear Data Tables, 32 (1985) 1-155.
[8] K.S. Birdi, Scanning Probe Microscopes :Applications in Science and Technology, (2003).
[9] P.A. Redhead, Vacuum, 12 (1962) 203-211.
[10] E.I. Ko, J.B. Benziger, R.J. Madix, J Catal, 62 (1980) 264-274.
[11] D.M. Mattox, Handbook of Physical Vapor Deposition (PVD) Processing, (1998) 31.
[12] M. Busch, PhD Thesis University of Gothenburg, (2012).
[13] W. Koch, M.C. Holthausen, Elementary Quantum Chemistry, in: A Chemist's Guide to Density Functional Theory, Wiley-VCH Verlag GmbH, 2001, pp. 3-18.
[14] W. Kohn, A.D. Becke, R.G. Parr, The Journal of Physical Chemistry, 100 (1996) 12974-12980.
[15] N.S.O. A. Szabo, Mc Graw-Hill Publishing Company, New York, , (1982).
[16] D.R. Hartree, 24 (1928) 89–110.
[17] D.R. Hartree, 24 (1928) 111–132.
[18] W. Kohn, Rev Mod Phys, 71 (1999) 1253-1266.
[19] B. Hammer, L.B. Hansen, J.K. Nørskov, Phys Rev B, 59 (1999) 7413-7421.
[20] C.J. Cramer, D.G. Truhlar, Phys Chem Chem Phys, 11 (2009) 10757-10816.
[21] H.J. Kulik, M. Cococcioni, D.A. Scherlis, N. Marzari, Phys Rev Lett, 97 (2006) 103001.
[22] J. Enkovaara, C. Rostgaard, J.J. Mortensen, J. Chen, M. Dułak, L. Ferrighi, J. Gavnholt, C. Glinsvad, V. Haikola, H.A. Hansen, H.H. Kristoffersen, M. Kuisma, A.H. Larsen, L. Lehtovaara, M. Ljungberg, O. Lopez-Acevedo, P.G. Moses, J. Ojanen, T. Olsen, V. Petzold, N.A. Romero, J. Stausholm-Møller, M. Strange, G.A. Tritsaris, M. Vanin, M. Walter, B. Hammer, H. Häkkinen, G.K.H. Madsen, R.M. Nieminen, J.K. Nørskov, M. Puska, T.T. Rantala, J. Schiøtz, K.S. Thygesen, K.W. Jacobsen, Journal of Physics: Condensed Matter, 22 (2010) 253202.
[23] J.J. Mortensen, L.B. Hansen, K.W. Jacobsen, Phys Rev B, 71 (2005) 035109.
[24] S.R. Bahn, K.W. Jacobsen, Computing in Science & Engineering, 4 (2002) 56-66.
[25] P.E. Blöchl, Phys Rev B, 50 (1994) 17953-17979.
[26] S. García-Gil, A. García, N. Lorente, P. Ordejón, Phys Rev B, 79 (2009) 075441.
[27] H. Lin, J.C. Rauba, K. Thygesen, K. Jacobsen, M. Simmons, W. Hofer, Front. Phys. China, 5 (2010) 369-379.
[28] R.E. Prange, Physical Review, 131 (1963) 1083-1086.
[29] J. Tersoff, D.R. Hamann, Phys Rev B, 31 (1985) 805-813.
[30] I. Borbath, D. Guban, Z. Paszti, I.E. Sajo, E. Drotar, J.L.G. de la Fuente, T. Herranz, S. Rojas, A. Tompos, Top Catal, 56 (2013) 1033-1046.
[31] C. Creemers, S. Helfensteyn, Appl Surf Sci, 167 (2000) 216-229.

3 Preparation and phase diagram

3.1 Clean (1×2)-Pt(110) surface

All the STM measurements reported in this chapter were performed in an Omicron variable temperature (VT) STM system. The instrument consists of a UHV preparation chamber with a base pressure of 2×10^{-10} mbar containing equipment for sample sputtering, thermal annealing, Sn evaporation, precise gas dosing. For all the experiments, the (1×2)-Pt(110) surface termination was obtained by cycles of Ar^+ sputtering and annealing at 973 K, followed by a short flash in oxygen at 10^{-7}mbar to eliminate residual carbon on the Pt surface. STM topographies were acquired in constant current mode at room temperature (RT) using PtIr electrochemically etched tips. Tip bias values (V_T) are reported for all images. The cleanness and order of the final surface was checked by LEED and photoemission experiments, while Figure 3-1 presents a typical LEED pattern and topography of (1×2)-Pt(110) surface.

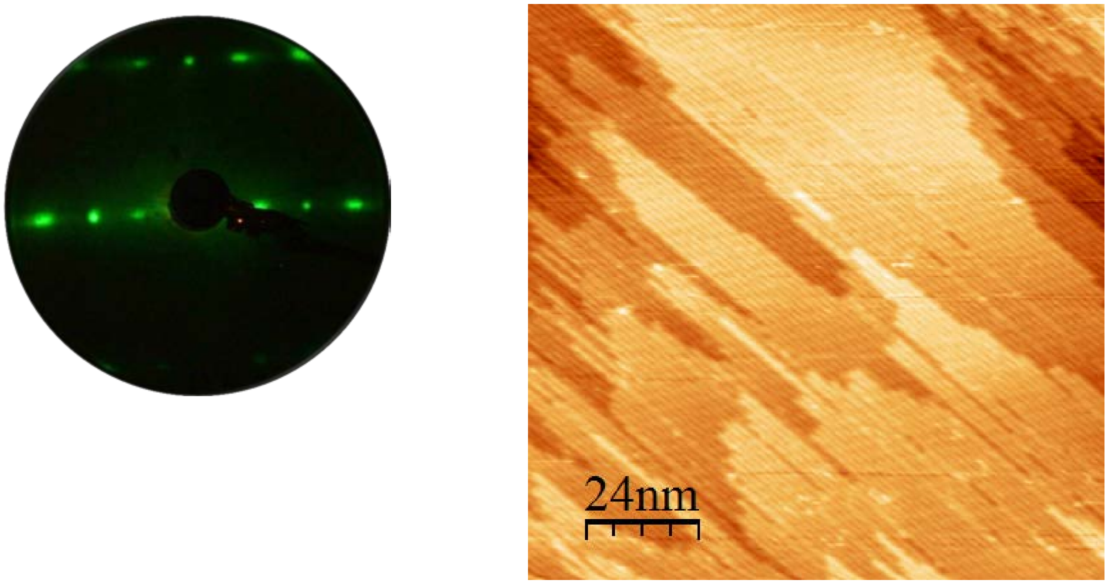

Figure 3-1. (1×2)-Pt(110) surface alloy : (a) LEED pattern at 49eV and (b) STM image, V_t=1000mV.

3.2 PtSn/Pt(110) surface alloys and their oxidized SnO_x derivatives

The Sn overlayers were deposited from an e-beam evaporator in UHV conditions using a molybdenum crucible filled with high purity Sn pellets (Mateck 99.99%). The calibration of the Sn deposition rate was obtained by STM measurements. In the following we will make reference to a Sn monolayer equivalent (MLE) defined as 1 Sn atom per Pt(110) surface unit cell, i.e., 1.8×10^{15} atoms/cm^2. To obtain the surface alloys, UHV thermal treatments were carried out at different temperatures and times (see below). After annealing the samples, the surface structures were characterized by LEED. To simplify the name of the obtained surfaces, p(3×1)PtSn/Pt(110) and p(6×1)PtSn/Pt(110) were shorten as p(3×1) surface and p(6×1) surface respectively.

The experimental phase diagram summarizing the whole set of experimental data discussed in this thesis is reported in Figure 3-2. In a previous paper, we already reported on the preparation of the p(4×1) PtSn/Pt(110) surface alloy [1]. However, the data reported in Figure 3-2 represent a refinement of the experimental conditions after a further optimization. It should also be stressed that kinetic effects have a large impact on the final results. In fact, a significant portion of the deposited Sn undergoes bulk diffusion, which is strongly dependent on both the deposition rate and the annealing temperature and time. As a consequence, the effective Sn surface coverage is very sensitive to the adopted procedure. In practice, this means that the vertical lines reported in Figure 3-2 should be considered as transition regions.

3.2.1 PtSn/Pt(110) surface alloys

Different amounts of Sn (ranging from 0.5 to 3.0 MLE) were evaporated at RT on the clean (1×2) reconstructed Pt(110) substrate and subsequently annealed in UHV. The choice of this particular Pt surface was suggested by the easy mass transfer that can be achieved on it by thermal activation, which facilitates the alloying process. Depending on the actual Sn dose and on the UHV annealing temperature, three different PtSn surface alloys were obtained under optimized experimental conditions.

When the Sn dose is ranging between 0.5-1.5 MLE and the sample is UHV-annealed at 625 K (with the following thermal ramp: heated up at 60 K/min, kept at 625 K for 5 min and finally cooled down to RT) a clear p(3×1) reconstruction is seen: in Figure 3-3 we report both LEED and STM results indicating the formation of a single prevalent phase. A similar but poorly defined LEED pattern has been reported in the literature after mild sputtering with Ar^+ ions of a $Pt_3Sn(110)$ bulk alloy surface [2]. The large-scale STM topography Figure 3-2(b) indicates that the surface is covered by large flat terraces with some defective points. High resolution STM images show that the surface is covered by corrugated rows running along the [001] direction, giving a superstructure whose unit cell has an area of 0.84 × 0.39 nm^2, in agreement with the LEED pattern. The distinctive feature of the p(3×1) surface is the presence of several missing atoms (highlighted with yellow rectangles) and few ad-atoms (highlighted with green rectangles).

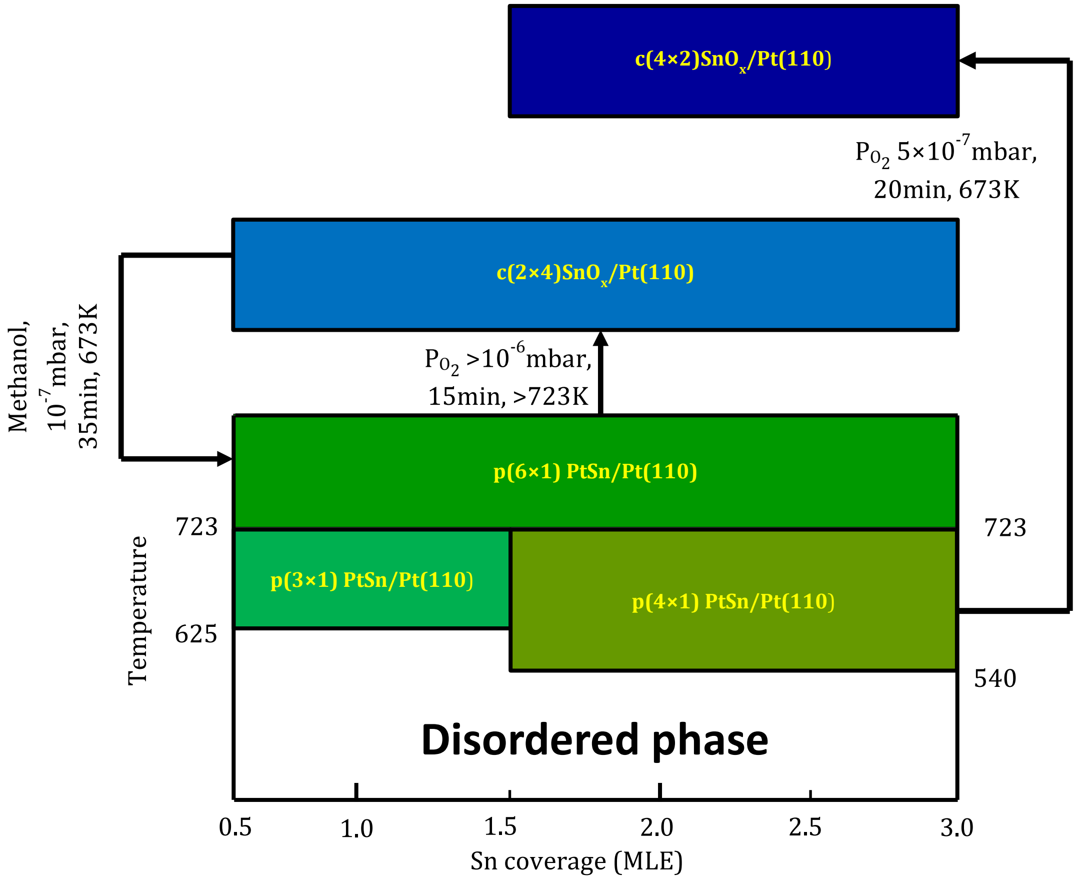

Figure 3-2. Phase diagram for PtSn/Pt(110) surface alloys and their SnO$_x$/Pt(110) oxides.

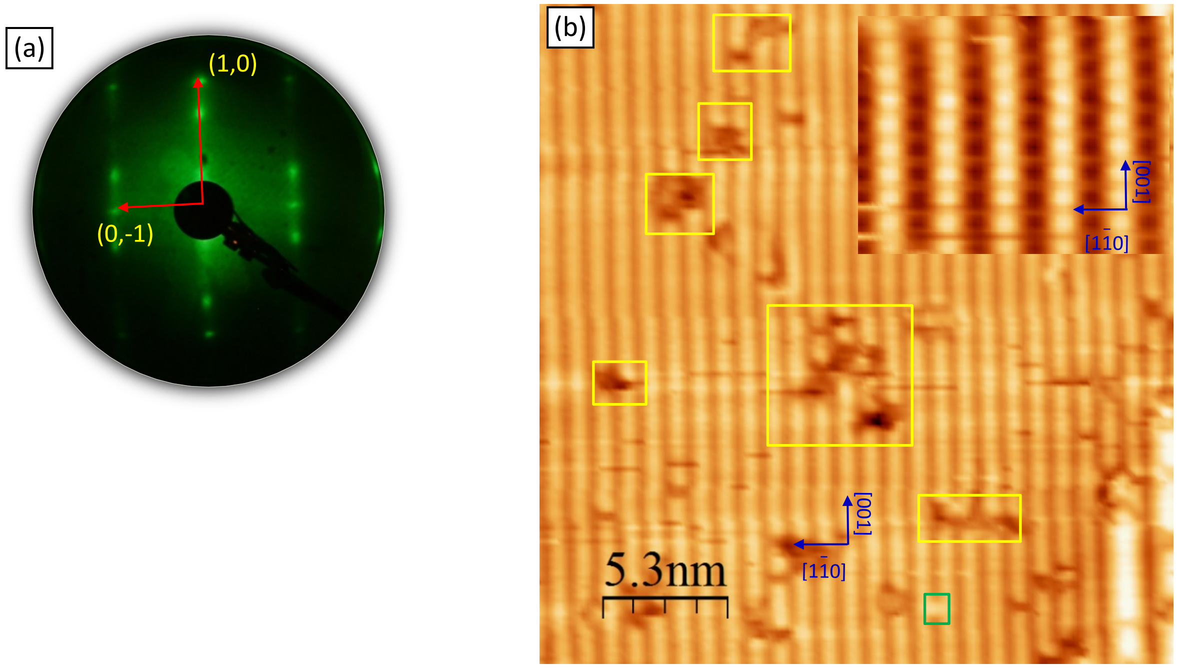

Figure 3-3. p(3×1) PtSn/Pt(110) surface alloy : (a) LEED pattern at 74eV and (b) STM image, V_t=875mV (the inset image is the atomically resolved STM topography, V_t= 875mV).

When a higher Sn amount (from 1.5 MLE to 3 MLE) is dosed on the clean substrate and the sample is annealed to 540 K (following a similar thermal program as above), a p(4×1) pattern is observed by LEED (Figure 3-4) [1, 3]. With respect to previously reported data [1], where an annealing temperature of 623 K was used, after optimization we have found that this phase is observed starting from lower T (540 K). The surface unit cell has an area of 1.12 × 0.39 nm^2, i.e. given by the product of four surface unit vectors in the [1$\bar{1}$0] direction and one in the [001] direction. According to large-scale STM topographies (not reported), the surface is covered by rectangular terraces with sizes ranging from 5 × 10 nm^2 to 12 × 40 nm^2 and steps with an apparent height of 5-20 Å, which produce a high surface roughness. High resolution STM data [1] indicate that the surface is homogenously covered by biatomic stripes running along the [001] direction. In ref. [1] we have already reported a model of the p(4×1) PtSn/Pt(110) surface alloy based on DFT calculations: as shown in Figure 3-4(c), the structure can be described as a (4×1) termination over a Pt_3Sn(110) near-surface ordered alloy. In the top layer, Sn atoms on the ridges are surrounded only by Pt atoms in the first layer, while Sn atoms in the second layer interact with 3 Pt atoms and 3 Sn atoms. The peculiar dependence of the STM pattern on the applied bias, coupled with the DFT results, allowed us to monitor the compositional order in deep layers [1].

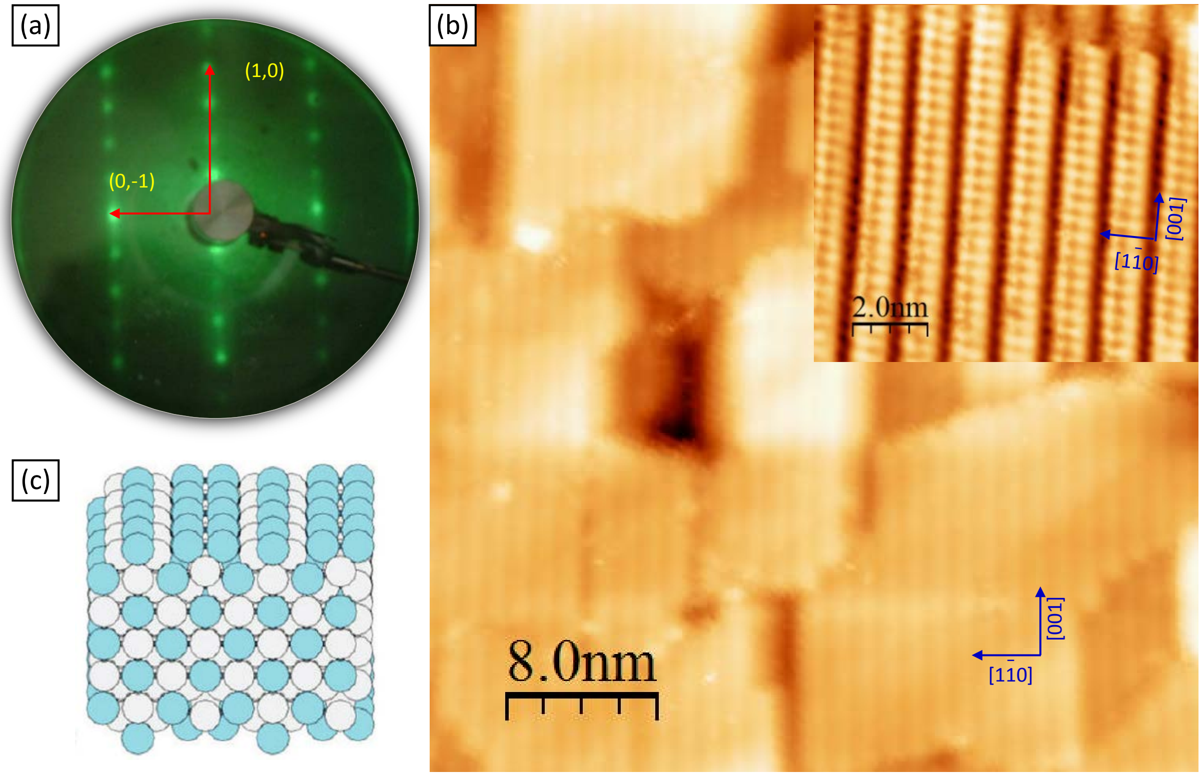

Figure 3-4. p(4×1) PtSn/Pt(110) surface alloy: (a) LEED pattern at 61 eV, (b), STM image, V_t=987mV (the inset image is the atomically resolved STM topography, V_t= -10mV) and (c) atomic model (from ref [1]).

When either the p(3×1) PtSn/Pt(110) or the p(4×1) PtSn/Pt(110) surfaces are annealed in UHV to 723 K with ramp of 120K/min, a new p(6×1) reconstruction is formed, as evidenced by the LEED pattern reported in Figure 3-5(a). A similar p(6×1) reconstruction is apparent in the STM image reported by Hoheisel et.al [4] when studying the annealing of the PtSn(110) bulk alloy, but no comment on it is reported in the paper. Since the coverage giving rise to the p(4×1) reconstruction is higher than the one leading to the p(3×1) superstructure, it turns out that appreciable Sn bulk diffusion occurs during the annealing. Large-scale STM pictures of the p(6×1) PtSn/Pt(110) phase show that the surface is covered with small rectangular terraces with an area ranging from 5 × 10 nm^2 to 10 × 20 nm^2, with step heights of 2-5 Å. The terraces are even smaller than those on the p(4×1) surface. The corresponding local STM topography (Figure 3-5(b)) shows that the surface is covered by highly corrugated stripes running along the [001] direction. Atomically resolved images allow us to identify a 1.68 × 0.39 nm^2 rectangular unit cell, in agreement with the LEED results.

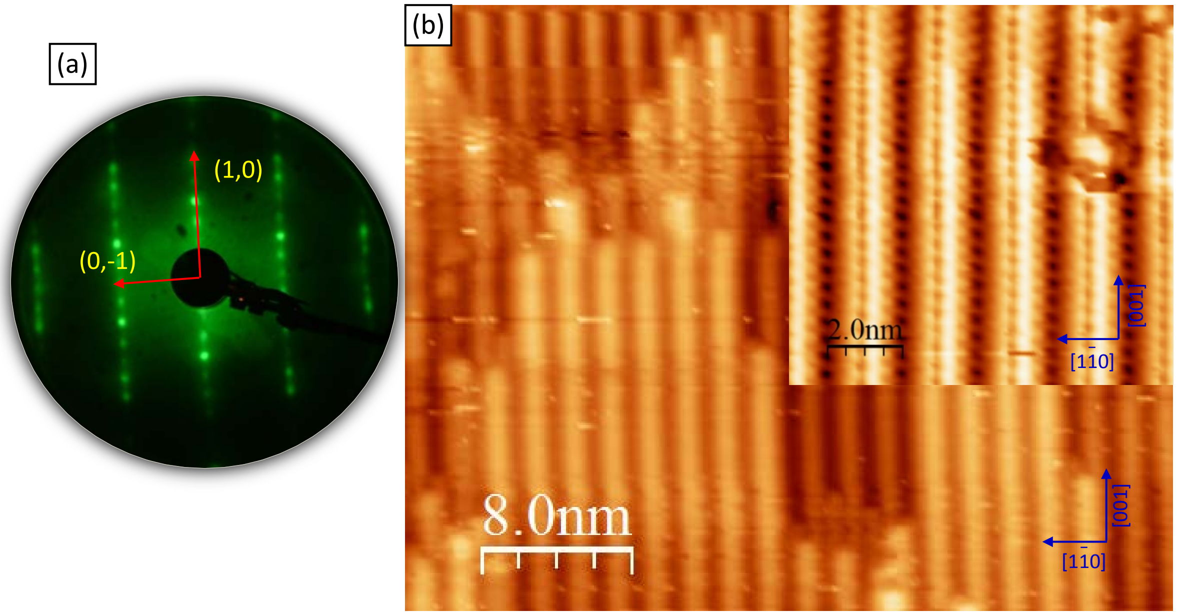

Figure 3-5. p(6×1) PtSn/Pt(110) surface alloy: (a) LEED pattern at 80eV and (b) STM image, V_t=-1000mV (the right inset image is the atomically resolved STM topography, V_t=550mV).

The line profile analysis of the three surface alloys is presented in Figure 3-6: the p(3×1) reconstruction has the lowest corrugation, while p(6×1) is the most corrugated among the three, more precisely the peak to valley apparent height along the [1-10] direction is 0.5 Å for the p(3×1), 1.5Å for the p(4×1):, and 2.0 Å for the p(6×1), respectively.

Moreover, we have investigated in detail also the boundary between the p(3×1) and the p(6×1), as shown in Figure 3-7, where black and dashed rectangles indicate the unit cells of the p(6×1) and the p(3×1) superstructures, respectively. The bright lines of the p(6×1) termination are midway between two adjacent p(3×1) stripes. The line profile reported in the inset of Figure 3-7shows that the apex of the p(6×1) corrugation (position a in the profile) is slightly lower than the one of the p(3×1) phase (position b in the STM image): in other words the two phases are roughly coplanar and in lateral registry, so that a roughening transition from p(3×1) to p(6×1) driven by surface energy minimization seems the likely mechanism for the interconversion.

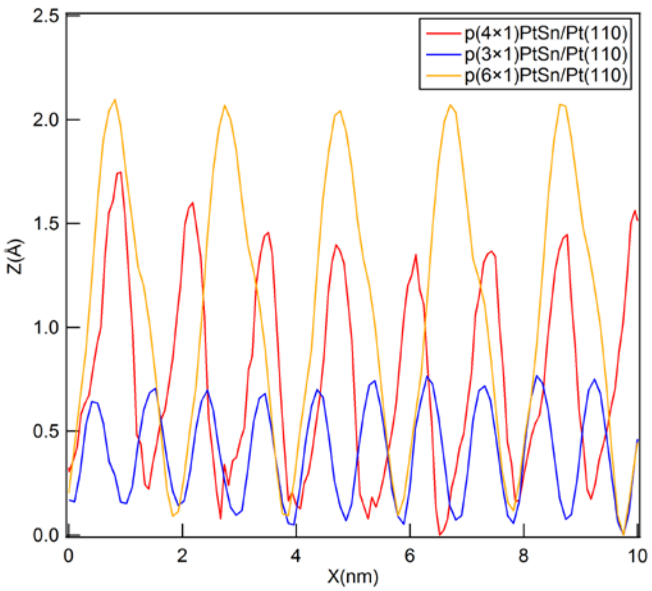

Figure 3-6. Line profiles along the [1$\bar{1}$0] direction of the three PtSn surface alloys on Pt(110).

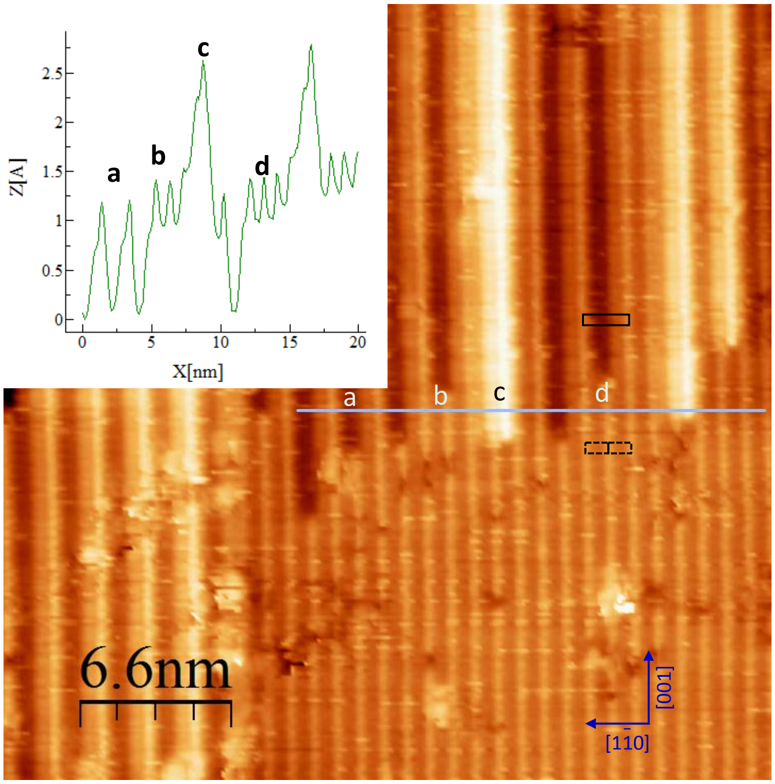

Figure 3-7. STM image of a region containing both the p(6×1) PtSn/Pt(110) and p(3×1) PtSn/Pt(110) terminations (V_t=875 mV). In the inset the line profile along the [1$\bar{1}$0] direction is reported .

In conclusion, Sn deposition and successive UHV annealing can increase the roughness of the Pt(110) surface by forming surface alloys on the surface. The increased roughness can in principle influence the reactivity of surface sites, possibly leading to an enhanced electrochemical activity, since implies the formation of a large amount of coordinatively unsaturated sites.

3.2.2 SnO_x nano-oxides on Pt(110)

When the surface alloys are exposed to an O_2 background in the range of 10^{-7} -10^{-5} mbar [4, 5] and annealed at high T, Sn is oxidized and the formation of SnO_x nano-oxides can be observed. The oxidation process has been followed step-by–step by high synchrotron radiation photoemission spectroscopy.

If the oxidation is carried out under nonspecific conditions, a mixture of different and disordered nano-oxides is obtained. However, procedures to obtain single and well-ordered phases have been optimized. For example, starting from the p(6×1) PtSn/Pt(110) and annealing it at $P_{O_2}>10^{-6}$ mbar and T= 723 K (with the following thermal ramp: heated up at 60 K/min, held at 723 K for 5-15 min, and finally cooled down to RT), a c(2×4) SnO_x/Pt(110) LEED pattern is obtained Figure 3-9 (a)).

The corresponding STM images are reported in Figure 3-9(b). In this case, the surface is characterized by large terraces covered by variable amounts of highly corrugated bright spots arranged into chessboard with a c(2×4) periodicity with respect to the substrate, as confirmed by the fast Fourier transform image reported in Figure 3-8(c). By connecting the bright spots, it is possible to identify the c(2×4) primitive unit cell, as highlighted by the blue rhombus reported in the top-right inset of Fig. 7b. However, an small fraction of bright spots are characterized by a random registry with the substrate (see yellow circles). A very similar STM appearance has been previously observed on some SnO_x/Pt(111) [6-11] surfaces and was attributed to the presence of variably interconnected SnO_x species forming ultrathin films with an exotic structure. However, the LEED pattern shown in Figure 3-8(a) is very sharp, indicating that the pattern must be associated to an ordered interfacial layer rather than to the arrangement of the bright spots observed by STM, which in general are coherent only on the short range: the bright spots do not form extended ordered clusters or ordered lines of more than four-five units. As a matter of fact, the top-left inset of Figure 3-8(b) reports the high-resolution image of a region with just few bright spots, which allows imaging the layer underneath. In this case a faintly corrugated motif compatible with a c(2×4) periodicity can be clearly observed. The c(2×4) phase therefore seems to be constituted by a highly ordered low corrugation structure that can be randomly decorated by very bright defects in registry with the substrate. The nature of these defective units is not clear at the moment: they could be adsorbed species (hydroxyls), oxygen vacancies, or differently coordinated tin atoms. However, they are fascinating because they are mobile even at room temperature and can be accommodated in a quite variable amount on the c(2×4) net (from a few percent up to more than 50%, e.g. in the two different insets of Figure 3-8(b), respectively).

We have also followed the same thermal treatment by LEED starting from either the p(3×1) or p(4×1) surfaces: both the pristine surfaces are initially transformed into p(6×1) and then the p(6×1) is oxidized into the c(2×4) $SnO_x/Pt(110)$ oxide phase.

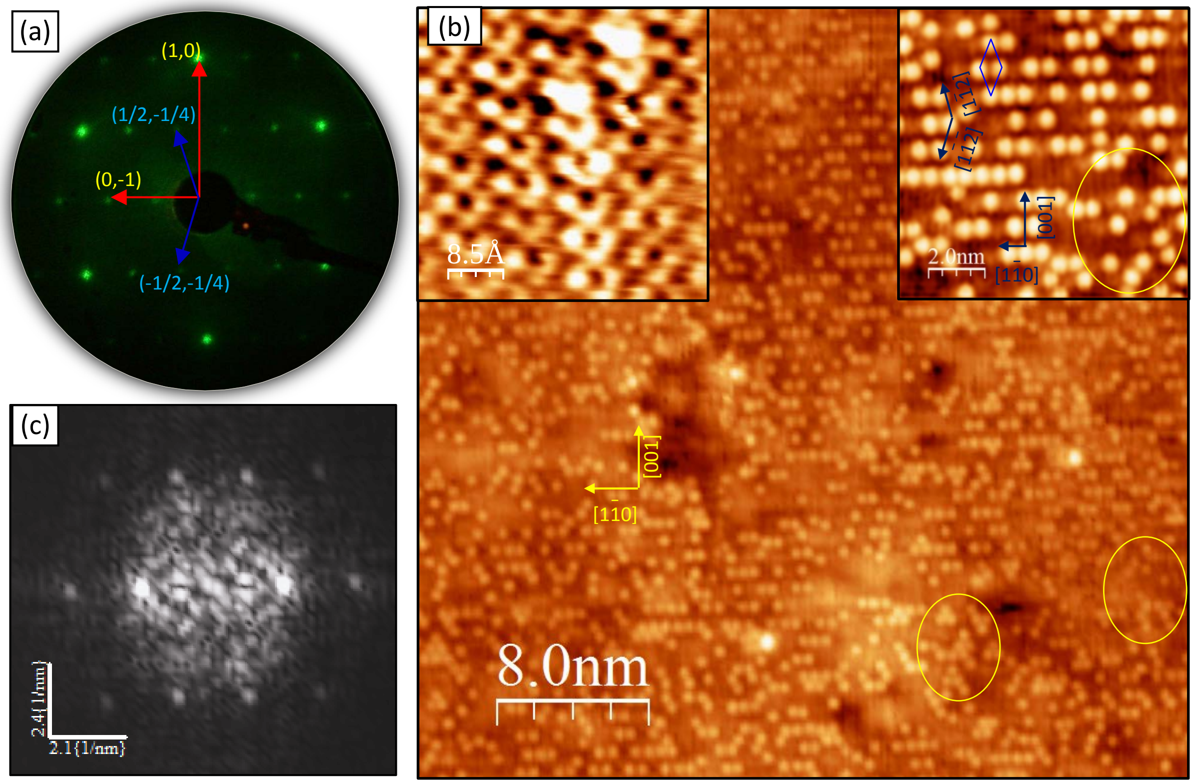

Figure 3-8. c(2×4) $SnO_x/Pt(110)$ nano-oxide: (a) LEED pattern at 63eV and (b) STM image, V_t=658mv. The top-left inset shows a zone where the c(2x4) motif is well evident with atomic resolution, V_t= -528mV. The top-right inset shows the c(2x4) motif of the bright spots (see text). (c) fast Fourier transform image of the top-right inset in (b).

If the oxygen pressure and the annealing temperature are reduced, we obtained a single phase only when starting from the p(4×1) surface alloy (e.g. P_{O_2} 5×10^{-7} mbar at 673 K for 20 min). According to the LEED pattern (Figure 3-9(a)), and STM topography (Figure 3-9(b)), the surface is transformed into a c(4×2) regular pattern with respect to the substrate. A similar c(4×2) SnO_x/Pt(110) reconstruction can be also prepared from Pt_3Sn(110) bulk alloy after adsorption of several thousand Langmuir of O_2 at 750K[4]. Our STM images show regularly spaced bright spots, which are analogous to the bright bumps observed on the SnO_x/Pt(111) surface [6-11]. However, fewer missing spots are observed in our case than on the SnO_x/Pt(111) system.. The surface cell has an area of 1.12 × 0.78 nm^2, which corresponds to four unit cells in the $[1\bar{1}0]$ direction and two in the [001] direction. Different domains separated by several zigzag-like boundaries (aligned with the $[\bar{2}21]$ and [221] directions and highlighted with red lines in Figure 3-9) can be easily observed. Such line defects are identified as antiphase domain boundaries. These results are consistent with SnO_x nano-oxides grown by oxidation of the Pt_3Sn(110) bulk alloy [4].

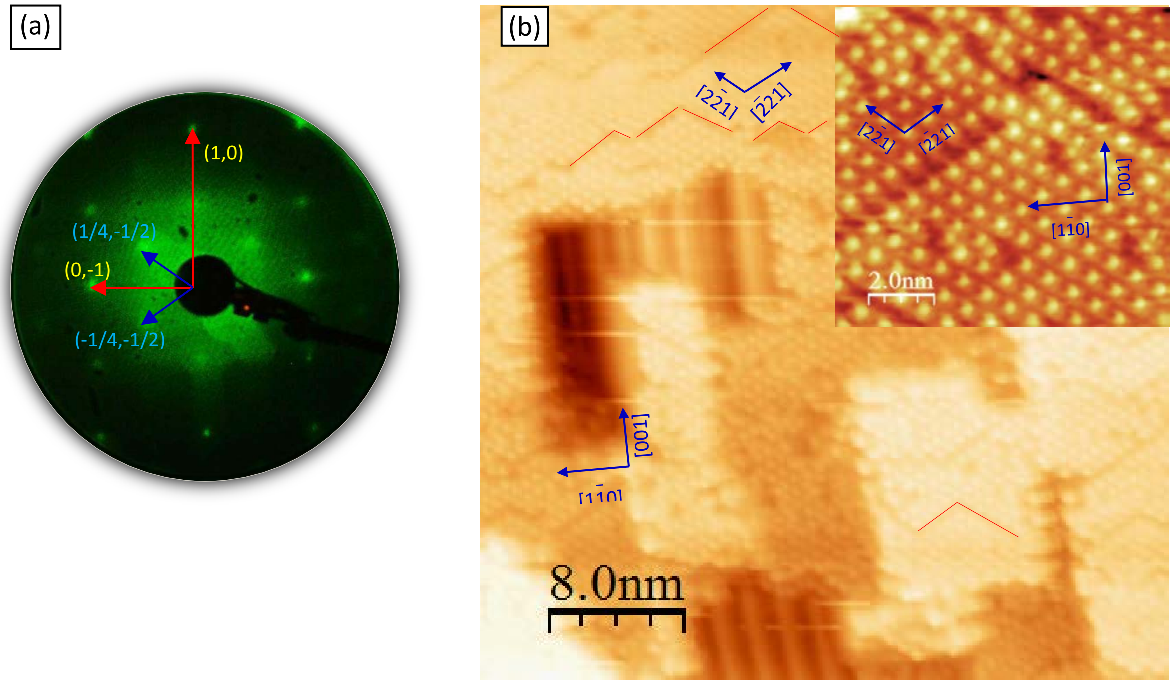

Figure 3-9 c(4×2) SnO_x/Pt(110) nano-oxide: (a) LEED pattern at 63eV and (b) STM image, V_t=1234mV, of. The inset image is the atomically resolved topography of the surface alloy oxide, V_t = -34mV.

Finally, the reduction of the c(2×4) SnO_x/Pt(110) phase was attempted by using methanol. The sample was maintained at 673 K and then exposed to ca 200 L of methanol. The surface was checked by LEED before and after the reaction, and the LEED patterns are shown in Figure 3-10. According to the LEED results, it can be concluded that the oxidized surface can be reduced from c(2×4) SnO_x/Pt(110) to p(6×1) PtSn/Pt(110).

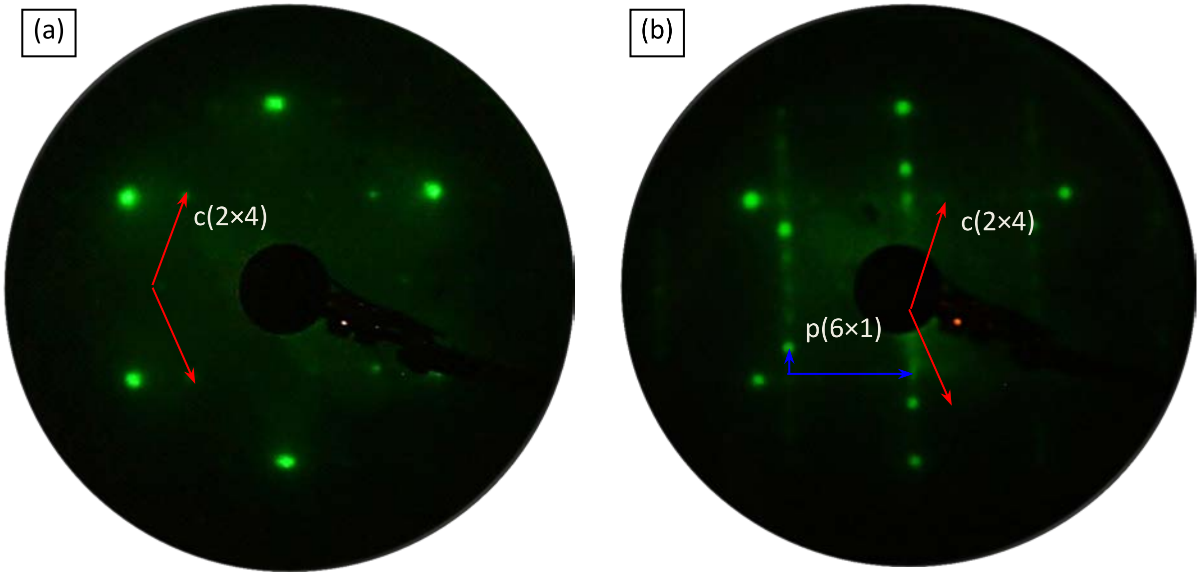

Figure 3-10 LEED patterns of (a) the pristine c(2×4) SnO_x /Pt(110) phase (82.0 eV) and (b) the same surface after reaction with methanol at 10^{-7}mbar (80.0 eV).

3.3 Conclusions

a. Three distinct Pt-Sn surface alloys, obtained by means of UHV Sn deposition on the (1×2) reconstructed Pt (110) surface and UHV annealing, have been isolated by a careful optimization of the growth conditions. In addition, their conversion into SnO_x surface nano-oxides as a consequence of oxygen dosing has been explored. All phases have been structurally and morphologically characterized by means of LEED and STM measurements.

b. Besides to the already known p(4×1) PtSn/Pt(110) superstructure[1] whose growth conditions have been now further refined, a new p(3×1) PtSn/Pt(110) surface alloy has been obtained starting from lower Sn coverage values. Both phases are shown to convert into a p(6×1) PtSn/Pt(110) superstructure after annealing at 723 K. Surface alloying is shown to imply a substantial roughening of the substrate surface.

c. Annealing the p(6×1) phase in an oxygen background at a pressure higher than 10^{-6} mbar and at T=723 K leads to the formation of a c(2×4) SnO_x/Pt(110) surface nano-oxide. Under the same conditions, the p(3×1) and p(4×1) PtSn/Pt(110) surface alloys lead to the same c(2×4) nano-oxide, though not directly, but rather through the p(6×1) intermediate. In turn, the c(2×4) oxide superstructure can be switched back into the p(6×1) Sn_x/Pt(110) surface alloy by dosing methanol.

d. Finally, a different nano-oxide phase characterized by a c(4x2) periodicity can be obtained exclusively from the higher coverage p(4×1) PtSn/Pt(110) surface alloy at a somewhat lower oxygen pressure (5×10^{-7}mbar) and annealing temperature (673 K).

e. A phase diagram summarizing these observations has been proposed.

References

[1] S. Agnoli, G. Barcaro, A. Barolo, A. Fortunelli, M. Sambi, F. Sedona, M. Di Marino, T. Skala, G. Granozzi, J Phys Chem C, 115 (2011) 14264-14269.
[2] V. Stamenkovic, M. Arenz, B.B. Blizanac, P.N. Ross, N.M. Markovic, J New Mat Electr Sys, 7 (2004) 125-132.
[3] N. Tsud, T. Skala, K. Veltruska, M. Skoda, K.C. Prince, V. Matolin, J Phys-Condens Mat, 23 (2011).
[4] M. Hoheisel, S. Speller, A. Atrei, U. Bardi, G. Rovida, Phys Rev B, 71 (2005).
[5] N. Tsud, T. Skala, F. Sutara, K. Veltruska, V. Dudr, M. Yoshitake, K.C. Prince, V. Matolin, J Phys-Condens Mat, 21 (2009).
[6] M. Batzill, D.E. Beck, D. Jerdev, B.E. Koel, J Vac Sci Technol A, 19 (2001) 1953-1958.
[7] M. Batzill, D.E. Beck, B.E. Koel, Appl Phys Lett, 78 (2001) 2766-2768.
[8] M. Batzill, D.E. Beck, B.E. Koel, Phys Rev B, 64 (2001) 245402.
[9] M. Hoheisel, S. Speller, W. Heiland, A. Atrei, U. Bardi, G. Rovida, Phys Rev B, 66 (2002) 165416.
[10] A. Atrei, U. Bardi, G. Rovida, M. Torrini, M. Hoheisel, S. Speller, Surf Sci, 526 (2003) 193-200.
[11] M. Batzill, J. Kim, D.E. Beck, B.E. Koel, Phys Rev B, 69 (2004).

4 Structure and reactivity of PtSn/Pt(110) surface alloys

4.1 Characterizations and their models

All the samples were checked by LEED and also consequently characterized by UHV-STM. All the STM images are presented as following.

4.1.1 p(3x1) PtSn/Pt (110)

4.1.1.1 LEED and STM images

The STM images of p(3×1) surface are presented in Figure 4-1. According to the STM images, the distance between the rows along with $[1\bar{1}0]$ direction is 0.80±0.05nm and the one between the bright spots along with the [001] direction is 0.40±0.03 nm. The parameters of the unit cells indicate that the surface has a p(3×1) reconstruction meaning three atoms along [001] direction and one atom along with the $[1\bar{1}0]$ direction in every unit cell.

4.1.1.2 Models and DFT calculations

Since this phase can be obtained in a wide range of Sn coverage (ie from 0.5ML to 1.5ML), the model for this structure was proposed assuming a variable amount of Sn in the substrate as shown in Figure 4-2. We report the formation energy with different reference including Pt_3Sn and $Pt_{15}Sn$, and the results considered the backside effects introduced previously in Chapter 2 for the two references are also listed. The comparison of difference among the listed models exhibits the stability trend of models is not influenced by the reference. Model 1 and model 2 have the same stoichiometry, while they have different surface structures. The model 1 has a Pt-rich surface, whereas the model 2 surface is Sn-rich. By the comparing the formation energies calculated by DFT of model 1 (-6.45eV) and model 2(-7.96eV), which have the same stoichiometry, we can infer that model 2 is more stable than model 1. Hence, according to the comparison, the surface having Sn atoms on the surface is more stable. The surface structure might very well depend on the bulk composition. So it is hard to make conclusions based on the results obtained from pure Pt(110) bulk only. Furthermore it is unlikely that penetration of Sn into the bulk does not occur in the described experiments, therefore Pt_xSn_y bulk must be considered.

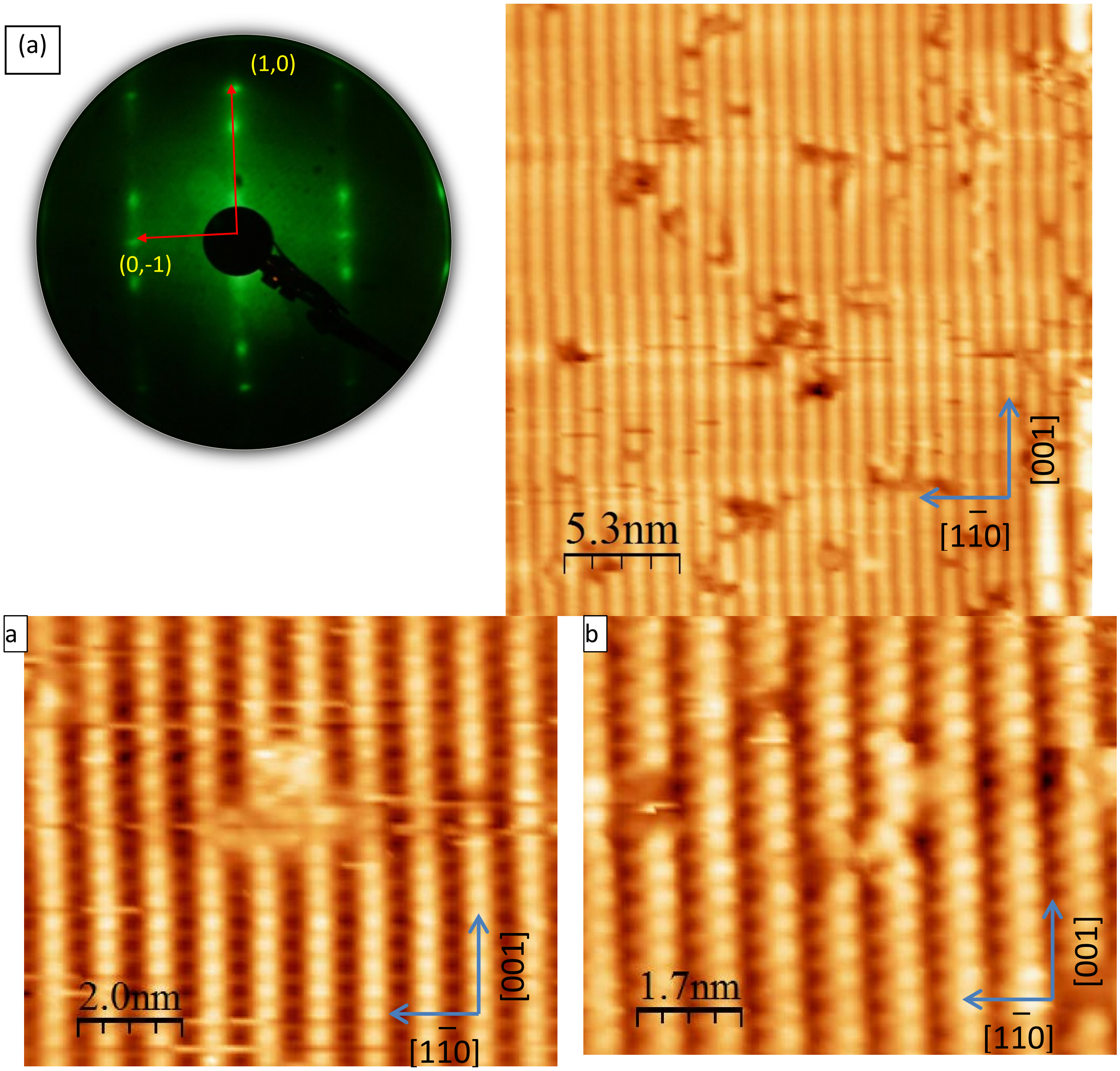

Figure 4-1. p(3×1) PtSn/Pt(110) surface alloy : (a) LEED pattern at 74eV, (b) STM image, V_t=875mV, (c) atomic resolved STM image, V_t=875mV, and (d) STM images with atomic resolution, V_t=1452mV

Based on the surface structures of model 1 and model 2, additional models employing a Pt_xSn_y bulk are proposed and studied by DFT. So, we just list the model having surface structures like model2. Let us consider model 2 to model 5, where we have systematically changed the amount of Sn and its arrangement but keeping the same structure on the surfaces. The formation energies are -7.96eV, -7.94eV, -10.81eV and -11.43eV for model 2, model 3, model 4 and model 5, respectively. So, the model 5, which has the highest Sn content among the discussed four models in the substrate, is the most stable and therefore the most likely candidate as the real structure of the p(3×1) phase .

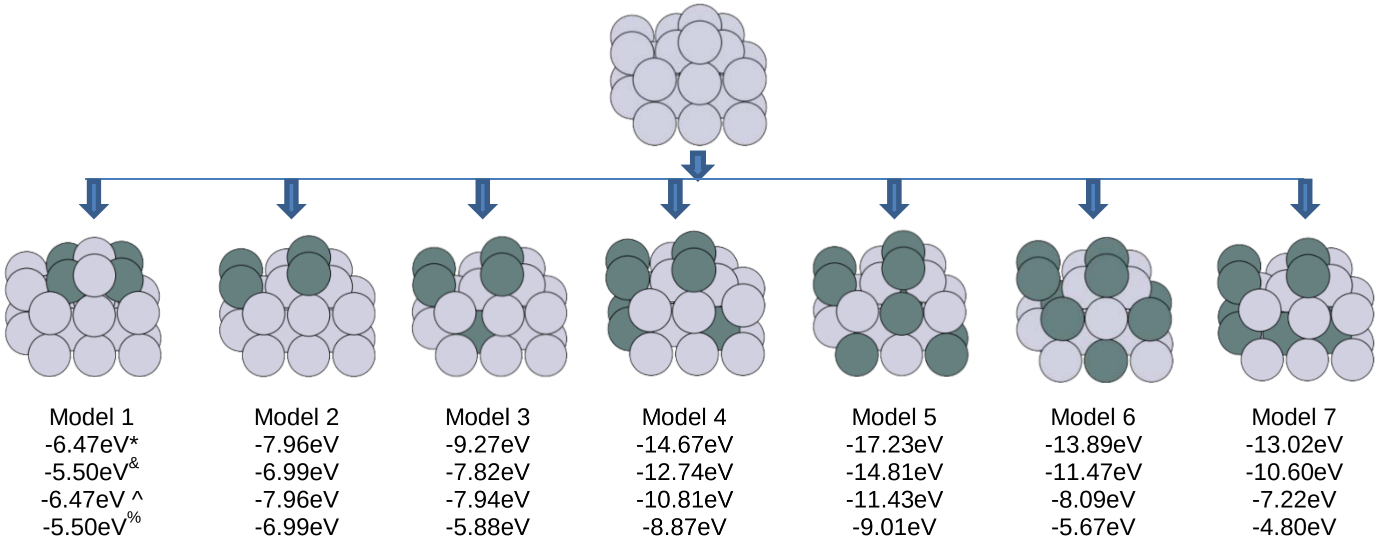

Figure 4-2 Schematic calculation process for formation energies of p(3×1) surface
Reference * Pt_3Sn, & $Pt_{15}Sn$, ^ Pt_3Sn+backside effect, % $Pt_{15}Sn$+backside effect

We have also explored the effect of a different Sn arrangement in the bulk while keeping the overall composition fixed. In this case we considered the model 5, model 6 and model 7, which have the same reconstructed surface, but different bulks (see Figure 4-2). The formation energies of model 5, model 6 and model 7 are -11.43eV, -8.09eV and -7.22eV, respectively, indicating that the model 5 is clearly most stable one.

To corroborate this conclusion we have simulated by DFT the STM images of the model at two different potentials, typical of our experimental conditions, and the results are reported in Figure 4-3. It can be seen that the simulated images contain bright rows that are consistent with the experimental STM topography. We have also performed the simulation for the other models obtaining very similar results, meaning that the STM images of the p(3×1) surfaces are insensitive to the actual bulk structures. Hence, according to the results from DFT calculations and experiments, the surface as in model 2 ~ model 7 are energetically more favorable, and higher Sn concentration in the bulk preferred. So that, the application of pure Pt bulk as model2 is questionable since Sn penetration into bulk is not likely not avoidable in experiment. Based on calculations, model 5 (at Pt_3Sn reference) is clearly the most stable one.

Model 2

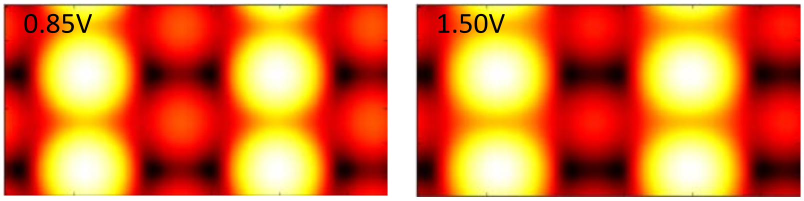

Model 3

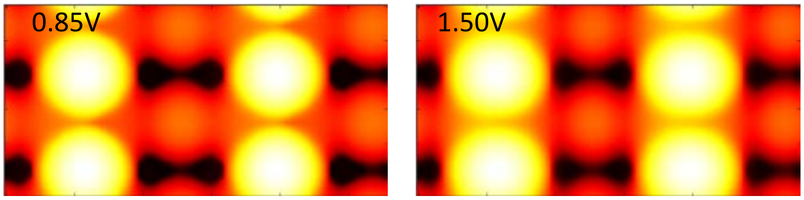

Model 4

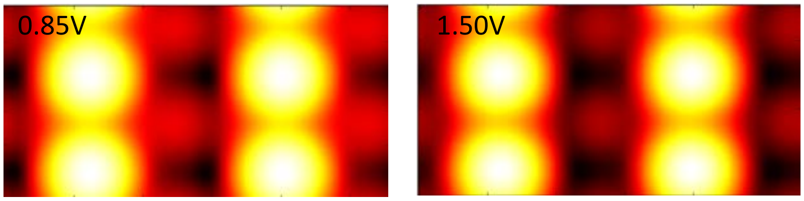

Model 5

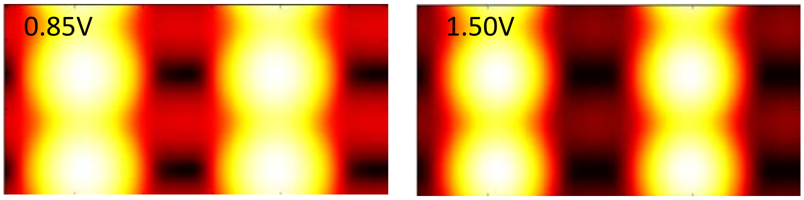

Model 6

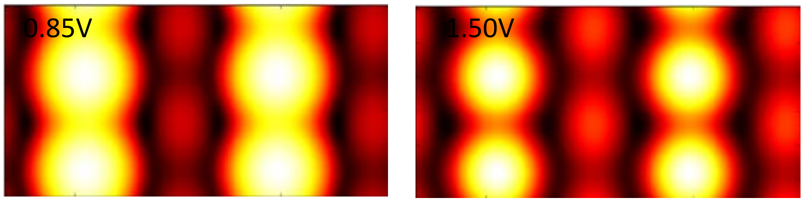

Experimental STM images

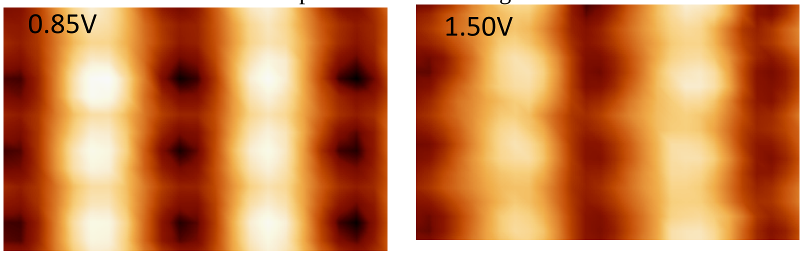

Figure 4-3 simulated STM images of models of the p(3×1) surface and Experimental STM images

The direct comparison between simulated STM images and experimental STM images of the p(3×1) surface (model 5) are showed in Figure 4-4 indicating the simulated images can fit our experimental STM image.

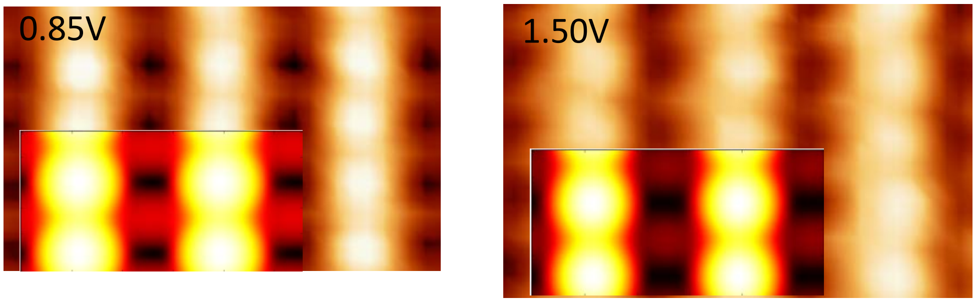

Figure 4-4 Comparison between simulated and experimental STM images of p(3×1) surface - model 5

4.1.2 p(6x1) PtSn/Pt (110)

4.1.2.1 LEED and STM

The LEED patterns and atomic STM images of the p(6×1) surface are presented in Figure 4-5. The STM images show that the surface is covered by distinguished wide and highly corrugated rows running along the [001] direction. The row separation is about 1.70±0.05 nm, which is 6 atomic spacing in the $[1\bar{1}0]$ direction, whereas the periodicity along the [001] direction is about 0.40±0.05 nm, that is one unit cell of the substrate. In conclusion, these parameters indicate the formation of a p(6×1) superstructure. Highly resolved STM images reported in Figure 4-5, can provide some details about the surface structure. According to different tunneling conditions (and more likely of different tip states) (see Figure 4-5(c)) the topographic images show either two close rows in every reconstructed unit along the [001] direction, or only one highly corrugated row, surrounded by two weaker features at both sides.

4.1.2.2 SRPES

To confirm the structure of the p(6×1) surface alloy, a SRPES investigation at different photon energies (125 eV and 60 eV) was carried out. In Figure 4-6 (a) we report the energy region corresponding to Sn4d levels. The spectrum measured at 60 eV presents two peaks, whereas three peaks can be observed in the spectra taken at 125eV. This difference stems from the different sampling depth of the two measurements: more surface sensitive the one at lower energy, whereas at 125 eV the bulk component gets more important. The fitting data of Sn4d of p(6×1) surface indicates that the surface contains four Sn-related species: component a at ~23.95 eV , component b at ~24.25 eV, component c at ~24.70 eV and component d at ~25.19 eV.

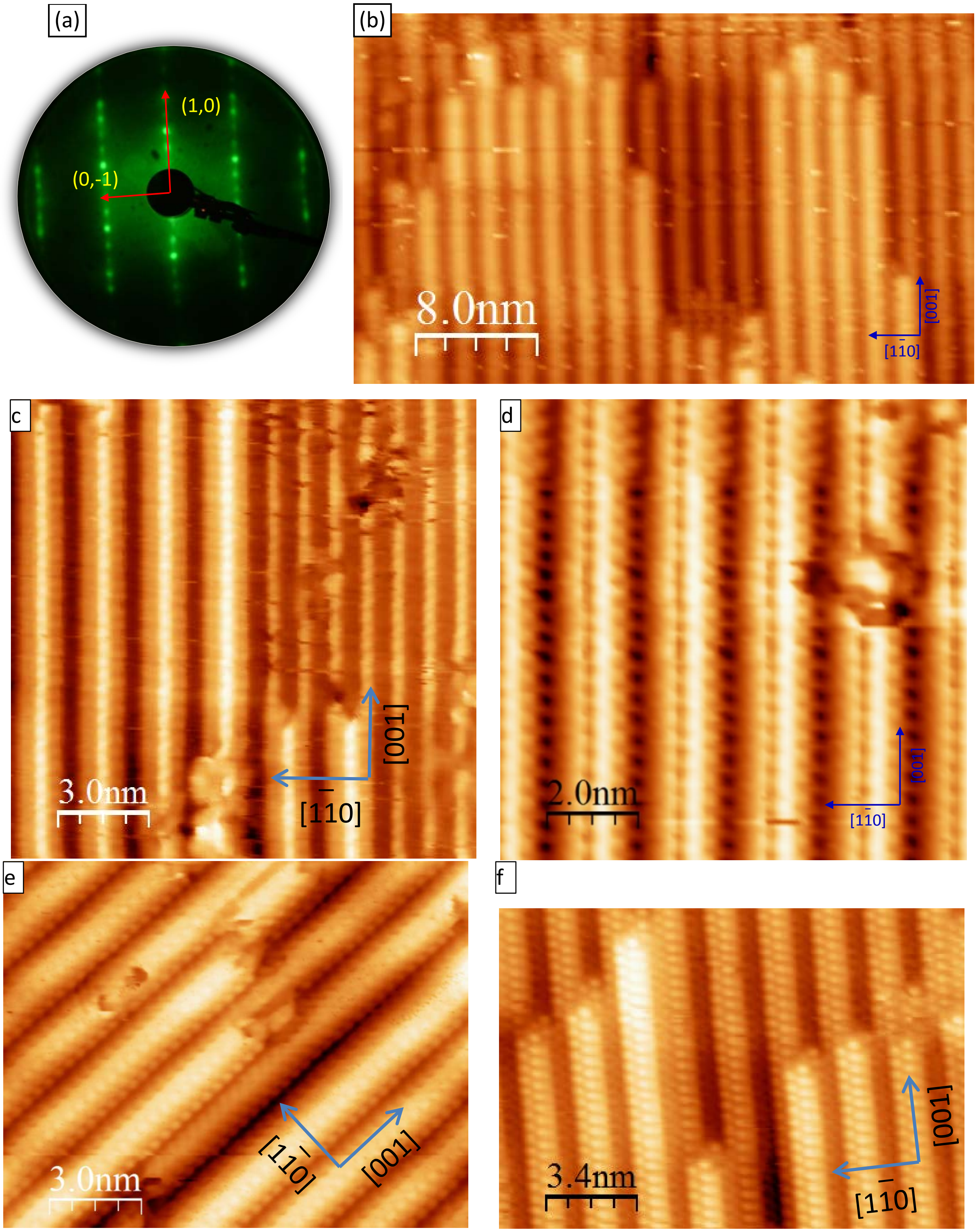

Figure 4-5 p(6×1) PtSn/Pt(110) surface alloy: (a) LEED pattern at 80eV, (b) STM image, V_t = -1000mV , (c), (d) and (e) reported atomic resolved STM image with V_t = 537mV, (f) atomic resolved STM image with tip bias at 537mV and (f) STM topography with tip bias at 1550mV

By the comparison with the values reported in literature, both the peak at ~23.95 eV [1-3] and the one at ~24.27 eV [3] can be assigned to metallic Sn on the surface due to low BE value: the former can be associated to Sn atoms in the topmost layer and the latter to Sn atoms in the second layer. The peaks at ~24.69 eV[1-3] should be connected to bulk species since it is more intense at high rather than low photon energy, and fits nicely with the value reported for Pt_3Sn alloys The peak at ~25.19 eV [4-6] has a very small intensity ratio and can be assigned to partially oxidized Sn (SnO, Sn-OH or Sn-H_2O).

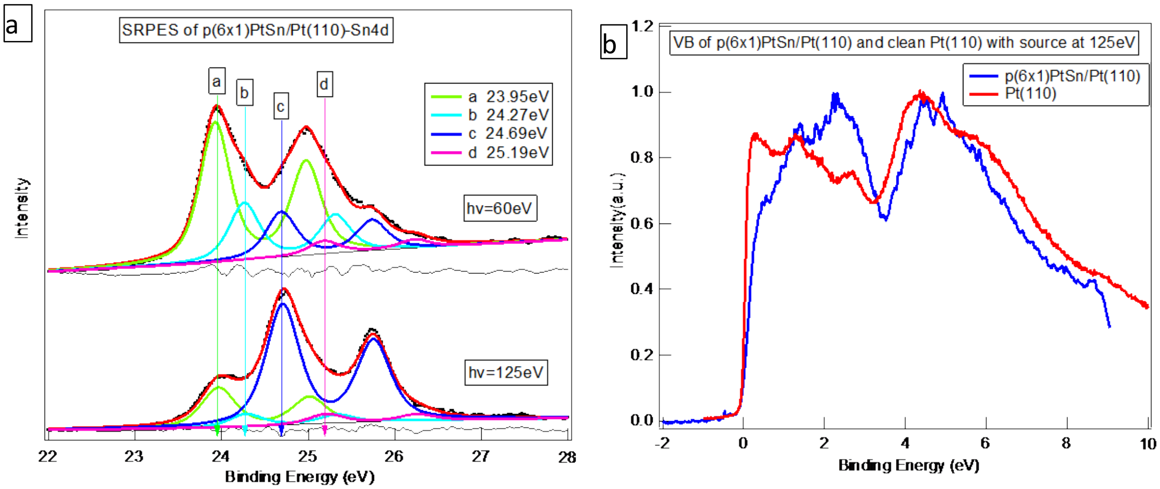

Figure 4-6 SRPES and model of p(6×1) PtSn/Pt(110) surface alloy with source at various energy levels: (a) Sn4d and (b)valence band

The comparison of valance band of p(6×1) and of the clean Pt(110) surface presented in Figure 4-6(d) indicates that the p(6×1) surface presents a smaller density of states in the energy region just below the Fermi level. On the clean Pt substrate, one broad peak centered at 4.4eV is visible as well as and some complex structures below 3 eV which is similar to the results reported in our previous work [1]. After the deposition of of Sn, the VB spectrum of p(6×1) surface develops two broad peaks centered at 2.2 eV and 4.6 eV, and its intensity around Fermi energy level decreases.

4.1.2.3 Models and DFT calculations

In order to determine the atomic structure of the p(6×1) surface alloy we used DFT calculations in order to identify the minimum energy configuration for Sn either in the surface or in the bulk and then we tested the model by simulating the STM images. As starting models for DFT calculations, we constructed a set of test structures based on chemical intuition that could fit the STM contrast in a one bump one atom scheme and were in agreement with the photoemission data (i.e. structure presenting Sn atoms with three different type of chemical environment). These models are shown in Figure 4-7. In Model 1 and model 2, the substrate is $Pt_3Sn(110)$, while in model 3 and model 4 the substrate is Pt(110). Model 1 and model 3, as well as model 2 and model 4 have the same topmost layer. Finally, Model 5 and model 6 shares the same surface reconstruction, which is different from the other four models, but model 5 is based on a $Pt_3Sn(110)$ bulk, while model 6 on pure Pt(110). Model 1 and model 3 have one Pt atom in the center of every reconstructed unit, while model 2 and model 4 have two Pt atoms.

As explained in chapter 2 we adopted several methods to calculate the formation energy of the different structures. However our photoemission data suggest that the selvedge is constituted by Pt_3Sn, therefore in the following we will discuss just the energy values obtained assuming as a reference the Pt_3Sn corrected by the backside effect. It is worth to notice however that this procedure is not arbitrary. Actually, as it can be seen form the values reported in figure 4-7, just little variations are observed by using a different energy reference.

According to the comparison of formation energies by DFT calculation, the formation energies of the model 1 and model 2 are -12.15eV and -12.13eV. They can be considered as the same value as their deviation of energies is 0.02 eV, which is with the error bar from DFT calculation. And the formation energies of model 3 and model 4 is -9.03 and -7.81eV, while the ones of model 5 and model 6 are -11.87eV and -6.72eV. The formation energies of model 3, 4 and 6 are less stable than the one of model 1 & 2 indicating that a Pt_xSn_y bulk as it can be found in Model 1, 2 and 5 is energetically favorable. Besides, according to SRPES of p(6×1), model 3, 4 and 6 can be rule out due to this lower Sn content in the bulk. Hence we will have to confirm the model of the p(6×1) according to further investigation.

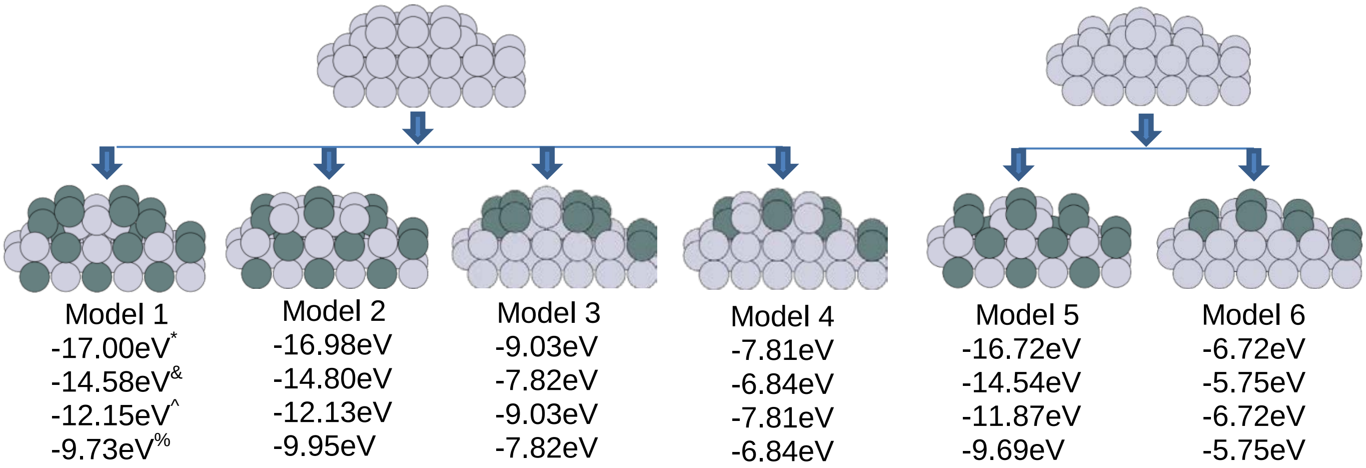

Figure 4-7 Schematic calculation process for formation energies of models for p(6×1) surface
Reference: * Pt$_3$Sn, & Pt$_{15}$Sn, ^ Pt$_3$Sn+backside effect, % Pt$_{15}$Sn+backside effect,

The simulated STM images with various biases are presented in Figure 4-8. According the simulated results of model 1, the images have two rows in every unit along the [001] direction, indicating that the STM of the model is not sensitive with bias but sensitive with surface. The results of model 2 show only a row along with [001] direction at any bias. The STM images of model 3 displays a row with bias at 0.55V, while two rows can be obtained with bias at 1.60V, meaning that this model is very sensitive with bias. The results of model 4 shows the two rows in the every unit along with [001] direction, but a wide single row could be observed with bias at 1.60V. Hence, the simulated images indicate that the tip biases has little impact on the STM topographies of model 1 and model 2, while the one is very dependent on bias for model 3 and model 4. Even the models has same surface structures, such as model 1 and model 3, or model 2 and model4, the simulated STM with various biases can be different. Model 1 and model 3 have similar STM images with bias at 0.55V, but model 1 shows two rows while the mode3 has only one wide row along with [001] direction. The STM image with bias at 0.55V of model 1 has zigzag rows in unit, while the one of model 4 exhibits two rows in the unit along [001] direction. However, if bias increases to 1.60V, the simulation of the two models shows similar STM images including one row in the center and two zigzag rows around the middle row.

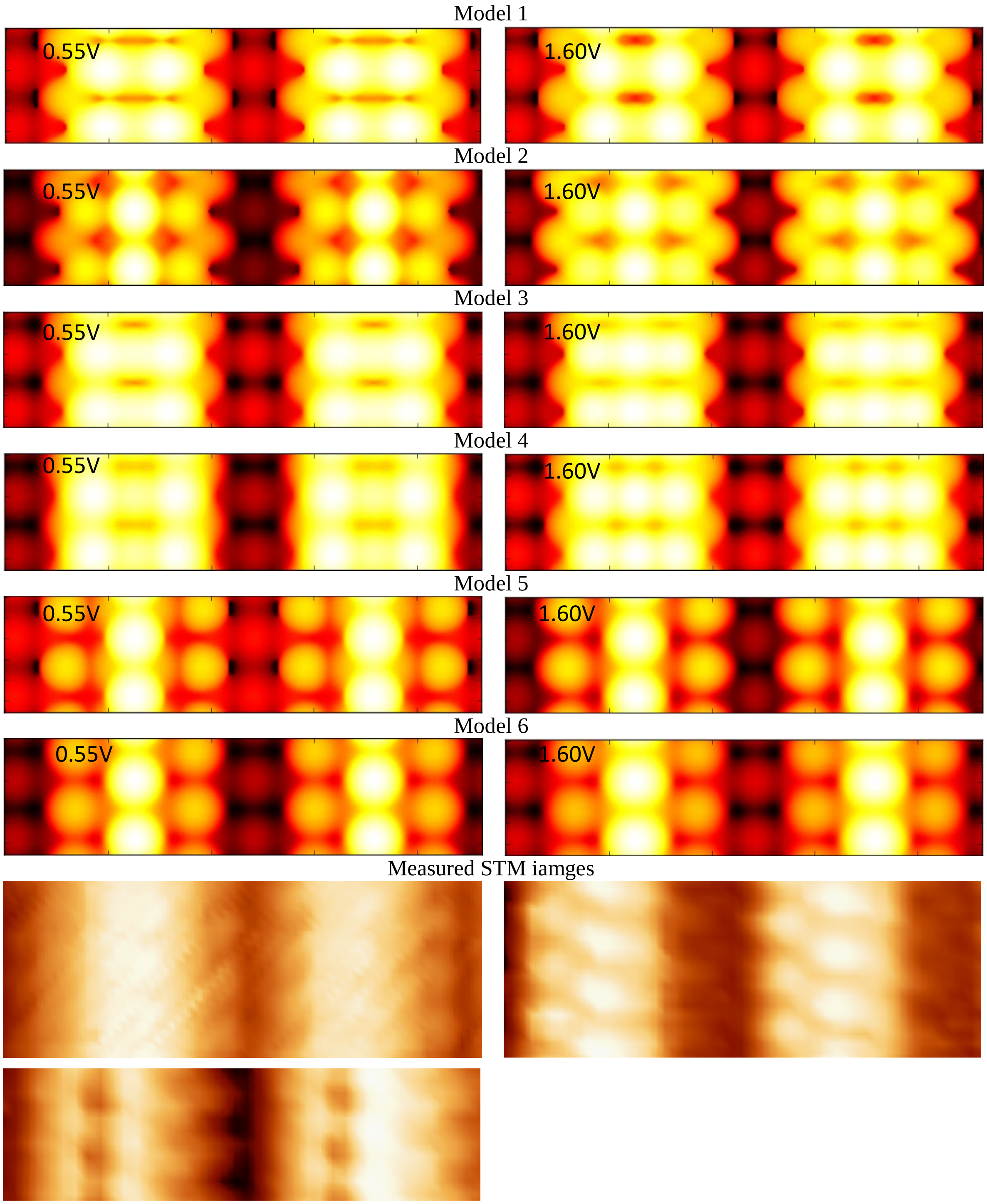

Figure 4-8 Simulated STM images of different p(6×1) models and STM image with corresponding tip biases

So the comparison of the simulated images of model 1, 2, 3, and 4 illustrate that STM images are highly dependent with their substrate composites. And we can further conclude that the STM images of surfaces from precursor of model 1, 2, 3 and 4 are usually morphological sensitive if the bulk is $Pt_3Sn(110)$, and the ones are very tip-bias-sensitive if the substrate is pure Pt(110).

Model 5 and model 6 have the same simulated STM images which have three rows from the simulation containing one bright row in the middle and two less bright rows around the bright row. As some STM images having double bright rows, model 5 and 6 can be disregarded due to their exhibition of constant one bright row along [001] direction.

According to the comparison of simulated and experimental data, model 1 always displays two rows at the both used bias. But the model cannot configure transition between p(3×1) to p(6×1) structures illustrated in Figure 4-9. Hence, Model 2 can be a preferable one. However, we cannot obtain some simulated STM images exhibiting two rows along with [001] direction.

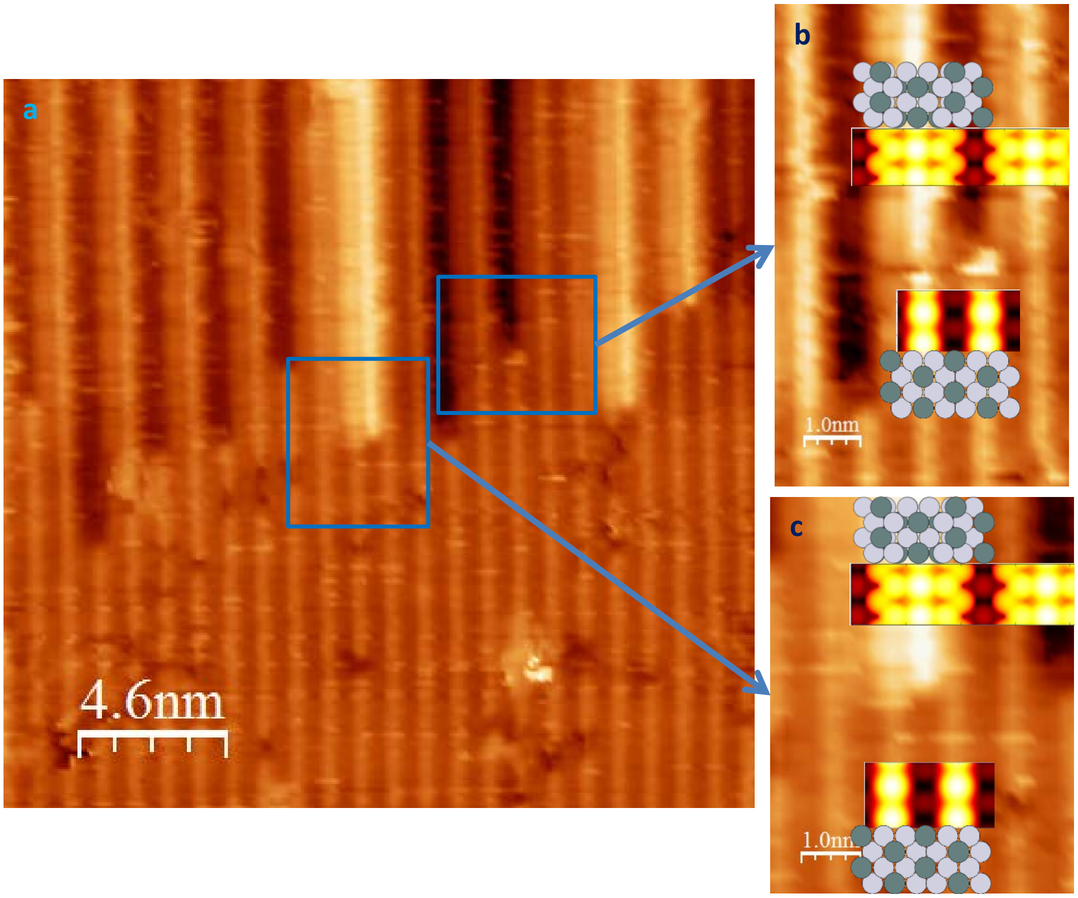

Figure 4-9 STM images of transition between p(6×1) and p(3×1): (a) experimental with tip bias at 1.25V, (b) embedded transition comparison and (c) grown transition comparison of experimental results and simulated STM image including p(3×1) and p(6×1) of model 2

The model 2 having Pt_3Sn(110) bulk cannot exhibit topography with the two row , while the model 4 owing Pt(110) substrate have the same surface structure as the model 2 can obtain the topography. Some models having the same surface structure as model 4 and model 2 on the different bulk compositions with various Sn content were proposed and investigated by DFT calculations. According to the simulated results reported in Figure 4-11, the model 7 and the model 9 can exhibit STM images including one row in the reconstructed unit along with [001] direction at different tunneling current and two rows at relative low tunneling current, which are displayed in Figure 4-11. From the formation energies of model 7 and model 9, model 9 is favorable. Hence, the model of p(6×1) can be very likely on a Pt_xSn_y bulk (based on energetics) and it can also explain the transition between the two model seen from STM images. Besides, compared with all the proposed models, the bulk has a huge influence on the measured STM images, which is also obtained in p(4×1)PtSn/Pt(110) surface[1]. The model 2 surface therefore can in principle explain the appearance of different measured STM images in different experiments.

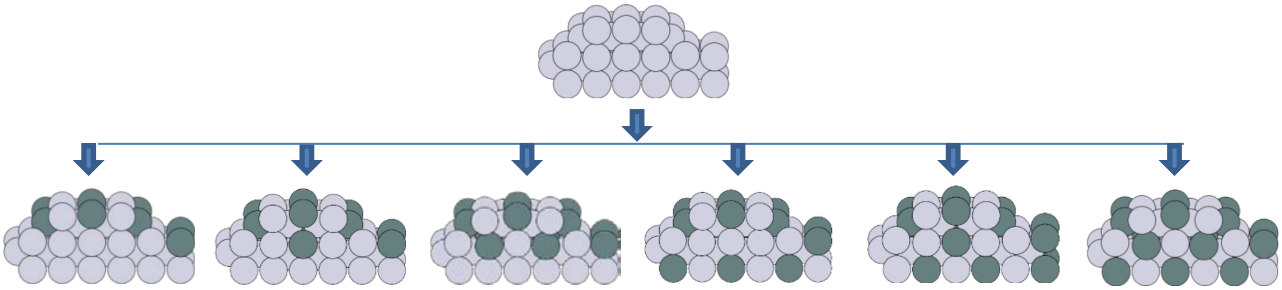

Model 4	Model 7	Model 8	Model 9	Model 10	Model 2
-7.81eV	-8.76eV	-10.05eV	-14.59eV	-14.46eV	-16.98eV*
-6.84eV	-7.56eV	-8.59eV	-12.90eV	-12.52eV	-14.80eV$^{\&}$
-7.81eV	-7.79eV	-8.11eV	-11.68eV	-10.58eV	-12.13eV$^{\wedge}$
-6.84eV	-6.59eV	-6.65eV	-9.99eV	-8.64eV	-9.95eV$^{\%}$

Figure 4-10 Schematic calculation process for formation energies of models for p(6×1) surface

Reference: * Pt_3Sn , $^{\&}$ $Pt_{15}Sn$, $^{\wedge}$ Pt_3Sn+backside effect, $^{\%}$ $Pt_{15}Sn$+backside effect,

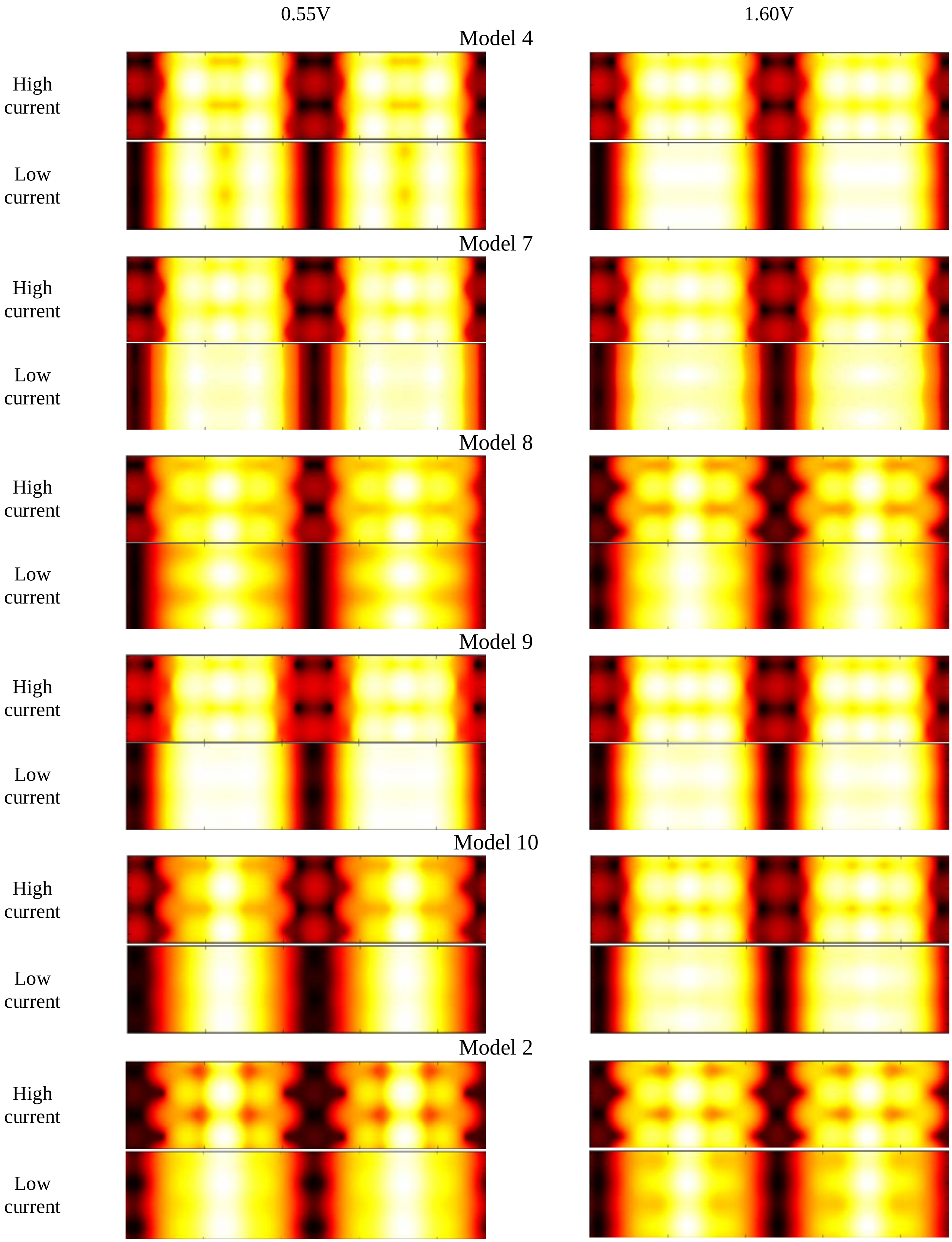

Figure 4-11 Simulated STM images of various p(6×1) models with different currents

The comparison of simulated STM and experimental images are displayed in Figure 4-12 indicating that a reasonable agreement between the simulated STM and experimental results.

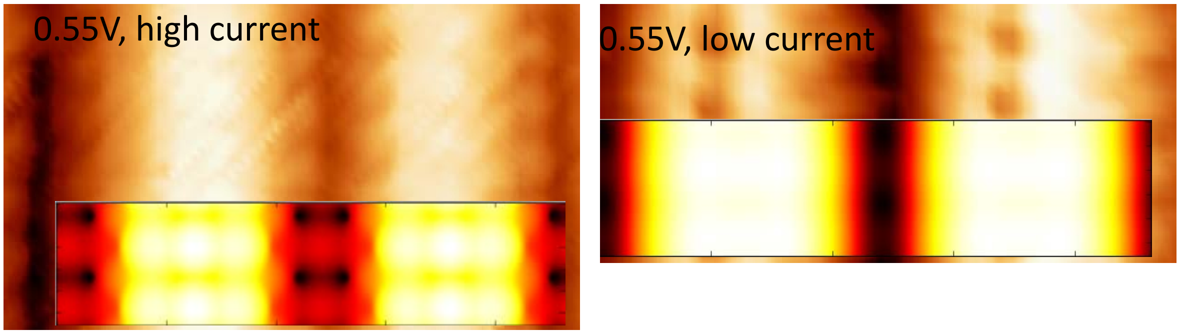

Figure 4-12 Comparison between simulated and experimental STM images of p(6×1) surface

The Sn species assignments are presented in Figure 4-13 .The Sn atoms in position a and a’ (noted as Sn_{ridge}) are in the ridge of the corrugated surface where the tin atoms of surface can exhibit similar electronic state on the surface [1]. And if we compare the Sn atoms in the ridge with the one in the valley between the rows (noted as Sn_{valley}), the former ones can have poorer electronic state than the latter. Hence, the peak at ~23.95eV should be from the ones at postions a and a’, and the peak should be from the Sn at position b. Also, the ratio of peak1/peak2 is about 3 (3.1 at 125eV and 2.5 at 60eV), in reasonable agreement with the atomic ratio of sum of Sn at position a and a’ to the one at position b.

The area of peak at ~24.69eV[1-3] with source at 125eV is much more than the one at 60eV. As the spectra at 60eV is more sensitive with surface Sn, the peaks can be assigned as the Sn from Pt_3Sn(110) bulk, which is noted as c and c’ in the model of Figure 4-13 (b). As the Sn atoms at position c and c’ have very similar chemical environment, the difference of binding energies can not be distinguished by SRPES. Hence, the peak assignation to the Sn at position c and c’ is kindly reasonable.

The model 1 indicate the surface have at least two Sn species on the surface and Sn_{ridge} /Sn_{valley} is 4/1 and one Pt_3Sn species in the bulk, the model therefore is not fit for our surface due to mismatch of Sn_{ridge} /Sn_{valley} . The model 5 exhibits the surface has at least three Sn species on the surface and two Sn in the bulk which can be considered as the same species, indicating its photoemission spectra should be separated into five peaks whose peaks position should be lower than 24eV. However, the spectra can not be fitted with five species with the ratio corresponding to the model 5. So, the model can reasonably agree with SRPES spectra data.

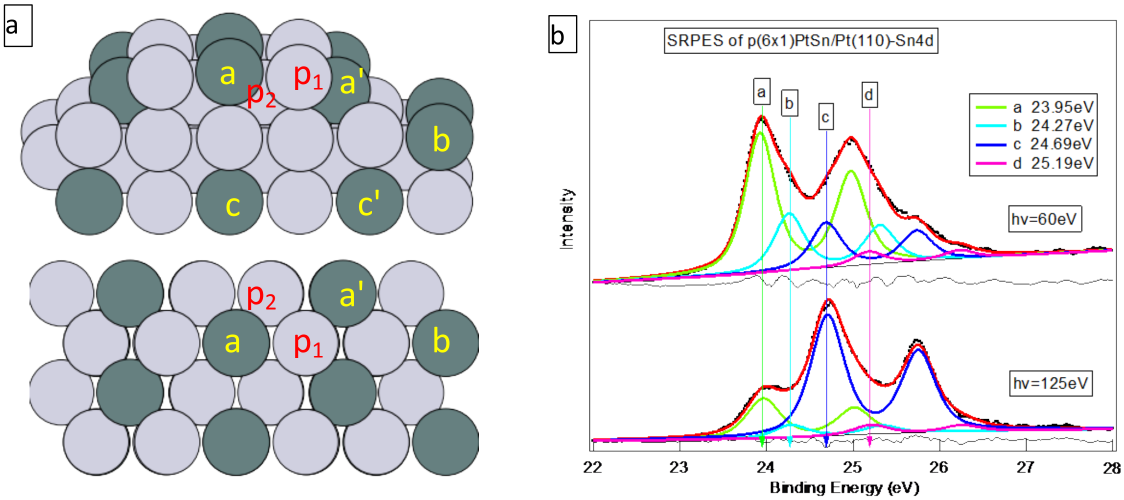

Figure 4-13 Sn species assignments between model and photoemission spectra of p(6×1) surface

4.2 Reactivity

4.2.1 CO adsorption

Thermal programed desorption (TPD) experiments were carried out in a home-built system with the base vacuum at 2×10^{-10} mbar. The system is equipped with quadrupole mass analyzer to record the desorbed gases signal. The sample is mounted on two parallel Ta wires, and can be cooled down to 120 K with liquid nitrogen and heated to about 1300 K. TPD measurements were performed in the UHV after the exposure to different amount of CO at about 120 K. During the TPD experiments, the sample was placed about 5 mm from of the collector tube of the spectrometer, where the emitted species were ionized and filtered by mass and detected. CO TPD results on the two surface alloys and clean (1×2)Pt(110) surface with various CO exposures are displayed in Figure 4-14.

the CO TPD results on p(3×1) surface and p(6×1) surface, are presented in Figure 4-14(a) and (b). The two surfaces exhibit only one obvious desorption peak,, however some smaller intensity features can be observed at the sides of the main desorption peak. For increasing CO exposure, the desorption peak position remains fixed on both surfaces indicating that first-orderkinetics. This behavior is the sane as the CO adsorption on

Pt(110) . Hence according to the method developed by P.A.Redhead [7], the adsorption energy can be calculated by the following equation. [8]..

$$\frac{E_{ad}}{RT_p} = ln\frac{\nu T_p}{\beta} - 3.64. \qquad \text{Equation 4-1}$$

Where E_{ad} is the adsorption energy, which is independent of the heating rate for a first-order rate. R is the ideal gas constant, 8.314 J/(K·mol). T_p is the temperature of desorption peak. β is the heating rate with unit K/s. v is the rate constant, which in general is assumed to be in the range $10^{13} > v/\beta > 10^{8}$.

Assuming $v/\beta = 10^{13} K^{-1}$ like on Pt, then we can obtain the CO adsorption energy on the surface alloys as following.

E_{ad} =111 kJ/mol or 1.16eV/ molecule for the peak at 415 K from p(3×1) surface .

E_{ad} =114kJ/mol or 1.19eV/ molecule for the peak at 425K from p(6×1) surface .

E_{ad} =132kJ/mol or 1.38eV/molecule for Peak α at 490K from pure Pt(110) surface .

Hence the adsorption energies of CO on the surface can be followed the series as $E_{ad\ p(3\times1)} \approx E_{ad\ p(6\times1)} < E_{ad\ Pt(110)}$.

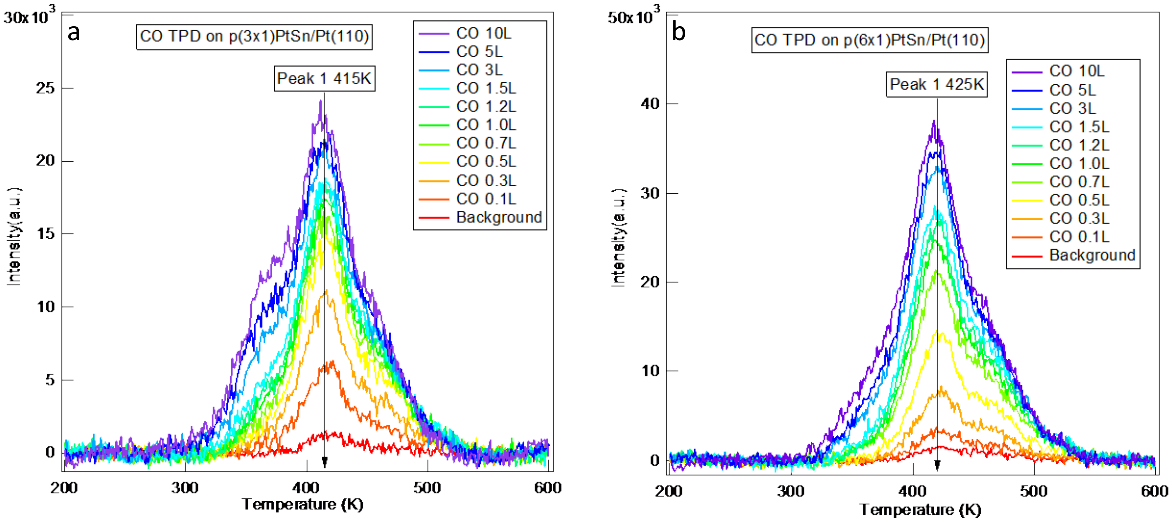

Figure 4-14 CO adsorption on various PtSn/Pt(110) surface alloys : (a) p(3×1) surface and (b) p(6×1) surface

4.2.2 DFT calculations

DFT [9, 10] calculations about CO adsorption on the p(3×1) surface and p(6×1) surface were finished and the results are provided as followed description. It is noted that the preferable adsorption site on pure Pt(110) surface is on top site with adsorption energy at -1.80eV according to our calculation.

Figure 4-15 and Table 4-1 present the results of CO adsorption on the p(3×1) surface, indicating that CO can be adsorbed at O2 site showing in Figure 4-15 with adsorption energy(E_{ad}) at -0.86eV. Another possible adsorbed position is B5 site with E_{ad} = -0.70eV. The O2 site and the B2 site can compete for the CO adsorption, while the E_{ad} at O2 more stable than B2. On the other sites, CO can be desorbed directly or formed an unstable structure. Hence O2 can be preferable adsorption position. According to the DFT results, the CO bond length after adsorption on the surface is 1.169Å (bond length of the CO gas is 1.147 Å) and the bond of Pt-C is 1.876 Å, indicating a strong chemisorption on the surface.

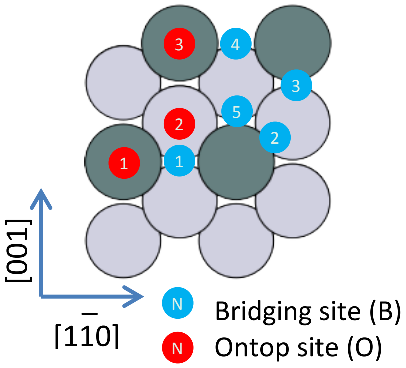

Figure 4-15 Possible CO adsorption sites on p(3x1)PtSn/Pt_3Sn(110)

Table 4-1 Adsorption Energies of CO on the p(3×1) surface

Original position	Final Position	Adsorption Energy(eV)	d(CO) /Å	d(Pt-C) /Å
B1	Unstable			
B2	O2			
B3	O2			
B4	Unstable			
B5	B5	-0.70	1.197	2.071
O1	Desorbed			
O2	O2	-0.86	1.169	1.876
O3	Desorbed			

Figure 4-16 and Table 4-2 present the results of CO adsorption on the p(6×1) surface, showing that CO can be adsorbed on the surface at O2 site with E_{ad} = -1.05eV and B2 sites with E_{ad}.= -0.90eV. The O2 site and the B2 site share the same Pt atoms of the surface; hence a competitive adsorption of CO on the two positions can occur. As CO adsorption on O2 is more stable than the one on B2 site. On the other sites, CO can be desorbed directly or formed an unstable structure. So the O2 site should be the preferable site for CO adsorption. According to the DFT results, the bond length of CO after adsorption on the surface is 1.165Å (bond length of the CO gas is 1.147 Å) and bond length of Pt-C is 1.917 Å, indicating a strong chemisorption

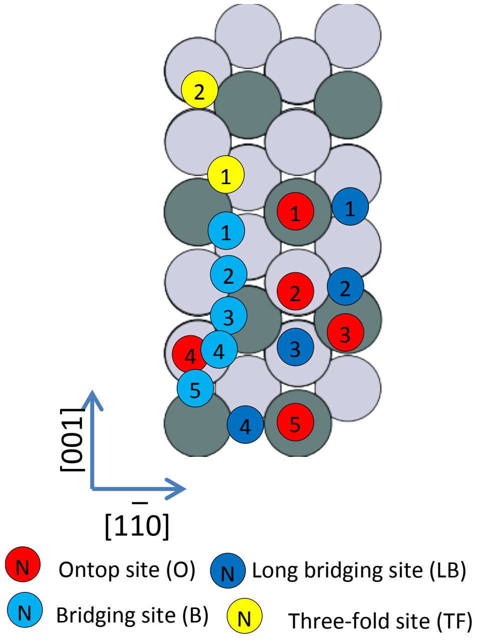

Figure 4-16 Possible CO adsorption sites on p(6x1)PtSn/Pt_3Sn(110)

Table 4-2 Adsorption Energies of CO on the p(6×1) surface

Original position	Final Position	Adsorption Energy(eV)	d(CO) /Å	d(Pt-C) /Å
O1	Desorbed			
O2	O2	-1.05	1.165	1.917
O3	Desorbed			
O4	Unstable			
O5	Desorbed			
B1	B2			
B2	B2	-0.90	1.192	2.012
B3	O2			
B4	O4			
B5	O4			
LB1	B2			
LB2	B2			
LB3	O4			
LB4	Unstable			
TF1	B2			
TF2	O2			

Hence, the two surface alloys can have the similar performance of CO adsorption, which is identified by our experimental data, while the temperature difference between the CO adsorption of the p(3×1) and the p(6×1) surface is about 10K, just a small deviation. Therefore, according to the DFT calculation, the CO adsorption energies on p(3×1) and p(6×1)) are very close. So, the adsorption temperature series can be described as followed: p(3×1) ≈ p(6×1) < Pt(110). And the series is exactly same as our experimental results.

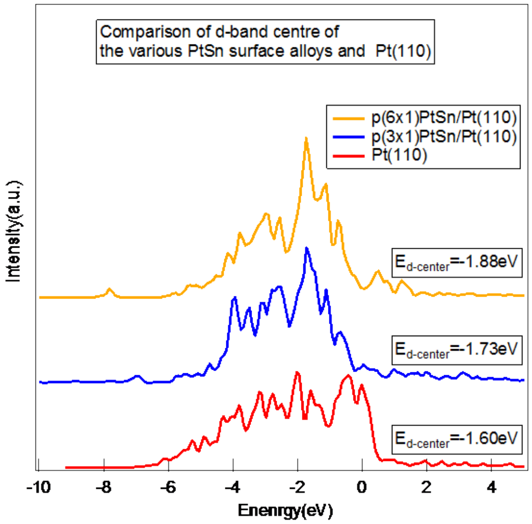

Figure 4-17 Comparison of LDOS of Pt atom of various surface alloys on the topmost layer and the one of Pt(110)

According to d-band center theory by Norskov[11], the value of d-band center is very important for COOR[11], oxidation of methanol or formic acid[12]. Among pure metals, the best one is palladium which has value of d-band center at -1.83eV, while the one of Pt(111) is -2.25eV. According to the DFT calculation of our surface alloy and clean, the value of d-band center of Pt atom on the topmost layer of the surface alloys are -1.73eV, -1.88eV and -1.60eV for p(3×1) surface, p(6×1) surface and Pt(110) surface respectively. According to the value of d-band center, the reactivities of the obtained surface alloys could be probably ranked as: p(6×1) ≈ p(3×1)>Pt(110), which has reasonable agreement with our CO TPD experimental results.

4.3 Conclusion

a. Some STM images at atomic solution of the two surfaces (p(3×1) surface and p(6×1) surface) were obtained and the p(6×1) surface were also additionally characterized with SRPES.
b. Some possible models of the two surfaces were proposed and investigated by DFT calculation. According to their formation energies, the preferable models were selected. Compared with all the proposed models of p(6×1) surface, the bulk has a huge influence on the measured STM images. The model 2 surface therefore can in principle explain the appearance of different measured STM images in different experiments.
c. We simulated by DFT the STM of the two surfaces, confirmed the proposing models, which are also supported by SRPES data.
d. The CO reactivity of two surfaces was investigated, showing that the introduction of Sn can decrease the CO adsorption energy with respect to the pure Pt(110) surface
e. CO adsorption was also investigated with DFT calculations and the adsorption energies series agree quite well with our experimental data.
f. By comparing the d-band center of Pt atoms on the clean and Sn deposited Pt(110) surface we deduce a shift of the centroid of Pt d-band towards higher binding energy, which corresponds to a higher activity for the COOR.

.

References

[1] S. Agnoli, G. Barcaro, A. Barolo, A. Fortunelli, M. Sambi, F. Sedona, M. Di Marino, T. Skala, G. Granozzi, J Phys Chem C, 115 (2011) 14264-14269.
[2] N. Tsud, T. Skala, K. Veltruska, M. Skoda, K.C. Prince, V. Matolin, J Phys-Condens Mat, 23 (2011).
[3] E. Janin, H. von Schenck, S. Hellden, O. Tjernberg, U.O. Karlsson, M. Gothelid, Surf Sci, 515 (2002) 462-470.
[4] P. Depadova, M. Fanfoni, R. Larciprete, M. Mangiantini, S. Priori, P. Perfetti, Surf Sci, 313 (1994) 379-391.
[5] M. Sinner-Hettenbach, N. Barsan, U. Weimar, T. Weiss, H. von Schenck, M. Gothelid, L. Giovanelli, G. Le Lay, Thin Solid Films, 391 (2001) 192-197.
[6] P. De Padova, R. Larciprete, C. Ottaviani, C. Quaresima, P. Perfetti, E. Borsella, C. Astaldi, C. Comicioli, C. Crotti, M. Matteucci, M. Zacchigna, K. Prince, Appl Surf Sci, 104-105 (1996) 349-353.
[7] P.A. Redhead, Vacuum, 12 (1962) 203-211.
[8] P. Waszczuk, G.Q. Lu, A. Wieckowski, C. Lu, C. Rice, R.I. Masel, Electrochim Acta, 47 (2002) 3637-3652.
[9] A. Sumer, M.A. Gulmen, A.E. Aksoylu, Surf Sci, 600 (2006) 2026-2039.
[10] M.A. Gulmen, A. Sumer, A.E. Aksoylu, Surf Sci, 600 (2006) 4909-4921.
[11] A. Ruban, B. Hammer, P. Stoltze, H.L. Skriver, J.K. Nørskov, Journal of Molecular Catalysis A: Chemical, 115 (1997) 421-429.
[12] K. Tedsree, T. Li, S. Jones, C.W.A. Chan, K.M.K. Yu, P.A.J. Bagot, E.A. Marquis, G.D.W. Smith, S.C.E. Tsang, Nat Nanotechnol, 6 (2011) 302-307.

5 Structure and reactivity of SnO_x/Pt(110) nano-oxides

When the surface alloys are exposed to O_2 in the range of 10^{-7} -10^{-5} mbar [1, 2] and annealed at relatively high T (500-800 K), Sn is oxidized and the formation of SnO_x nano-oxides can be observed. The oxidation process was followed by accurate photoemission, and the related results are reported as followed.

5.1 STM and LEED

5.1.1 c(2×4) SnO_x/Pt (110)

If all the three surface alloys are oxidized under nonspecific conditions, a mixture of different nano-oxides is obtained. However, procedures to obtain single and well-ordered phases were optimized. For example, starting from p(6×1) PtSn/Pt(110) and annealing it at P_{O_2}>10^{-6} mbar and T= 723 K (with the following thermal ramp: heated up at 60 K/min, held at 723 K for 5-15 min, and finally cooled down to RT), a c(2×4) SnO_x/Pt(110) LEED pattern is obtained Figure 5-1(a)).

The corresponding STM images are reported in Figure 5-1 (b). In this case, the surface is characterized by large terraces covered by variable amounts of highly corrugated bright spots arranged into c(2×4) chessboard with respect to the substrate, as confirmed by the fast Fourier transform image reported in Figure 5-1(c). By connecting the bright spots, it is possible to identify the c(2×4) primitive unit cell, as highlighted by the blue rhombus reported in the top-right inset of Figure 5-1(b). However, a small fraction of bright spots is characterized by a random registry with the substrate (highlighted with yellow circles). A very similar STM appearance has been previously observed on some SnO_x/Pt(111) [3-8] surfaces and was attributed to the presence of variably interconnected SnO_x species forming ultrathin films with an exotic structure. However, the LEED pattern shown in Figure 5-1(a) is very sharp, indicating that the pattern must be associated to an ordered interfacial layer rather than to the arrangement of the bright spots observed by STM, which in general are coherent only on the short range: the bright spots do not form extended ordered clusters or ordered lines of more than four-five units. As a matter of fact, the top-left inset of Figure 5-1(b) reports the high-resolution image of a region with just few bright spots, which allows imaging the layer underneath. In this case a faintly corrugated motif compatible with a c(2×4) periodicity can be clearly observed. The c(2×4) phase therefore seems to be constituted by a highly ordered low corrugation structure that can be randomly decorated by very bright defects in registry with the substrate. However, they are fascinating because they are mobile even at room temperature and can be accommodated in a quite variable amount on the c(2×4) net (from a few percent up to more than 50%, e.g. in the two different insets of Figure 5-1(b) and Figure 5-1(d), respectively). A high atomic resolved STM image is presented in Figure 5-1(e), indicating that every bright dot is embraced with a cross with victors at $[1\bar{1}1]$ and $[\bar{1}11]$ directions highlighted with red. The ratio of the length along with $[1\bar{1}0]$ direction to the one in [001] direction is a little less than the perfect c(2×4) reconstruction. It can be due to the less thermal drift in [001] direction which is the scanning direction than the one in $[1\bar{1}0]$ direction.

5.1.2 c(4×2) SnOx/Pt (110)

If the oxygen pressure and the annealing temperature are reduced, we obtain a single phase only when starting from the p(4×1) surface alloy (e.g. P_{O_2} 5×10^{-7} mbar at 673 K for 20 min). According to the LEED pattern (Figure 5-2(a)), and STM topography (Figure 5-2(b)), the surface is transformed into a c(4×2) regular pattern with respect to the substrate. A similar c(4×2) SnO_x/Pt(110) reconstruction can be also prepared from Pt_3Sn(110) bulk alloy after adsorption of several thousand Langmuir of O_2 [2]. Our STM images show regularly spaced bright spots, which are analogous to the bright bumps observed in SnO_x/Pt(111) [3-8]. However, fewer missing spots are observed in our case than in the SnO_x/Pt(111) one. The surface cell has an area of 1.12×0.78 nm^2, which corresponds to four unit cells in the $[1\bar{1}0]$ direction and two in the [001] direction. The vectors of the unit cell are highlighted with blue in Figure 5-1(c) and (d). Different domains separated by several zigzag-like boundaries (aligned with the $[\bar{2}21]$ and $[2\bar{2}1]$ directions and highlighted with red lines in Figure 5-2 (b)) can be easily observed. Such line defects are identified as antiphase domain boundaries. These results are consistent with SnO_x nano-oxides grown by oxidation of the Pt_3Sn(110) bulk alloy [2].

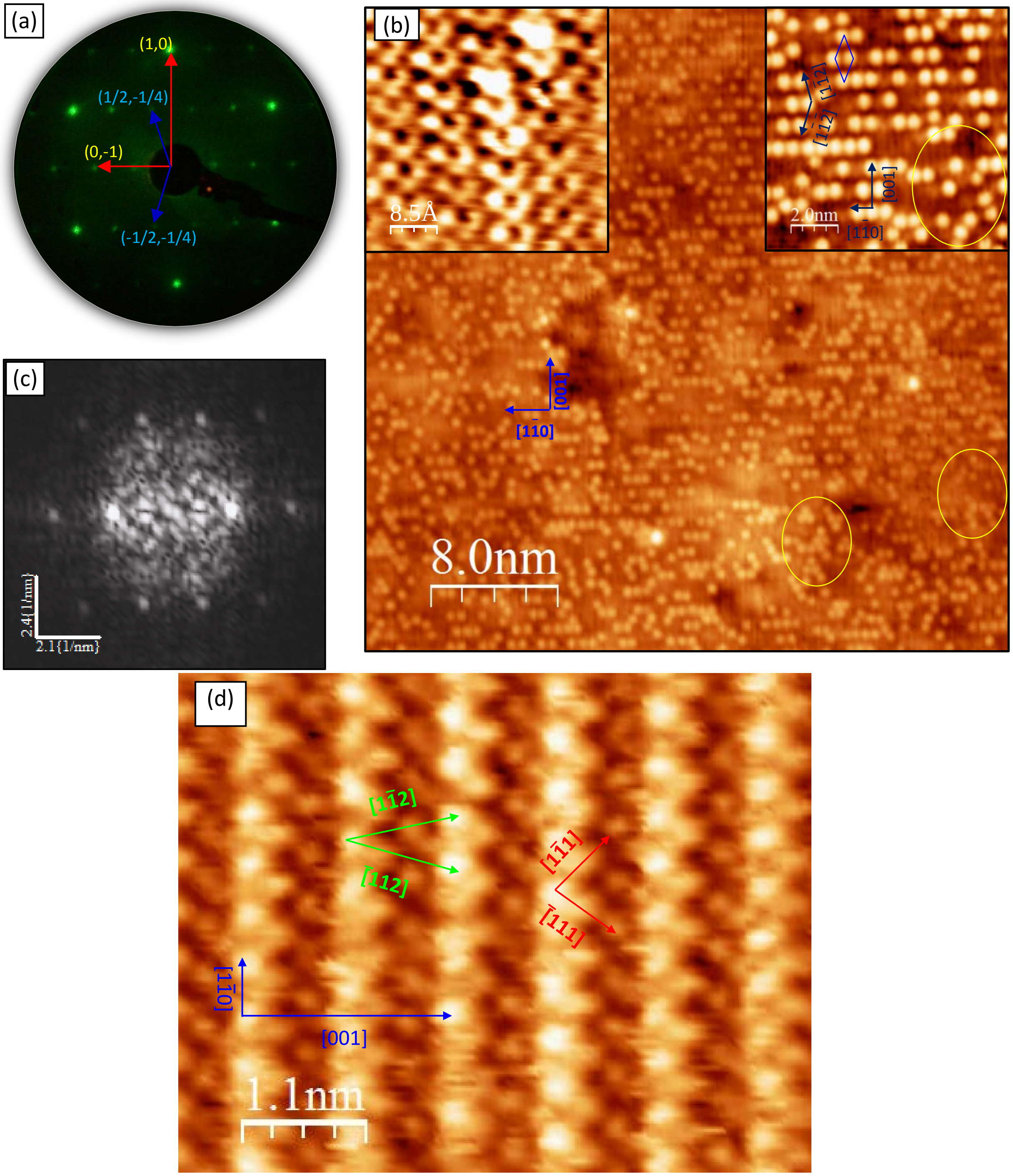

Figure 5-1 c(2×4) SnO$_x$/Pt(110) nano-oxide: (a) LEED pattern at 63eV and (b) STM image, V_t=658mV. The top-left inset shows a zone where the c(2×4) motif is well evident with atomic resolution, V_t= -528mV. The top-right inset shows the c(2×4) motif of the bright spots (see text), V_t=658mV. (c) fast Fourier transform image of the top-right inset in (b), and (d) STM image with high atomic resolution, V_t = -61mV.

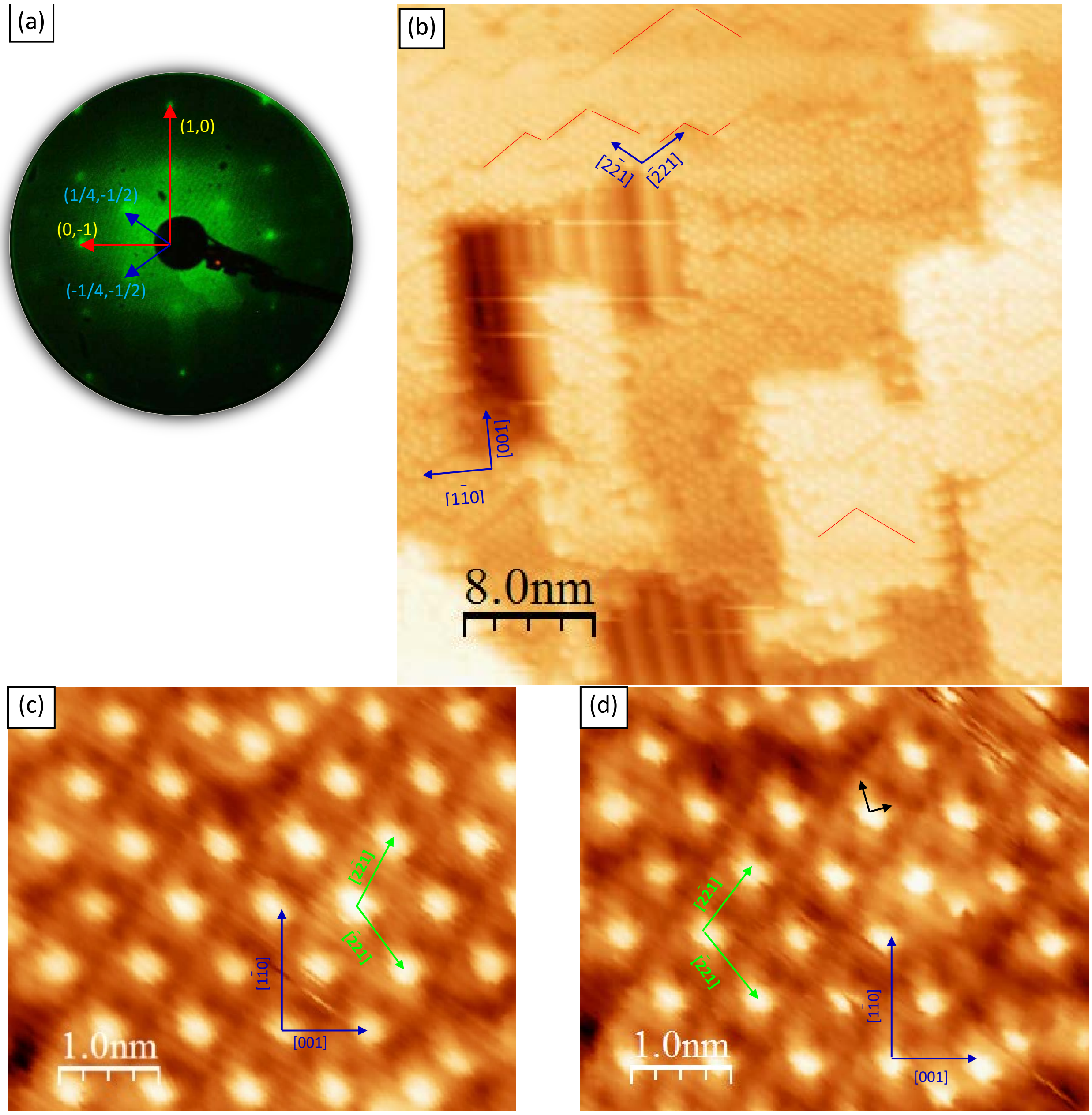

Figure 5-2 c(4×2) SnO_x/Pt(110) nano-oxide: (a)LEED pattern at 63eV, (b) STM image, V_t=1234mV, (The inset image is the atomically resolved topography of the surface alloy oxide, V_t = -34mV), (c) STM image with c(4×2) motif at high atomic resolution, V_t= 55mV and (d) high atomic resolved STM image with c(4×2) motif, V_t= -55mV.

Basing on atomically resolved STM in Figure 5-2 (c) and (d), the images illustrate some defects and dark lines along with $[2\bar{2}1]$ direction, while some dark spots can be observed between bright dots in $[2\bar{2}1]$ direction. The STM images display that every bright spot locates in the center of less bright cross around the dots, while the cross vectors noted as dark arrows in Figure 5-2 (d) are not perfectly along with $[1\bar{1}0]$ or [001] direction.

5.2 SRPES

The two oxides were characterized by SRPES and the spectra are displayed as Figure 5-3, and their fitting data are listed in Table 5-1 The SPRES contains Sn4d (23.5eV ~28eV) and O2s (20eV ~24eV) spectra meaning a little overlap between Sn4d and O2s. The Sn4d photoemissions lines are constituted by a large doublet which can be mainly separated into several different chemically shift doublets. The Sn4d spectrum of c(2×4) oxide is has a peak of higher binding energy than the one of c(4×2) oxide. The O2s lines of c(2×4) oxide is much wider than the one from c(4×2) oxide.

According to the SRPES of O2s and Sn4d of the two oxides, c(2×4) oxide is more oxidized than c(4×2) surface. The 4d photoemission line of c(2×4) surface can be separated into four Sn-related species[9-11]: one component noted as Sn_a at 24.78 eV which can be corresponding to the Sn in Pt_3Sn, a peak at 25.66eV noted as Sn_b ascribed to Sn(II), the last two components at 26.19 eV and 26.96eV noted as Sn_c are connected to Sn(IV) and Sn(IV)-OH species, respectively. The presence of hydroxyls species can be induced by the reaction of c(2×4) surface with residual water in the UHV environment.

The O2s photoemission line of c(2×4) surface can be fitted by three O-related species: component O_a as O-Sn at 20.31eV, component O_b connected O-Sn-O at 21.64 eV, and H_2O_{ad} or –OH at 23.14 eV (see Figure 5-4). The ratio between the peak areas of Sn(IV) species to Sn(II) species is about 0.4, whereas the ratio of O-Sn-O/O-Sn is about 1.7. The Sn(IV) should be related with O-Sn-O, while the Sn(II) can be corresponding to O-Sn. So, the surface should has species SnO_4 and SnO with a ratio SnO_4/SnO=1/2

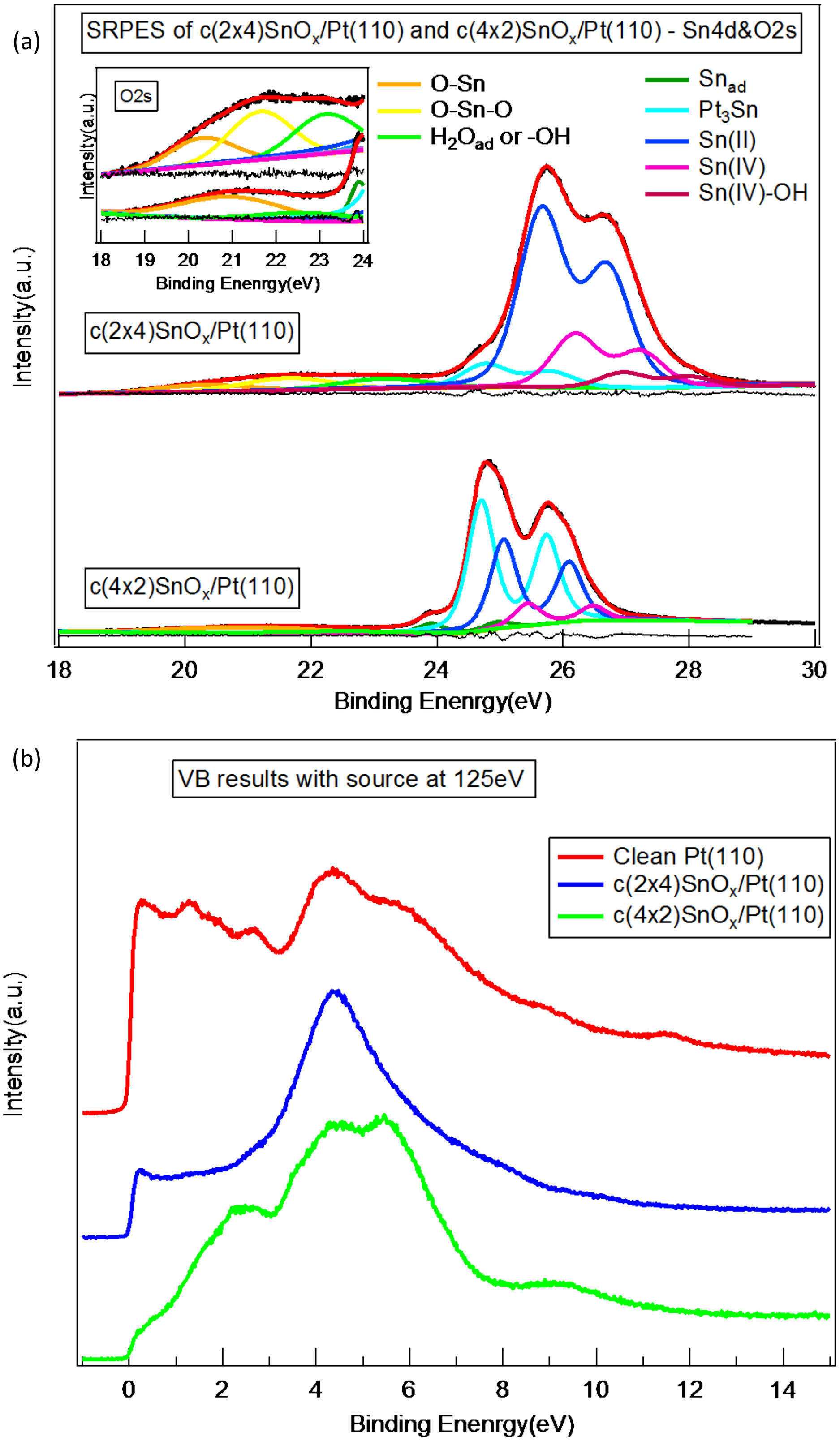

Figure 5-3. SRPES of c(2×4)SnO_x/Pt(110) and c(4×2)SnO_x/Pt(110) surface oxides: (a) Sn4d and O2s and (b) comparison of valence band (VB) of various surfaces

Table 5-1 Fitting data of the two oxides

<table>
<tr><th colspan="6">c(2×4)SnO_x/Pt(110)</th></tr>
<tr><th>Sn4d</th><th>Position(eV)</th><th>Peak area</th><th>O2s</th><th>Position(eV)</th><th>Peak area</th></tr>
<tr><td>Sn-Pt</td><td>24.78</td><td>15287</td><td>Sn-O</td><td>20.31</td><td>5001</td></tr>
<tr><td>Sn(II)</td><td>25.66</td><td>117684</td><td>O-Sn-O</td><td>21.64</td><td>8781</td></tr>
<tr><td>Sn(IV)</td><td>26.19</td><td>35882</td><td>H_2O_{ad} or -OH</td><td>23.14</td><td>7244</td></tr>
<tr><td>Sn(IV)-OH</td><td>26.96</td><td>10238</td><td></td><td></td><td></td></tr>
<tr><th colspan="6">c(4×2)SnO_x/Pt(110)</th></tr>
<tr><th>Sn4d</th><th>Position(eV)</th><th>Peak area</th><th>O2s</th><th>Position(eV)</th><th>Peak area</th></tr>
<tr><td>Sn-Sn</td><td>23.89</td><td>4420</td><td>SnO_x</td><td>20.98</td><td>6842</td></tr>
<tr><td>Sn-Pt</td><td>24.70</td><td>56379</td><td>H_2O_{ad} or -OH</td><td>22.75</td><td>2693</td></tr>
<tr><td>Quasi-Sn(II)</td><td>25.05</td><td>37991</td><td></td><td></td><td></td></tr>
<tr><td>Sn(II)</td><td>25.43</td><td>9498</td><td></td><td></td><td></td></tr>
</table>

The spectrum of c(4×2) surface can be separated into four distinct peaks, connected to Sn atoms in different structural environment[9-11]. The peak at 23.89eV assigned as little metallic Sn_{ad} or the Sn on the surface not oxidized; the peak at 24.70eV, a value close to the BE of Sn in Pt_3Sn can be associated of the “bulk species” noted as $Sn_{a,}$. The component at 25.43eV fits the expected value for Sn(II) noted as Sn_c species, whereas the peak at 25.05eV noted as Sn_b should represent quasi Sn(II) species due to the media value between the ones attributed by Sn(II) and Sn(ad). Similarly the O2s peak can be fit by two components: component O_a from O-Sn at 20.98 eV, and a second peak at 22.75eV due to adsorbed H_2O_{ad} or –OH. The ratio of Sn(II)/quasi-Sn(II) corresponding to Sn_c/Sn_b is 0.25, while the O-related species can be mainly attributed to O-Sn from O_a. Hence, the surface should constitute of SnO_4 & SnO while the O is the interlock between the two Sn species.

VB spectra of the two surface oxides surfaces presented in Figure 5-3, (b) indicate that the pure Pt(110) has a complex structure of the Pt 5d band [9], consisting of peak at about 4.5 eV and some highly intense features around the Fermi level. The VB of c(2×4) surface with a broad peak centered at 4.5 eV and a medium intensity around Fermi level ; while the one of c(4×2) surface has four peaks: 2.4eV, 4.5eV, 5.5eV and 9.2eV, and very low value around Fermi level. The peak at 4.5eV obtained from c(2×4) surface is probably caused by the bulk Pt or Pt_3Sn(110) Pt_3Sn(110) exhibiting the c(2×4) surface has a thin SnO_x layer. And the intensity around Fermi energy level of the surface illustrates the layer. The spectrum of c(4×2) surface has a four wide peaks including the peak at 4.5eV probably from Pt_3Sn bulk, and peaks centered at 2.4eV, 5.5eV, 9.2eV which are probable from SnO whose VB typically has three peaks at about 3eV, 6.5eV and 9.7eV respectively. [12-15]. Hence c(4×2) surface has kindly thicker SnO_x covered on the Pt surface than c(2×4) surface, which agree with comparison between models of the two oxides.

5.3 Models

According to STM images of the oxides, some models were proposed and investigated by DFT calculations.

5.3.1 c(2×4) SnO_x/Pt (110)

According to the SRPES results discussed previously, the surface constitutes of SnO_4 and SnO clusters with their SnO_4/SnO component ratio at 0.5. The models are proposed and investigated by DFT calculation, and their structures and simulated STM images are as displayed in Figure 5-4 . The model 1, 2 and 3 assume SnO_4 clusters whose components are labeled as Sn_c and O_b on the topmost layer. The third layer has a SnO with half-layer and its components are indicated as Sn_b and O_a, whereas the bulk can have pure Pt or PtSn alloys which contains the Sn_a component. The three models are constructed such that they share the same topmost layer termination and differ only for the Sn amount and distribution in the Pt bulk. Model 4 also has a SnO_4 clusters on the topmost layer, and a full SnO_x in the second layer. In the third layer, a full PtO_x is configured, while the substrate consists of pure Pt bulk. The proposed models were simulated by DFT calculations, and are displayed in Figure 5-4.

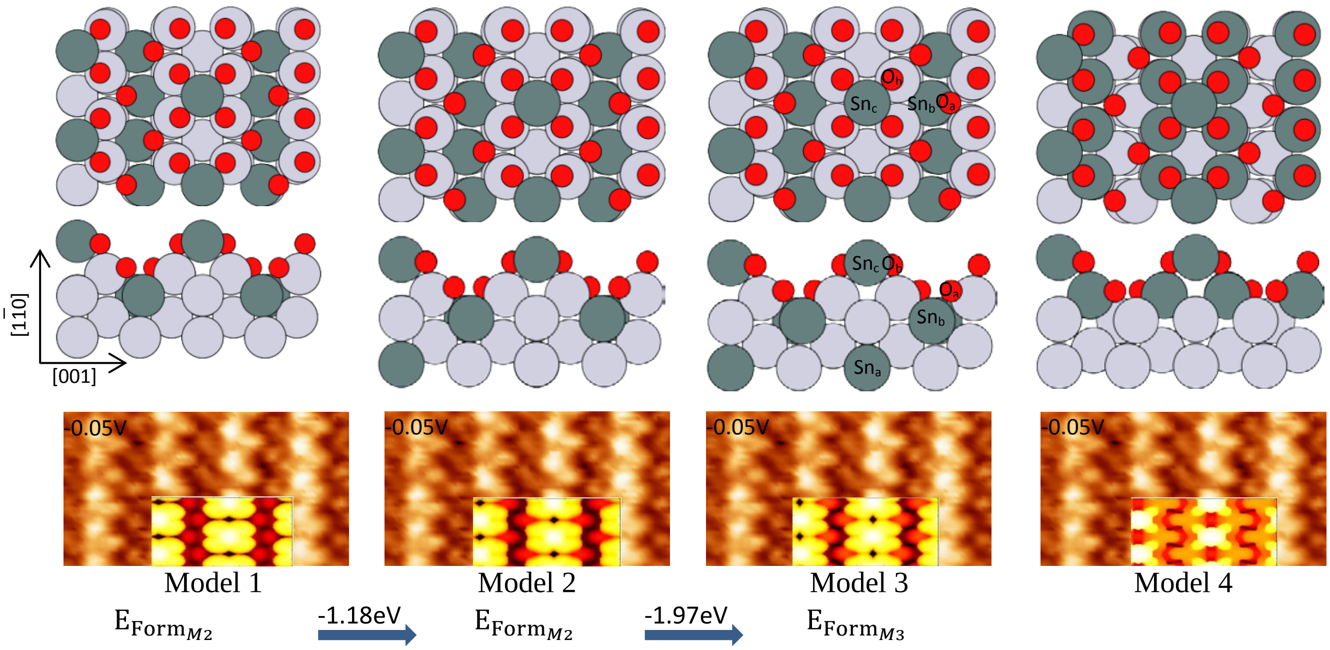

Figure 5-4 Atomic models of c(2×4) surface and their corresponding simulated STM images.

The simulated STM images show some flower-like structure corresponding to the SnO_4 cluster and a “zigzag-like” structure in the space between the “flowers”, which stems from the O_a in the SnO of the third layer. The model 4 shows some crosses on the topmost layer, while the contrast is not consistent with the experimental STM image. Hence, according to the comparison of experimental data and simulated images, model 1, 2, and 3 could match experimental STM images. According to DFT calculations, STM topographies of the oxide are not so sensitive to the bulk composition. So, the formation energies among the models should be considered. Using the method explained in chapter 2 the formation energy for the different phases is also reported in Figure 5-4 .

According to the comparison of the formation energies among the models, the Model 3 owing the lowest formation energy should be the preferable one. It can be noted that there is a clear preference for the system to go towards Sn rich conditions. From the experimental point of view, this uptake of Sn is ruled by the actual availability of Sn on the surface and therefore by the amount of Sn deposited. The model obtained by DFT optimization is made up by a SnO_4 unit and two SnO species therefore well in agreement with the values obtained by the analysis of the photoemission data ($Sn^{IV}/Sn^{II}=0.5$ O-Sn^{IV}/O-$Sn^{II}=2$). Hence, the model 3 can match the surface well.

5.3.2 c(4×2) SnO_x/Pt (110)

The proposed models of c(4×2) surface are presented in Figure 5-5 . The model 1 and model 2 were supposed the surface has a completed SnO_x topmost layer (i.e. No Pt is exposed), The two models have the same stoichiometry of components, while their oxygen sites on the topmost layer have different orientations showing in Figure 5-5. For the two models, outer Sn and Oxygen atoms are named as Sn_c and O_a, respectively. The second layer comprises a pure Sn layer, whose atoms are arranged in group of four that are slightly tilted with respect to the main crystallographic directions of the substrate. The third layer is the interface between Sn_b layers and bulk composing with Pt_3Sn and is made up by Sn and Pt atoms arranged in a slightly distorted fcc lattice. The model 3 has the same surface structure as the model 1 and model 2 while the model 3 has a pure Pt interfacial layer between the SnO_x layer and Pt_3Sn(110) bulk. The model 4 has a SnO_4 on cluster on the topmost layer, while the second layer is composited of PtO_x which share the oxygen atoms with the SnO_x. The interfacial layer is a PtSn layer between PtO_x layer and bulk having a component of Pt_3Sn(110). The models were investigated by DFT calculations providing also the simulation of the STM images. Comparing the simulated STM images with experimental data (see Figure 5-5), the simulated STM images of model 1 can nicely reproduce the bright spots and slight dark troughs along with $[2\bar{2}1]$ well indicating that model 1can match the surface well. The simulated STM image of model 2 and model 4 can also reproduce the bright spots and the dark trough, but the dark trough direction can not match our experimental results. The model 3, according to its simulated STM image can not match experimental STM images due to no reproduction of dark troughs. Besides, the comparison between experimental and simulated STM images of model 1 with bias at 50mV and -50mV displayed in Figure 5-6(d) and (e), indicating high accordance of the model. The ratio of Sn_c/Sn_b= 0.25, and the O atoms on the topmost layer are shared by the two Sn-species, which means a quite good agreement with our photoemission data. Therefore, mode1 can match the surface very well.

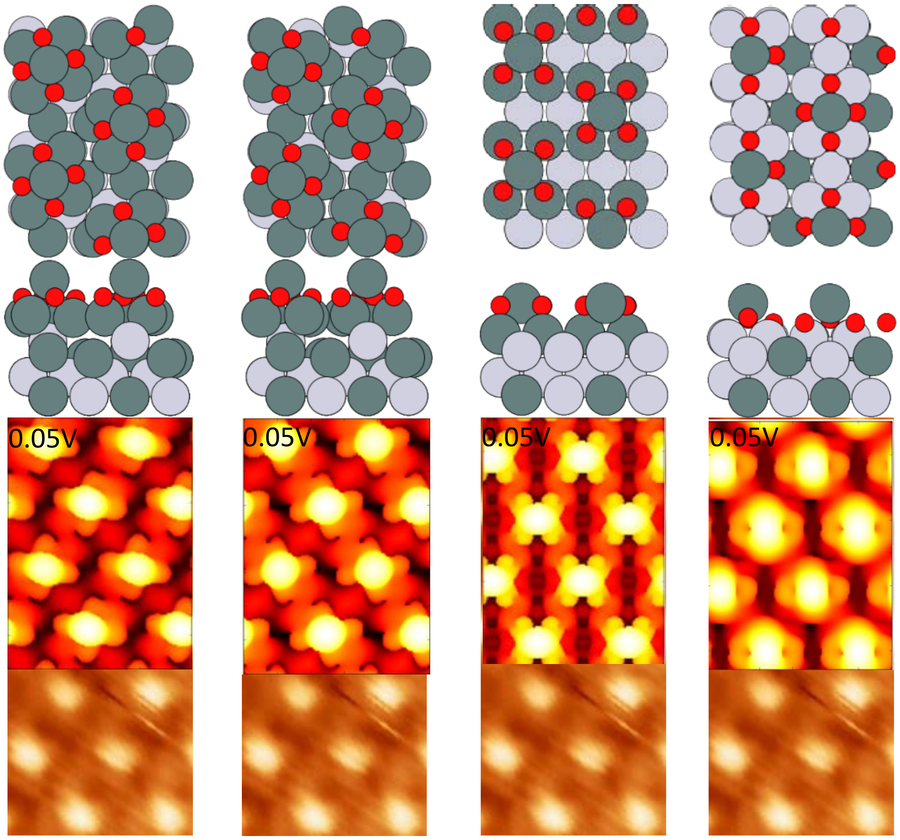

Model 1 Model 2 Model 3 Model 4

Figure 5-5 Atomic models of c(4×2) surface and their corresponding simulated STM images.

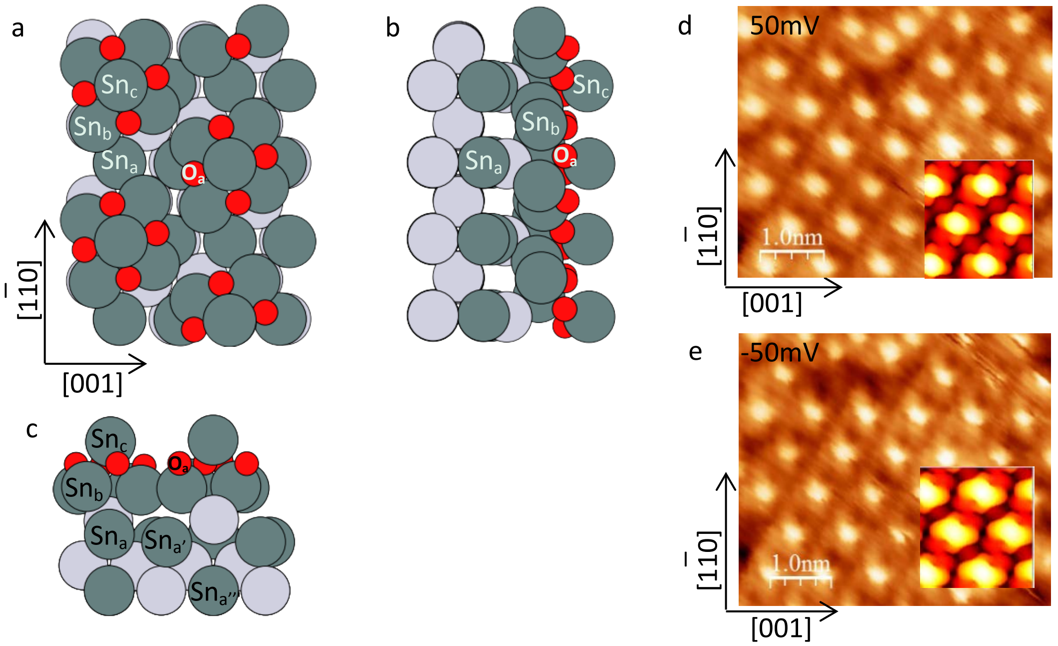

Figure 5-6 Atomic models of c(4×2) surface-M1: (a) top view, (b) front view and (c) side view, and comparisons between simulated STM and experimental results with different bias: (d) 50mVand (e) -50mV.

5.4 Reactivities

The reactivity of the two oxides was tested using small molecules such as CO and methanol, and their results are discussed in the following paragraphs.

5.4.1 CO adsorption

CO was employed as the probe to test the performance for the two surface oxides and oxidized Pt(110) surface. Firstly, the surfaces were prepared with isotopic labeled oxygen,$^{18}O_2$, and then the samples were checked by LEED and then cooled down to 150 K to complete the TPD tests. The reactivity towards CO was investigated experimentally and theoretically by DFT calculations.

5.4.1.1 TPD results

The TPD experimental results are presented in Figure 5-7. Figure 5-7(a) shows the CO signal (m/z=28) on various surfaces including the c(2×4), the clean and oxidized Pt(110) surface. According to the spectra, for the clean Pt(110) surface, the CO shows two desorption peaks: peak 0 at 405 K and peak 4 at 495 K, which are identified with saturated CO adsorption on reconstructed Pt(110) reported in the previous papers [16-19]. After pre-dosing dosing $^{18}O_2$ 3L at 723K, the sample was exposed cyclically to CO at 3L CO per cycle. In the first cycle, a peak at 490K is recorded from the oxidized Pt(110) surface. Then, starting from the 2nd cycle, the position of desorption peak does not change, whereas the area is higher than the one in first cycle and is maintained constant in the 2nd and 3rd cycle. From the comparison with the CO on the oxygen pre-exposed and clean Pt(110), the active adsorbed surface area is reduced into about one half of the one on the clean Pt(110) surface. It can be explained as the oxidation of Pt on the surface by pre-adsorbed oxygen during the TPD measurements. The oxidation will block some active adsorption sites and it then cause the decrease of CO adsorption.

When the CO was exposed on the c(2×4) surface, no clear CO desorption peaks can be observed from the surface. But, starting from the 2nd cycle, a CO peak at 485 K is observed, whose area increases with the gas exposure to saturate at the 4th cycle. In the 3rd and 4th cycle, two more peaks become visible, peak 1 at 425 K and peak 2 at 450K as reported in Figure 5-7(a), indicating that two new active sites for CO adsorption are formed during the desorption experiments procedure.

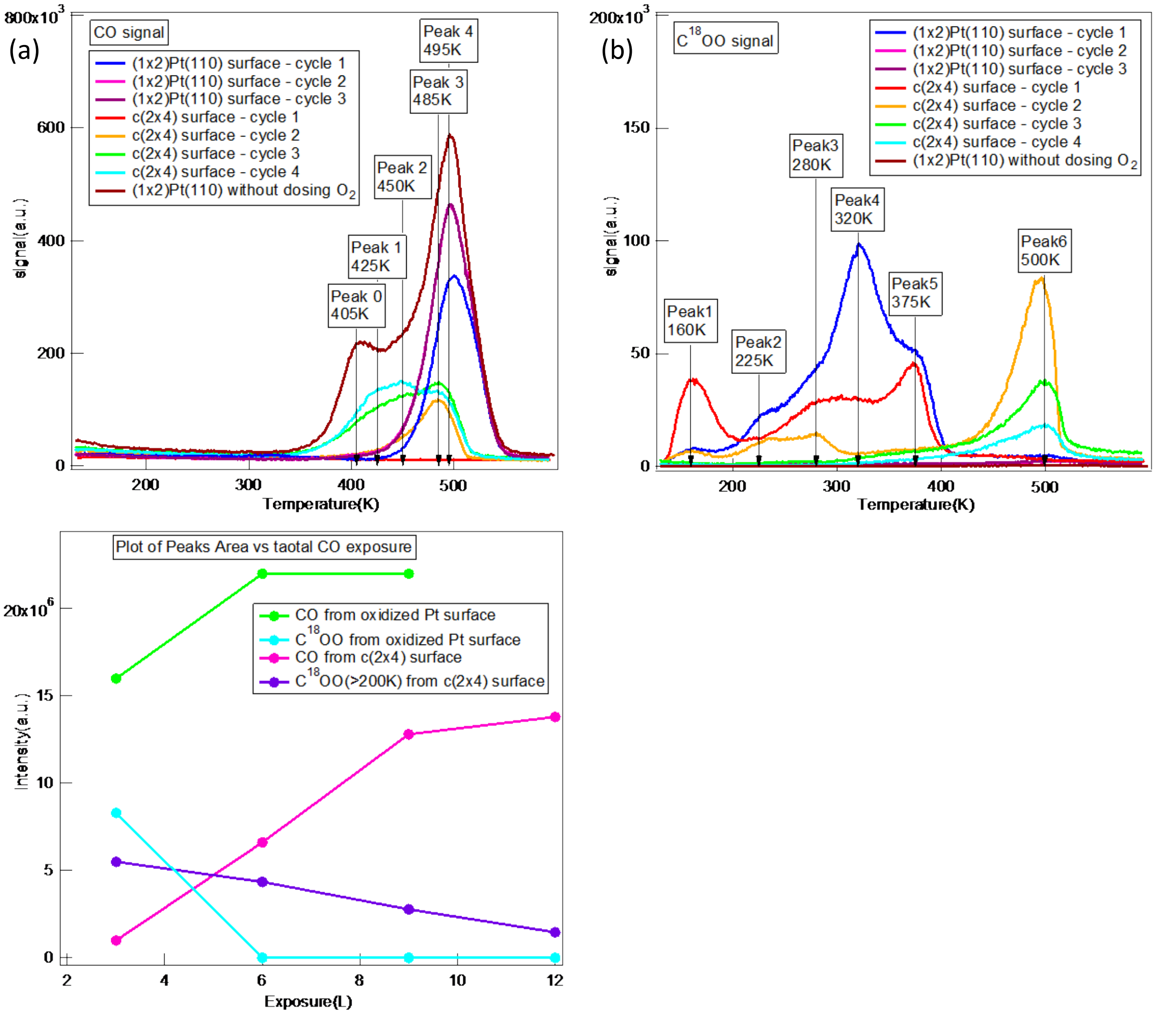

Figure 5-7 CO adsorption on c(2×4)SnO_x/Pt(110) nano-oxides and (1×2)Pt(110) surface pre-dosed with O_2: (a) CO with signal at m/z =28, (b) $C^{18}OO$ at m/z =46 and (c) plot of peaks area vs total dosed CO amount

Figure 5-7(b) reports the desorption spectra monitoring m/z=46 corresponding to $C^{18}OO$ from the different surfaces after cyclic CO exposure. on the oxidized Pt(110) surface, four peaks including peak 2 at 225K , peak 3 at 280K, peak 4 at 320K and peak 5 at 375K can be observed., the peak at 320 K being the most intense one. All these peaks can be assigned to products of CO oxidation from different reconstructed oxidized Pt(110) surface[20-24]. And after the 1st cycle, no $C^{18}OO$ evolves from the Pt(110) surface probably due to the depletion of oxygen from the surface.

On the c(2×4) surface, at least three peaks can be observed in the $C^{18}OO$ desorption spectrum: peak 1 at 160 K, the wide peak 3 at 280 K and peak 5 at 375 K. Peak 1 is always attributed from physically adsorbed $C^{18}OO$, however the peak from the 1st cycle is very huge. Hence, it could be caused by desorption of products from reaction of adsorbed CO with active ^{18}O on the surface. Peak 3 and 5 can be also observed from oxidized Pt(110) surface in our experiments, so the c(2×4) surface should has certain part PtO_x surface which has active sites for CO transformation into $C^{18}OO$. Starting from the 2nd cycle, the peak 5 disappears, and the peak 2 and peak 3 reduces comparing with the 1st cycle; moreover, a new peak, labeled as 6, can be observed at 500 K. In the following CO exposure cycles, the peaks below 400 K quickly decrease in intensity and almost disappears whereas peak 6 even if decreasing remain very intense.,

By comparing Pt(110) and c(2×4) spectra we can deduce that the CO can be converted to CO_2 following two distinct path. There is one direct high temperature channel that implies just the c(2×4) phase where the CO is adsorbed, reacts with the oxygen of the c(2×4) phase and is readily desorbed, originating the desorption peak at 500 K.

An alternative lower temperature path involves the co-presence of c(2×4) and Pt. This can be deduced by the co-presence of the same desorption peaks (2, 3 and 5) on Pt and on the surface oxide. However, the presence of the surface oxide determines an increase in the activity as a function of time. Actually while the activity conversion of CO is lost after the first cycle on the Pt(110) surface because all oxygen is consumed. On the c(2×4) the low temperature desorption peaks are observed also in the 2nd and 3rd cycles. This indicates that the c(2×4) surface can act as an oxygen reservoir (spillover effect) for the Pt areas where the actual conversion of CO takes place. Increasing the cycles this channel disappears probably because a Sn metal area is produced around SnO_x islands preventing therefore the interaction with Pt.

If we plot the areas of the CO and $C^{18}OO$ desorption peaks versus total CO exposure reported in Figure 5-7(c), it become apparent that on Pt in absence of O_2 pre-exposure no oxidation occurs and just CO desorption, whereas in presence of O_2, CO_2 is efficiently produced until oxygen is consumed. On the c(2×4) surface the production of CO_2 is more steady indicating that the c(2×4) surface as higher durability than the Pt(110) surface.

If we compare the sum of all the CO_2 peaks area from the c(2×4) surface with the one from oxygen pre-exposed Pt(110) surface, the c(2×4) transforms more than 50% of CO to CO_2 .

CO is also used to test reactivity of the c(4×2) surface, however, no clear CO or CO_2 can be observed from the surface.

5.4.1.2 DFT calculations

The reactivity of two oxide surfaces towards CO was investigated by DF theory. A summary of the results is presented in Figure 5-8 & Table 5-2 for the c(2×4) surface , and Figure 5-9 &Table 5-3 for the c(4×2) surface, respectively.

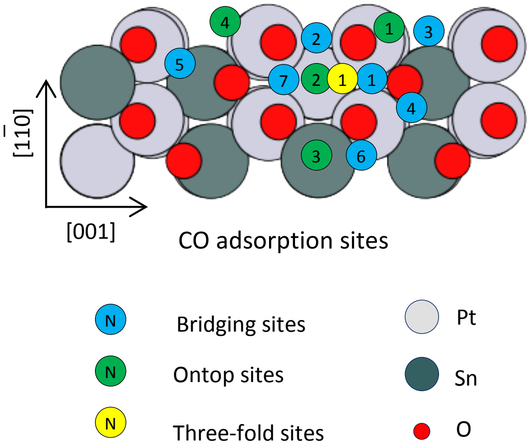

Figure 5-8 DFT results of CO adsorption on c(2×4)SnO_x/Pt(110) surface

Table 5-2 Adsorption Energies of CO on the c(2×4)SnO_x/Pt(110) surface-M3

Original position	Final position	Product	Energy
B1	Desorbed	CO_2	-2.91
B2	B2	CO	5.01
B3	Unstable		-1.53
B4	Desorbed	CO_2	-0.73
B5	B5	CO	2.53
B6	Desorbed	CO_2	-1.69
B7	Unstable		0.75
O1	Desorbed	CO_2	-1.69
O2	B2	CO	5.01
O3	Desorbed	CO	--
O4	Desorbed	CO	--
TF1	TF1	CO	4.73

On the c(2×4) surface, a CO molecule was added to the surface to calculate reactivity on all the possible adsorption sites by calculating their corresponding adsorption energies. According to the results reported in Table 5-2, on the surface, there are two active sites that are able to adsorb CO and then oxidize the CO to CO_2. This reaction can produce CO_2 with 1.7 eV energy emitted on O1 site whereas this reaction can reach 2.9 eV on B1 site (see Figure 5-8). The active barriers are always less than 1.0eV [20, 23-25]. On oxidized Pt(110) surface, the barriers is about 0.4 eV via Langmuir-Hinshelwood mechanism, or about 0.7 eV through Eley-Rideal mechanism[22]. On the PtO_x(110)/Pt(110) (12×2) reconstruction, the barriers is only 0.3eV[22]. And on α-PtO_2(0001), the barrier is 1.9eV which is pretty high, however the value is still lower than the one giving out from the oxidation on B1 site. So, it is possible oxidize CO on the c(2×4) surface. Hence, according to the DFT results, the surface can oxidize CO efficiently, which is in agreement with our TPD results.

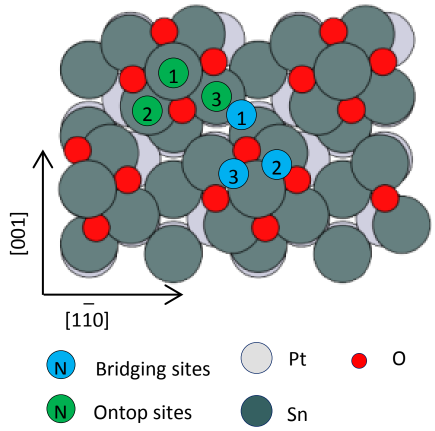

Figure 5-9 DFT results of CO adsorption on c(4×2)SnO_x/Pt(110) surface

Table 5-3 Adsorption Energies of CO on c(4×2)SnO_x/Pt(110) surface

Original position	Final position	Product	Energy
B1	Desorbed	CO	--
B2	Desorbed	CO	--
B3	Desorbed	CO	--
O1	Desorbed	CO	--
O2	Desorbed	CO	--
O3	Desorbed	CO	--

According to the adsorption sites showed in data presented in Figure 5-9 and Table 5-3, no CO can be adsorbed on the c(4×2) surface, due to its complete coverage by $SnO_{x.}$ Hence, it can match our experimental results. And the conclusion obtained from DFT calculations also support our conclusion about the role of Pt-related species in oxidation of CO in SnO_x/Pt(110) system.

5.4.2 Methanol decomposition

The two oxide surfaces were investigated using methanol as probe molecule.

In the case of the c(2×4) a marked reactivity was observed. As a matter of fact as already reported in chapter 3, by dosing methanol on the c(2×4) structure at moderate temperature it is possible to induce a phase transition to the p(6×1). Obviously, this indicates a redox reaction where the methanol reduces the surface oxide and leaves on the surface metal Sn alloyed with Pt. We tried to get a better insight into this surface reaction by carrying out TPD experiments. In particular we exposed the c(2×4) structure to 3L methanol at low temperature and performed a linear ramp to 600 K to observe the desorption spectra. Then we cycled this same procedure for several times.

Differently from the c(2×4), the c(4×2) resulted to be scarcely reactive towards methanol. Methanol is adsorbed at low temperature and it is molecularly desorbed around 200 K.

No other byproducts were observed (e.g. CO, H_2 CO_2 C H_2O ect), therefore the corresponding TPD will not be discussed in the present thesis.

5.4.2.1 *TPD results from c(2×4) surface dosed with 3 L CH_3OD per cycle*

To better understand the reactivity of the c(2×4) surface and to gauge the results, the clean (1×2)Pt(110) was employed as internal reference. The corresponding TPD results with 1 L methanol exposure are reported in Figure 5-10.

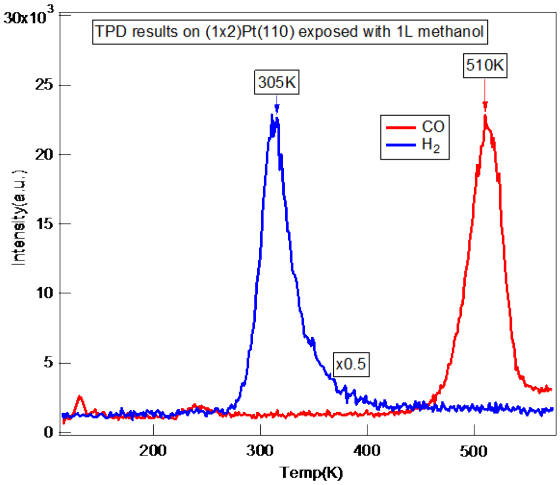

Figure 5-10 TPD results of methanol decomposition on clean (1×2)Pt(110) surface after dosing 1L methanol

According to the desorption curves, the Pt surface can decompose methanol completely into CO and H_2 whose ratio of the two peaks area (CO/H_2) is about 1:2. The desorption temperature of the CO and H_2 peaks are 510 K and 305 K respectively, which perfectly agrees with literature data [26, 27]. This points to a very high activity of the surface that can clearly decompose methanol below room temperature, interestingly no other byproducts like CO_2, water, or formaldehyde were observed.

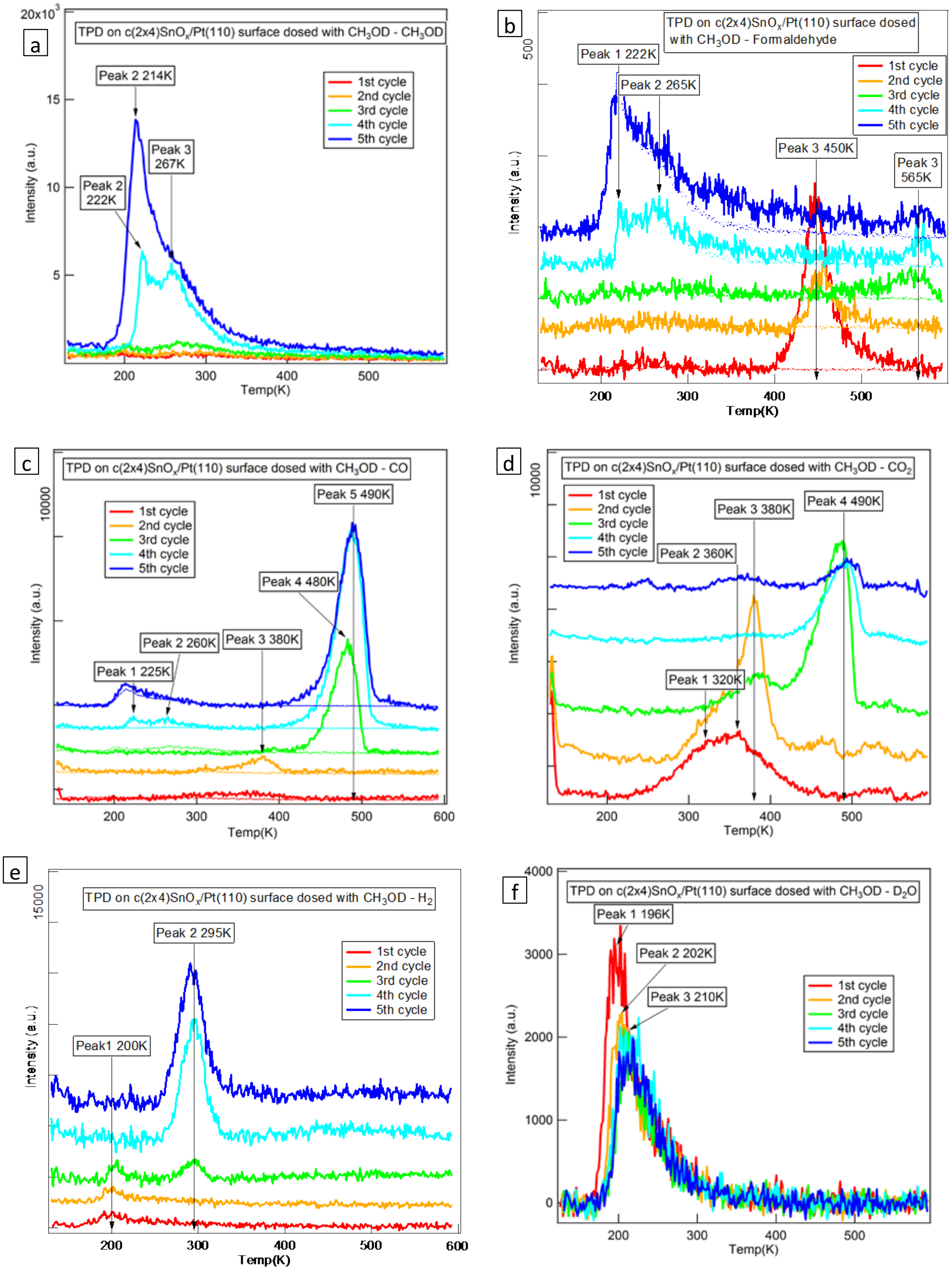
a
TPD on c(2x4)SnOx/Pt(110) surface dosed with CH3OD - CH3OD
20x10³
15
10
5
Intensity (a.u.)
Peak 2 214K
Peak 3 267K
Peak 2 222K
1st cycle
2nd cycle
3rd cycle
4th cycle
5th cycle
200
300
400
500
Temp(K)
b
TPD on c(2x4)SnOx/Pt(110) surface dosed with CH3OD - Formaldehyde
500
Intensity (a.u.)
Peak 1 222K
Peak 2 265K
Peak 3 450K
Peak 3 565K
1st cycle
2nd cycle
3rd cycle
4th cycle
5th cycle
200
300
400
500
Temp(K)
c
TPD on c(2x4)SnOx/Pt(110) surface dosed with CH3OD - CO
10000
Intensity (a.u.)
1st cycle
2nd cycle
3rd cycle
4th cycle
5th cycle
Peak 5 490K
Peak 4 480K
Peak 2 260K
Peak 3 380K
Peak 1 225K
200
300
400
500
600
Temp(K)
d
TPD on c(2x4)SnOx/Pt(110) surface dosed with CH3OD - CO2
10000
Intensity (a.u.)
1st cycle
2nd cycle
3rd cycle
4th cycle
5th cycle
Peak 3 380K
Peak 4 490K
Peak 2 360K
Peak 1 320K
200
300
400
500
Temp(K)
e
TPD on c(2x4)SnOx/Pt(110) surface dosed with CH3OD - H2
15000
Intensity (a.u.)
Peak 2 295K
Peak1 200K
1st cycle
2nd cycle
3rd cycle
4th cycle
5th cycle
200
300
400
500
600
Temp(K)
f
TPD on c(2x4)SnOx/Pt(110) surface dosed with CH3OD - D2O
4000
3000
2000
1000
0
Intensity (a.u.)
Peak 1 196K
Peak 2 202K
Peak 3 210K
1st cycle
2nd cycle
3rd cycle
4th cycle
5th cycle
200
300
400
500
Temp(K)

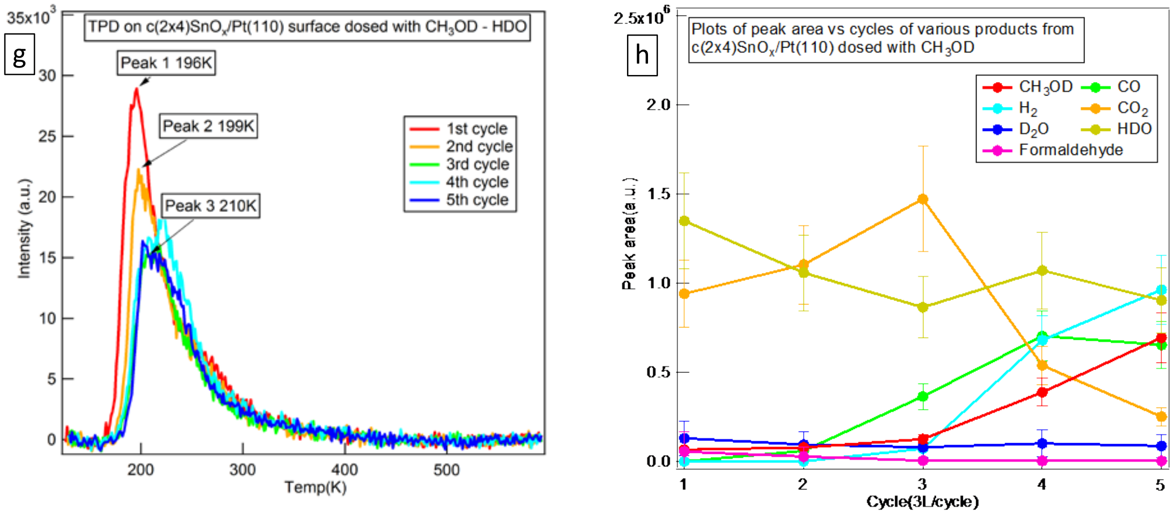

Figure 5-11 Cyclic TPD results from c(2×4)SnO$_x$/Pt(110) surface dosed with 3L/cycle CH$_3$OD

Figure 5-11 presents a set of TPD experiments where the exposure to CH$_3$OD at low temperature (120 K) and desorption ramp up to 600 K were cycled several times.

The reiteration of the dosing procedure allows monitoring the effect of an increasing reduction of the oxide towards the reaction path of methanol. Actually, methanol is a reducing species whose decomposition removes oxygen from the surface. Our data will show that on passing from a fully oxidized surface to a reduced one (and eventually PtSn surface alloy) methanol undergoes a notable change in the decomposition products.

In order to get a complete view of the different products that can be formed during methanol decomposition we acquired the mass signal corresponding to methanol, formaldehyde, CO, CO$_2$, H$_2$, D$_2$O, HDO.

The results show that from 1st cycle to 3rd cycle, no distinct CH$_3$OD can be observed, meaning that the oxidized surface can catalyze methanol decomposition completely in the quite efficiently. In the 4th cycle, two desorption peaks: peak 2 at 222 K and peak 3 at 267 K were observed from the surface, which indicates that some CH$_3$OD molecules are simply molecularly desorbed from surface, without undergoing any reaction. This is a first indication that the surface oxide is quite reactive, whereas as the phase gets more and more reduced also its reactivity strongly decreases. In the 4th and 5th cycle, the curve contains two peaks, peak 1 at ~214 K, and peak 2 at 267 K. Comparing with the 4th cycle, the TPD desorption peak area in 5th cycle is higher than the one in the 4th cycle, meaning that more CH_3OD is desorbed from the surface, without be involved in a chemical reaction.

Figure 5-11(b) reports one of the products (m/e=30), formaldehyde (CH_2O), obtained from the oxidized surface. During the first two cycles, a peak at 450 K, peak 3, is observed and the peak area decreases in the following cycles. In the 3rd cycle, the peak at 450 K cannot be detected, while a new weak peak at 565 K, peak 4 appears. In the subsequent exposure, the peak 4 remains roughly constant, but in the 4th and 5th cycle, two intense low temperature peaks, peak 1at 220K and peak 2 at 265K, can be seen, but are simply due to the cracking pattern of CH_3OD which are plotted with dotted curves in the figure, therefore not connected to the surface reactivity.

In Figure 5-11(c), we report the desorption spectrum of m/z=28, which corresponds to CO and in dotted lines the background signal coming from the cracking pattern of CH_3OD. The data indicate that no CO desorption peak can be observed during the first exposure, whereas one weak peak at 380K - peak 4- can be observed in the 2nd cycles. An intense desorption peak at about 490K - peaks 4 - can be observed starting from the 3rd cycle. The desorption temperature slightly shifts and undergoes a huge intensity increase. It has to be noted that peak 4 shows a desorption temperature very similar to the CO desorption temperature from Pt(110) (495 K) and also to the desorption of CO coming from the decomposition of methanol (510 K). This seems to indicate that starting from the 3rd exposure the surface oxide is heavily reduced and some Pt patches are formed.

The mass signal coming from CO_2 (m/z=44) is reported in Figure 5-11(d). In the 1st cycle, two desorption peaks can be distinguished: peak 1 at 320 K and peak 2 360K. An evolution of the desorption spectrum can be observed already at the second exposure: the peak 1 disappears, the peak 2 becomes weak, and a new peak - peak 3 - at 380 K can be observed From the 3rd cycle to the 5th cycle, the peak 3 decreases and another new peak-peak 4 - at 490 K is obtained. The intensity of peak 4 decreases from the 3rd to 5th cycle.

The behavior of the surface is therefore quite complicated, however we can discern a pattern: at high level of oxidation (first cycle) the total conversion of methanol to CO_2 is quite effective at low temperature (peak 1, 2, 3), however as the oxygen availability is progressively reduced a new reaction channels opens at higher temperature (peak at 490 K). This latter peak seems to have a similar behavior to the CO_2 desorption peak observed on the oxygen pre-dosed Pt(110) surface, suggesting once again the hypothesis that after an induction period during which the oxide is reduced, Pt metal patches are formed and on these areas methanol can be decomposed.

The desorption spectra of hydrogen were recorded as well (m/z=2, Figure 5-11(e)). According to the spectra, no clear peaks can be observed from the surface in the first two cycles but only starting for the 3rd exposure to methanol. This peak at 295 K remains constant in position and slightly increases in intensity from the 3rd to 4th cycle, then remain constant. The peak lies in a temperature range very similar to the desorption temperature of H2 from Pt(110) as a consequence of methanol decomposition

Since we used deuterated methanol, various water species including HDO (m/z=19) and D_2O (m/z=20) were recorded. The results are showed in Figure 5-11(f), and Figure 5-11(g) respectively. The spectra of two species have the same desorption peaks at about 200 K, and undergo small changes as a function of the number of the exposure cycles. From the results of HDO and D_2O, the signal of HDO is stronger than D_2O. The data therefore do not allow an easy disentanglement of the reaction pathway followed by methanol probably because of the adsorption of H_2O from the background atmosphere, which prevents a clear identification of the H or D atoms coming from the formation of methoxy species or from oxidative dehydrogenation of methanol to formaldehyde, respectively.

To summarize the surface reactivity we have reported in one plot the trend of products observed by mass spectroscopy as a function of the exposure cycles, and the results are showed as Figure 5-11(h). According to the plot, during the first two cycles, three species can be clearly observed: CO_2, methanol and formaldehyde; hence the reactions of the two cycles can be concluded as Equation 5-1 and Equation 5-2. The CO amount is far more than CH_2O, so the latter one should be related with decomposition products from the surface defect or boundary.

$$\boldsymbol{CH_3OD + PtSn - O \rightarrow CO_2 + HDO} \qquad \text{Equation 5-1}$$

$$\boldsymbol{CH_3OD + PtSn - O \rightarrow CH_2O + PtSn - OH} \qquad \text{Equation 5-2}$$

With increasing cycles to the 3rd cycle, also CO and H_2 can be observed probably coming from the interaction with Pt or PtSn reduced areas:

$$\boldsymbol{CH_3OD + PtSn \rightarrow CO + 2HDO} \qquad \text{Equation 5-3}$$

When exposure reaches the 4th cycle, a relevant amount of CH_3OD is molecularly desorbed from the surface. It can be deduced that the surface becomes less reactive with methanol decomposition. Also the fraction of methanol that undergoes total oxidation to CO strongly reduces whereas the signal from CO and H_2 strongly increases. Then the reaction can be described as Equation 5-4.

$$\boldsymbol{CH_3OD + PtSn - O_{red} \rightarrow HDO + CO + H_2 + CO_2} \qquad \text{Equation 5-4}$$

At the 5th TPD cycle, the peak area of CO_2 decreases dramatically, while the one of H_2 increases and becomes one of major products. Besides the signals of CO and HDO is almost the same as the one in the 4th cycle. Therefore, the main reaction in this cycle can be summarized as Equation 5-5.

$$\boldsymbol{CH_3OD + PtSn - O_{red} \rightarrow HDO + CO + H_2} \qquad \text{Equation 5-5}$$

Finally, to corroborate the hypothesis of the formation of clean Pt and PtSn alloys patches we mention that the after the set of TPD experiments we observed a strong weakening of the of the LEED pattern of the c(2×4) structure and at the same time we observe the formation of the pattern pertainig to the p(6×1).

5.4.2.2 SRPES and LEED

SRPES was also used to characterize the interaction between methanol and the surface oxide: Sn3d, O1s, C1s and Pt4f signals were acquired on the clean surface, after 5.0 L methanol exposure and after desorption to 600K. The SRPES spectra are showed in Figure 5-12 (a), (b), (c) and (d). C1s was also recorded during the desorption of methanol in snapshot mode (selecting the binding rang and acquiring the signal in real time through the MCP detector) and the resulting spectra were plotted as a matrix (Figure 5-13(a)). Moreover, in Figure 5-13(b) we report the line profiles corresponding to C1s peaks at 6 increasing temperatures ($T_0 – T_5$), and their deconvolution. Finally, the evolution of each C 1s peak component as a function of temperature is shown in Figure 5-13(c).

According to the Sn3d spectra,(Figure 5-12(a)), the signal can be separated into five peaks[8, 28, 29]:

i) ~484.68 eV assigned to Sn ad-islands on the surface, noted as Sn_{ad}

ii) ~485.65 eV assigned to Pt_3Sn in the bulk, noted as Sn_{alloy}

iii) ~486.45 eV assigned to Sn^{2+} species,

iv) ~487.30 eV assigned to Sn^{4+} species

v) ~488.20 eV assigned to SnO_2-OH

The Sn^{4+}/Sn^{2+} components ratio evaluated by the Sn 3d peak deconvolution of the clean (original) surface is about 0.26 (comparing to the 0.5 value predicted by the model), indicating that the present of some defects.

The same ratio, evaluated after 5L methanol dosing is about 0.34. These two values can be considered constant as the 0.26 to 0.34 deviation can be made on the Sn3d deconvolution. Therefore, we can conclude that surface does not change after the methanol exposure. Moreover, the spectrum of the surface dosed with 5.0L methanol shows a weak peak at ~488.25 eV, which can be assigned to SnO_2 adsorbed with hydroxyl. After methanol desorption, the Sn^{4+}/Sn^{2+} ratio decreases to about 0.14, much lower than ~0.3 value reported above, in agreement with a further reduction of the surface oxide. .

Furthermore, we compared the Sn^{2+}/Pt-Sn among the three spectra: a value of about 0.7, 0.8 and 1.3 were found for the clean surface, after 5.0L methanol dosing and after desorption respectively. The first two value can be considered constant it is clear that the Sn^{2+} species increased after desorption due to an increase of Sn^{2+} (as demonstrated before by Sn^{4+}/Sn^{2+} ratio), thus to the SnO_x reduction. The peaks area of Sn_{ad} peaks and SnO_2-OH are very little; and can be assigned to some defects on the surface. By comparing the results of Sn^{4+}/Sn^{2+} and Sn^{2+}/Pt-Sn ratios, we can conclude that after reaction with methanol, Sn^{4+} surface species are reduced into Sn^{2+} and some Sn diffusion from the surface to the bulk occurs during the heating process.

Based on the O1s signal deconvolution (Figure 5-12-b), the spectrum of the pristine surface contains three O-related species [8, 30]:

i) SnO at 529.95 eV

ii) SnO_2 at 530.90eV

iii) –OH at 531.90 eV.

The SnO_2/SnO peaks components ratio result to 0.37, which is a lower than the computed ratio of 0.52 and in quite good agreement with the ~0.3 values obtained from Sn3d deconvolution. As discussed above, this is tune with presence of surface defects. When the surface is exposed with 5.0L methanol, the O 1s spectrum becomes more complex and can be separated into several components.

-the components i), ii) and iii) assigned to SnO, SnO_2 and -OH species, were still present, although the -OH peak maximum negatively shifts to 531.67eV

iv) 532.55eV, assigned to methanol (CO, $-OCH_3$ or CH_xO species)[31, 32];

v) 533.40eV assigned to adsorbed water;

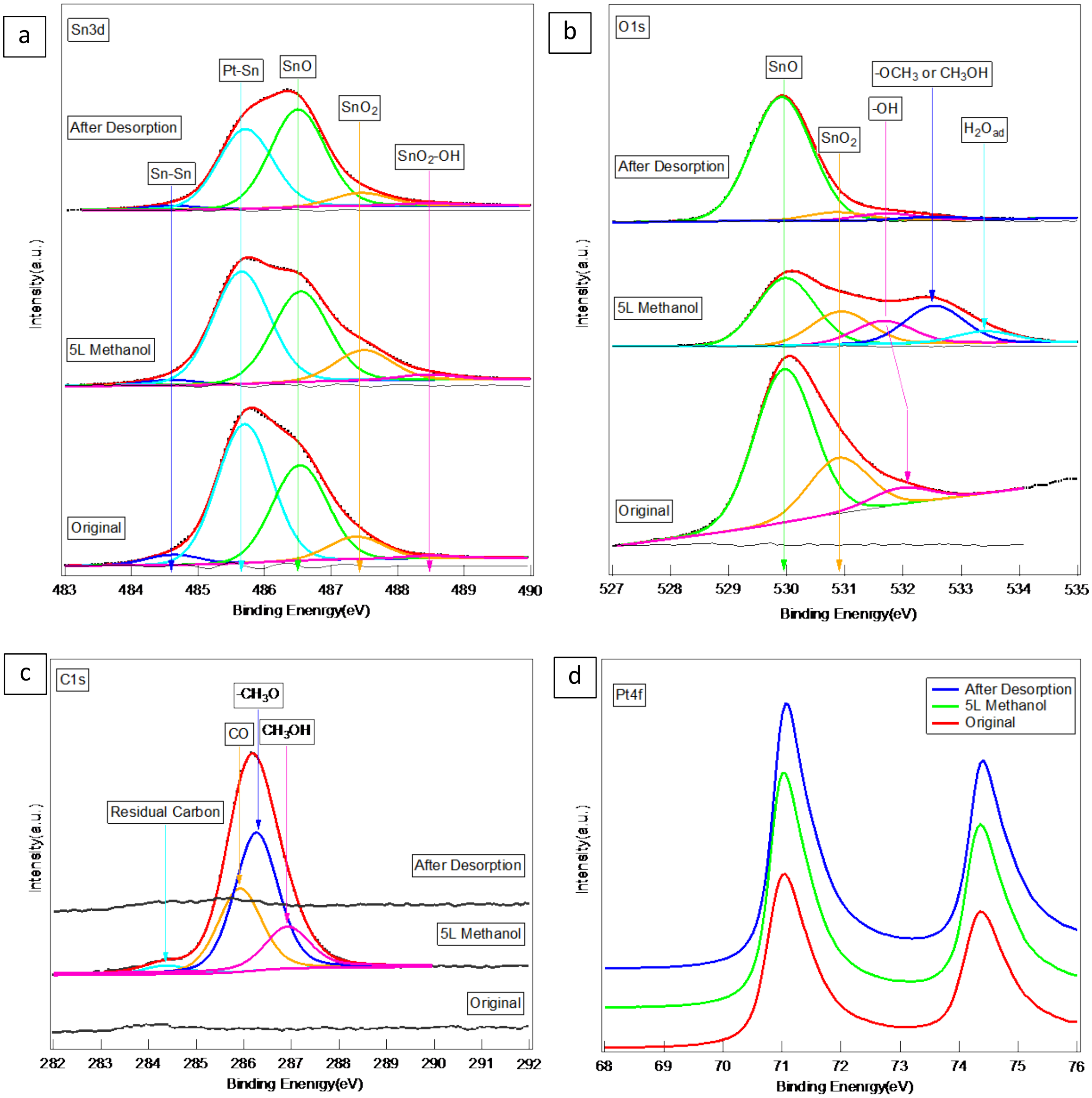

Figure 5-12 In-situ SRPES results during reactions of 5L CH_3OH during heating $c(2\times4)SnO_x$/Pt(110): (a) Sn3d results, (b) O1s signal, (c) C1s, and (d) Pt 4f,

After methanol desorption, the two peaks related with methanol and adsorbed water are almost disappeared. The SnO_2 peak area decreases probable due to the oxidation film reduction in agreement with the Sn3d results discussed above. A small peak at ~531.67eV is still present and shows no shift compared to the one collected on the surface dosed with methanol; this it can be assigned to hydroxyl.

Also small intensity peak at 532.20eV can be observed and could be due to adsorbed species (either methanol or products from methanol decomposition). .

Figure 5-12(c) reports the C1s spectra of the original surface, the surface with after 5L methanol dosing and after desorption. According to the results, no carbon- related species can be observed on the original surface. After 5L methanol exposure, a broad C1s spectrum was observed. Based on the deconvolution results, the spectrum can be separated into 4 components[33]:

i) ~284.30eV, assigned to elemental carbon,

ii) ~285.86eV, assigned to CO,

iii) ~286.26eV, assigned to methoxy ($-OCH_3$) group,

iv) ~286.91eV, assigned to methanol.

According to spectra, no related C1s signal can be detected, while little formaldehyde can be observed from the surface. It can be explained as the little amount of formaldehyde on the surface comparing with other species, so the photoemission signal of formaldehyde cannot be distinguished. After the methanol desorption, no distinguished C1s peaks can be observed. The results match the O1s peak analysis.

Figure 5-12(d) shows the Pt4f spectra unchanged both after the methanol exposure and the desorption

In-situ SRPES test was finished during the TPD procedure which is reported as Figure 5-13(a) and some of their fitting results were showing as Figure 5-13(b). According to the C1s matrix (Figure 5-13(a)) and the C1s deconvolution (line profiles T_0-T_5 , Figure 5-13(b)) four species can be singled at T_0 [34]: ~284.30eV, ~285.86eV, ~286.26eV, and ~286.91eV, which are assigned as residual carbon, $-OCH_3$, and methanol respectively.(in agreement with the spectrum reported in Figure 5-12(c), - i~iv peaks) The same components are also present at T_1 and T2. When the sample temperature increases to T_3, the peak iv) corresponding to molecular methanol disappears. This indicates the methanol is either desorbed or decomposed from the surface. When the temperature reaches T_4, only one peak centered at 295.9eV, assigned to adsorbed CO, can be observed. However, at this temperature, no CO can be observed from TPD spectra, but clearCO_2 desorption peaks develops (see Figure 5-13(d).). Therefore, we can conclude that the surface is able to oxidize the methanol to CO, then to CO_2 due to plentiful O atoms on the topmost surface. When the temperature reaches T_5, the spectrum shows no distinguished peak meaning that no carbon-related species can be detected.

In Figure 5-13(c), we report that the C 1s peak components evolution as a function of the temperature in the T_0-T_5 range. Based on the plot, at T_0 the surface is mainly covered by -CH_3O Resulting from the dissociative adsorption of CH_3OH. When the temperature reaches T_1, the amount of CH_3OH and –CH_3O decreases.

This can be explained by:

i) molecular desorption of CH_3OH,

ii) recombination of -CH_3O and –OH groups to yield CH_3OH (recombinative desorption),

iii) -CH_3O decomposition (oxidation to CO) [33],

The CO component area increases, doe to a probable decomposition of methoxy into CO (reaction path iii). This reaction path (methanol total oxidation to CO_2) is supported by presence of labeled water (HDO) desorption peak, showing in Figure 5-13(d). HDO is formed from the recombination of –OH and –OD groups that are formed upon CH_3OH dissociation and -CH_3O decomposition.

When the temperature reaches T_3, CH_3OH can no more be detected while the signal of –CH_3O decrease dramatically and the CO shows a little variation. T_3, can be considered the temperature at which CO desorption starts. At T_4, CO is the only species detected on the surface, even though its intensity decreases with respect to the maximum. This result is in good agreement with TPD which shows that CO_2 is the last desorption product. (see Figure 5-13(d)). As CO_2 cannot be adsorbed on the surface, the CO_2 can be the products of oxidized CO on the surface. Basing on the photoemission peak area, about one half part of adsorbed CO can be oxidized into CO_2 by the O of the surface from T_3 to T_4.

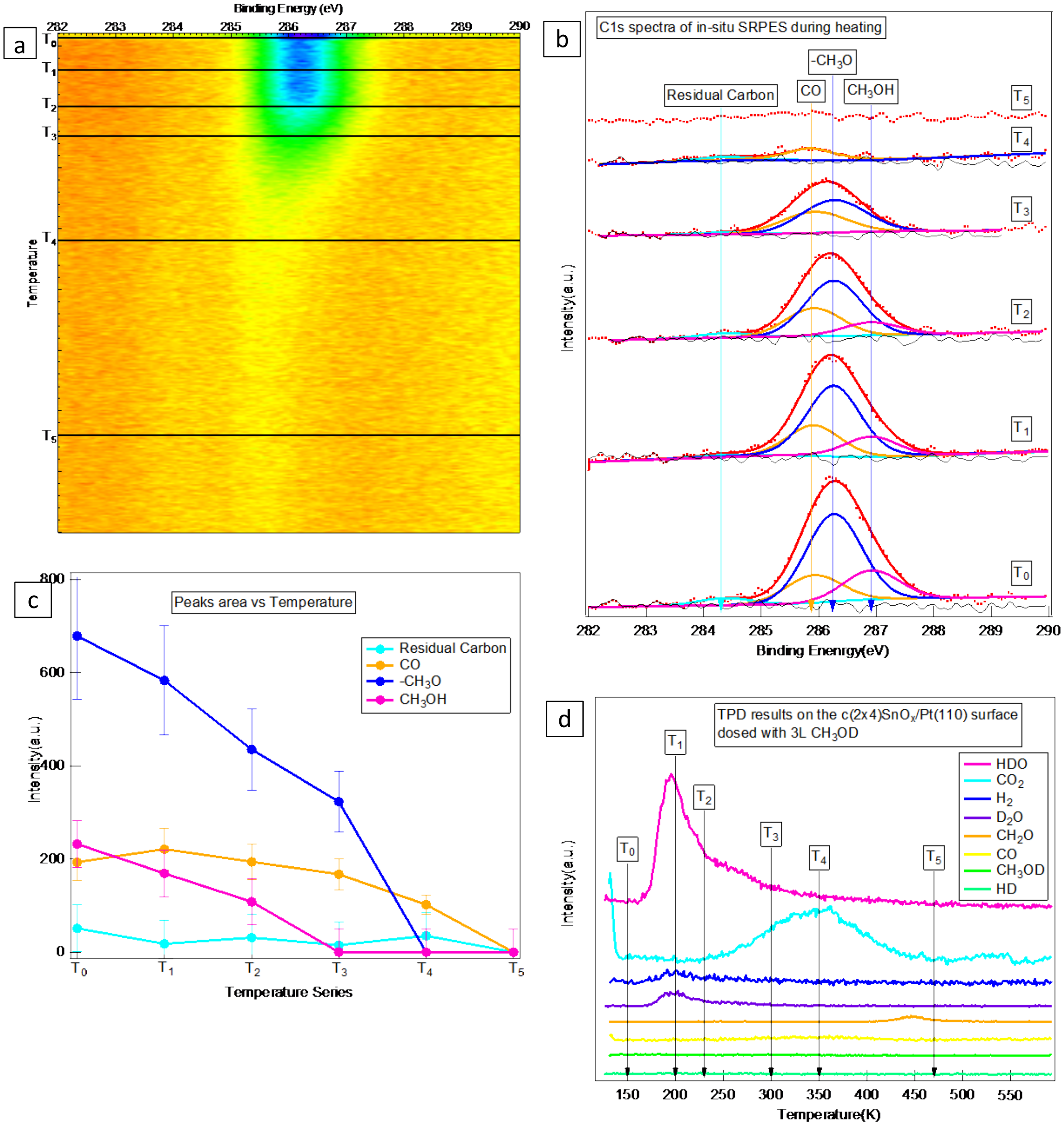

Figure 5-13 (a) in-situ matrix results of C1s and fitting data of spectra at certain temperature from the matrix , (b) fitting data of spectra extracted from the matrix and (c) the plot of the species' peaks area vs Temperature according to fitting data showing in (b), (d) the corresponding TPD results for the in-situ SRPES

Based on the above analysis, the (2×4) surface can oxidize the methanol to CO_2 and be reduced to PtSn alloys. To confirm the surface oxide reduction, an in-situ LEED test was performed. The sample was placed in front of the LEED screen, then the surface was heated to 673K and kept at this temperature during thousand Langmuir methanol dosing at 10^{-7}mbar The comparison of the LEED patterns of the original surface and the one after reaction is showed in Figure 5-14.

It is important to point out that no LEED pattern modifications were observed during the heating and thermalization of the sample at 673 K. Accoding to the LEED patterns, the original surface is a perfect c(2×4), while after the reaction with methanol it turns into mixed surfaces including c(2×4) and p(6×1) patterns. The p(6×1) surface is one of the most stable surfaces reported in the previous chapter.

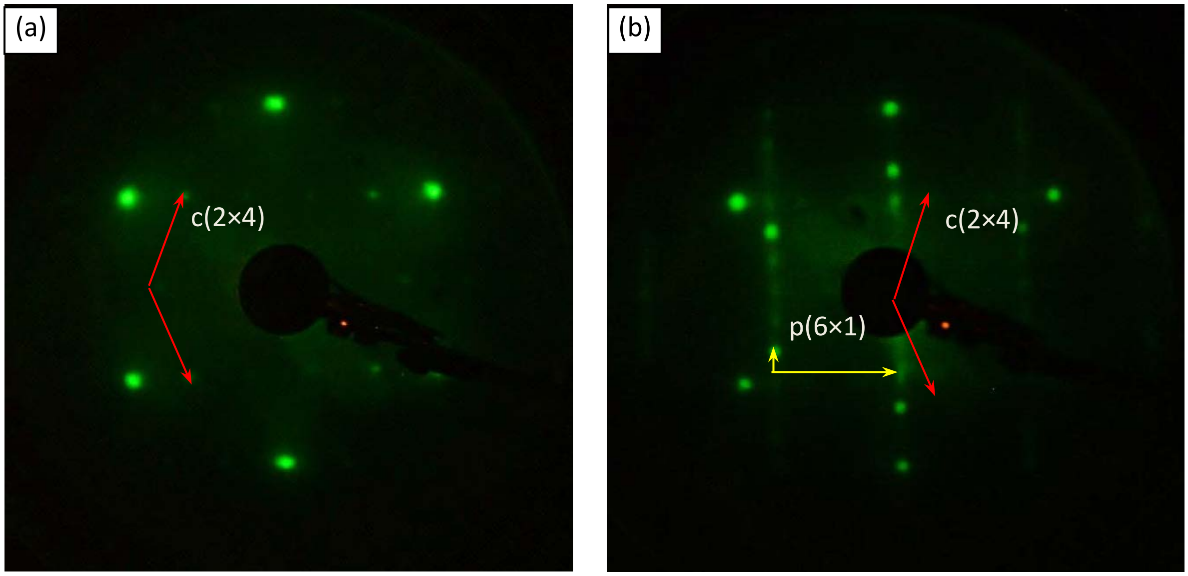

Figure 5-14 comparative LEED patterns of (a) the pristine c(2×4) SnO_x/Pt(110) phase (82.0 eV) and (b) the same surface after reaction with methanol at 10^{-7}mbar for several minutes(80.0 eV).

5.5 Conclusion

g. Some STM images at atomic solution of the two oxides: (c(2×4) surface and c(4×2) surface) were obtained and the both surface were also additionally characterized with SRPES which indicates c(2×4) surface is more oxidized than c(4×2) surface.
h. The model of the oxides were proposed and investigated by DFT calculations, and then the preferable models were confirmed and also match our SRPES analysis.
i. Reactivity of CO with the oxides were finished and also studied by DFT, indicating that c(2×4) surface can oxidize CO into CO_2 while c(4×2) surface is very inert. And comparing with oxidized Pt(110), the introduction of SnO_x can enhance the durability of the active surfaces.

j. The decomposition of methanol was also completed on the two surfaces. According to the results, methanol can be oxidized by c(2×4) surface into CO_2 and H_2O. After several cycle, the surface can form surface alloys or possible core-shell structure.

k. SRPES results indicate that after reaction with methanol, the surface will be reduced due to the reduction of Sn^{4+}, some Sn can be diffused into bulk.

References

[1] N. Tsud, T. Skala, F. Sutara, K. Veltruska, V. Dudr, M. Yoshitake, K.C. Prince, V. Matolin, J Phys-Condens Mat, 21 (2009).
[2] M. Hoheisel, S. Speller, A. Atrei, U. Bardi, G. Rovida, Phys Rev B, 71 (2005).
[3] M. Batzill, D.E. Beck, D. Jerdev, B.E. Koel, J Vac Sci Technol A, 19 (2001) 1953-1958.
[4] M. Batzill, D.E. Beck, B.E. Koel, Appl Phys Lett, 78 (2001) 2766-2768.
[5] M. Batzill, D.E. Beck, B.E. Koel, Phys Rev B, 64 (2001) 245402.
[6] M. Hoheisel, S. Speller, W. Heiland, A. Atrei, U. Bardi, G. Rovida, Phys Rev B, 66 (2002) 165416.
[7] A. Atrei, U. Bardi, G. Rovida, M. Torrini, M. Hoheisel, S. Speller, Surf Sci, 526 (2003) 193-200.
[8] M. Batzill, J. Kim, D.E. Beck, B.E. Koel, Phys Rev B, 69 (2004).
[9] S. Agnoli, G. Barcaro, A. Barolo, A. Fortunelli, M. Sambi, F. Sedona, M. Di Marino, T. Skala, G. Granozzi, J Phys Chem C, 115 (2011) 14264-14269.
[10] N. Tsud, T. Skala, K. Veltruska, M. Skoda, K.C. Prince, V. Matolin, J Phys-Condens Mat, 23 (2011).
[11] P. De Padova, R. Larciprete, C. Ottaviani, C. Quaresima, P. Perfetti, E. Borsella, C. Astaldi, C. Comicioli, C. Crotti, M. Matteucci, M. Zacchigna, K. Prince, Appl Surf Sci, 104-105 (1996) 349-353.
[12] L. Kaplan, R. I, R.L. Boxman, S. Goldsmith, M. Nathan, E. BenJacob, Thin Solid Films, 290 (1996) 355-361.
[13] C.L. Lau, G.K. Wertheim, Journal of Vacuum Science & Technology, 15 (1978) 622-624.
[14] J.-M. Themlin, M. Chtaïb, L. Henrard, P. Lambin, J. Darville, J.-M. Gilles, Phys Rev B, 46 (1992) 2460-2466.
[15] P. Depadova, M. Fanfoni, R. Larciprete, M. Mangiantini, S. Priori, P. Perfetti, Surf Sci, 313 (1994) 379-391.
[16] J.C. Davies, B.E. Hayden, D.J. Pegg, Surf Sci, 467 (2000) 118-130.
[17] S. Yamagishi, T. Fujimoto, Y. Inada, H. Orita, J Phys Chem B, 109 (2005) 8899-8908.
[18] B.E. Hayden, A.J. Murray, R. Parsons, D.J. Pegg, J Electroanal Chem, 409 (1996) 51-63.
[19] D.C. Godfrey, B.E. Hayden, A.J. Murray, R. Parsons, D.J. Pegg, Surf Sci, 294 (1993) 33-42.
[20] N. Seriani, W. Pompe, L.C. Ciacchi, The Journal of Physical Chemistry B, 110 (2006) 14860-14869.
[21] B.L.M. Hendriksen, J.W.M. Frenken, Phys Rev Lett, 89 (2002) 046101.
[22] L. Wei-Xue, Journal of Physics: Condensed Matter, 20 (2008) 184022.
[23] T.M. Pedersen, W. Xue Li, B. Hammer, Phys Chem Chem Phys, 8 (2006) 1566-1574.
[24] M.D. Ackermann, T.M. Pedersen, B.L.M. Hendriksen, O. Robach, S.C. Bobaru, I. Popa, C. Quiros, H. Kim, B. Hammer, S. Ferrer, J.W.M. Frenken, Phys Rev Lett, 95 (2005) 255505.
[25] W.X. Li, B. Hammer, Chem Phys Lett, 409 (2005) 1-7.
[26] G.A. Attard, K. Chibane, H.D. Ebert, R. Parsons, Surf Sci, 224 (1989) 311-326.
[27] J. Wang, R.I. Masel, J Catal, 126 (1990) 519-531.
[28] S. Axnanda, W.-P. Zhou, M.G. White, Phys Chem Chem Phys, 14 (2012) 10207-10214.
[29] W.-P. Zhou, W. An, D. Su, R. Palomino, P. Liu, M.G. White, R.R. Adzic, The Journal of Physical Chemistry Letters, (2012) 3286-3290.
[30] J. Szuber, G. Czempik, R. Larciprete, D. Koziej, B. Adamowicz, Thin Solid Films, 391 (2001) 198-203.
[31] T. Kawabe, K. Tabata, E. Suzuki, Y. Nagasawa, Surf Sci, 482–485, Part 1 (2001) 183-188.
[32] T. Kawabe, K. Tabata, E. Suzuki, Y. Nagasawa, Surf Sci, 454–456 (2000) 374-378.
[33] L. Artiglia, S. Agnoli, A. Vittadini, A. Verdini, A. Cossaro, L. Floreano, G. Granozzi, J Am Chem Soc, 135 (2013) 17331-17338.

[34] V.r. Matolín, V. Johánek, M. Škoda, N. Tsud, K.C. Prince, T.s. Skála, I. Matolínová, Langmuir, 26 (2010) 13333-13341.

6 General conclusion and Outlook

During my three years' work on my thesis, I had a systematic research on new ultrathin films of Sn on the Pt(110) surface and their oxides. Three surface alloys (including one already reported surface alloy) and two new surface oxides on Pt(110) surface were obtained.

The two novel surface alloys, i.e. p(3×1)PtSn/Pt(110) and p(6×1) PtSn/Pt(110), can be prepared by means of UHV Sn deposition on Pt(110) at different coverage, and with a consequent annealing at various temperature. Two SnO_x oxides surfaces, i.e. c(2×4)SnO_x/Pt(110) and c(4×2) SnO_x/Pt(110), were prepared by oxidation starting from the surface alloys. With optimization of the preparation condition, a phase diagram for the surface alloys and surface oxides on Pt(110) was determined.

The LEED pattern and STM images of the two novel surface alloys were obtained, and also SRPES of the p(6×1) surface was recorded at MaxLab (Lund). STM images of the two surface alloys are characterized by corrugated structures. Some models for the two surfaces were proposed based on the STM and LEED results (for p(6×1) surface, SRPES were also employed), and on DFT calculations. The simulated STM images were compared to the experimental ones. Based on the experimental and DFT results, the most suitable models for the two surfaces were proposed. The reactivity of the surface alloys with CO was investigated by TPD and DFT calculations. The results reveals similar CO reactivity on the two surfaces and higher CO poison resistance due to chemisorption with lower adsorption energy with respect to the one on pure Pt(110) surface. Based on the DFT results, the investigated surfaces can have a better COOR performance, and the introduction of Sn can enhance the COOR reactivity.

LEED patterns and STM images for the two nano-oxides (c(2×4)SnO_x/Pt(110) and c(2×4)SnO_x/Pt(110)) were obtained, and they were also characterized with SRPES at Elettra (Trieste). Some models for the two surfaces were proposed based on the experimental results and DFT calculations. According to DFT calculations and to comparison between experimental and simulated STM images, the most suitable models for the two surfaces were proposed, exhibiting a good agreement with the experimental data. Reactivity studies with CO were also carried out and also compared with DFT calculations, indicating that c(2×4) surface can oxidize CO to CO_2. On the contrary, c(4×2) surface is very inert.

From the point of view of the EC activity, with respect to oxidized Pt(110), the introduction of SnO_x can enhance the durability of the active surfaces.

The decomposition of methanol on c(2×4) surface was also investigated by TPD and SRPES, indicating that the methanol can be oxidized efficiently to CO_2 and H_2O, while the surface can be transformed into surface alloys or possible core-shell structure after several TPD cycles. The Sn^{4+} surface can be reduced during the TPD procedure, and some Sn diffuses into bulk.

In conclusion, PtSn surface alloys and SnO_x on Pt(110) can exhibit high reactivity for COOR reaction, hence they owns probably high MOR reactivity. However, such predictions require a detailed EC screening.

Acknowledgements

I have been in Italy more than three years for my thesis. During the past years, I gained a lot of support from others. Without their help, it was impossible to finish all the work. Firstly, I want to thank Prof. Gaetano Granozzi for his patient advice and passion for my research. I also want to thank Dr. Stefano Agnoli for his support in my academic work and suggestions for my daily life in Padova. Thanks are also given to my labmates: Prof. Gian Andrea Rizzi, Enrico Reeder, Marco Favaro, and Mattia Cattelan, due to their daily assistance.

Besides, I had about 4 months in Technical University of Denmark for some theoretical work. I met kind people who gave me many counsels for my studying there. So, I would like to give my thanks to Prof. Jan Rossmeisl and Dr. Michael Busch for their guidance in my learning DFT calculation. Also, I want to thank Martin Hangaard Hansen, Jens Jørgen Mortensen for their support about STM simulations.

Finally, I will specially thank my families for their constant support: my wife, my parents, my elder brother & his family, my younger sister & her family, and my parents-in-law. Without them, it would have been impossible to finish all my work.